

**Octave-spanning lasers for optical metrology
applications**

by

Lia Machado de Matos

B.S., Universidade Federal do Rio de Janeiro, Rio de Janeiro, Brazil
(1998)

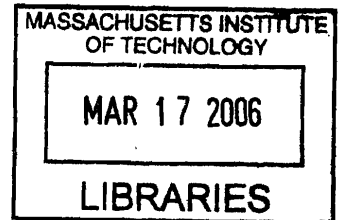
Submitted to the Department of Physics
in partial fulfillment of the requirements for the degree of

Doctor of Philosophy

at the

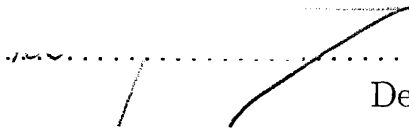
MASSACHUSETTS INSTITUTE OF TECHNOLOGY

[February 2006]
December 2005

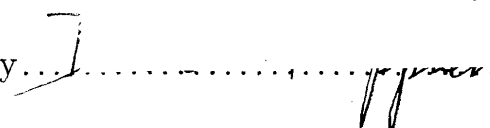


© Massachusetts Institute of Technology 2005. All rights reserved.

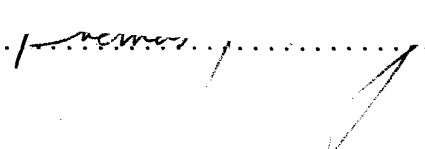
The author hereby grants to MASSACHUSETTS INSTITUTE OF
TECHNOLOGY permission to reproduce and
to distribute copies of this thesis document in whole or in part.

Signature of Author 

Department of Physics
December 1st, 2005

Certified by..... 

Daniel Kleppner
Lester Wolfe Professor of Physics
Thesis Supervisor

Certified by..... 

Thomas Greytak
Professor
Thesis Supervisor

Accepted by..... 

Thomas Greytak
Chairperson, Department Committee on Graduate Students

ARCHIVES

Octave-spanning lasers for optical metrology applications

by

Lia Machado de Matos

Submitted to the Department of Physics
on December 1st, 2005, in partial fulfillment of the
requirements for the degree of
Doctor of Philosophy

Abstract

This thesis describes the first octave-spanning frequency comb based on a prismless, Ti:sapphire laser. It covers in detail the design and construction of the laser system, as well as the electronic stabilization scheme used to control the frequencies of the mode comb. The system developed is suitable for optical metrology applications in general, although the version here presented is locked to the hydrogen 1S-2S transition frequency in ultracold hydrogen.

A detailed study of the carrier-envelope phase dynamics and noise characteristics of octave-spanning Ti:sapphire lasers is presented. We model the effect of the laser dynamics on the residual carrier-envelope phase noise by deriving a transfer function representation of the octave-spanning frequency comb. The modelled phase noise and the experimental results show excellent agreement. The model developed greatly enhances our capability of predicting the residual carrier-envelope phase noise in octave-spanning lasers, an important aspect in many time and frequency domain applications.

Potential applications of the current system to ultraprecise optical frequency metrology of ultracold hydrogen are described.

Thesis Supervisor: Daniel Kleppner
Title: Lester Wolfe Professor of Physics

Thesis Supervisor: Thomas Greytak
Title: Professor

Contents

1	Introduction	15
2	Kerr-lens Mode-locked Lasers for Metrology Applications	18
2.1	Kerr-lens mode-locked lasers	20
2.1.1	Self-focussing due to the Kerr effect	22
2.1.2	Typical KLM Ti:sapphire lasers	25
2.2	The spectrum of the mode comb	27
2.2.1	Self-referenced control of f_{CE}	30
2.2.2	Repetition rate control	31
2.3	Octave-spanning lasers: why?	32
3	Octave-spanning lasers: theory and challenges	35
3.1	The master equation for mode locking	35
3.2	Pulse dynamics in octave-spanning lasers	39
3.2.1	Nonlinear pulse propagation	39
3.2.2	The modified master equation	41
3.3	Technical challenges in generating octave-spanning spectra	46
3.3.1	Resonator design	46
3.3.2	Dispersion management	47
3.3.3	Output coupler design	52

4	Octave-spanning laser: experimental results	54
4.1	Resonator design	55
4.2	Results	61
4.2.1	Generating ultrabroadband spectra	61
4.2.2	Importance of the output coupler design	61
4.2.3	Generating the carrier-envelope beat signal	64
5	Stabilizing the octave-spanning frequency comb	70
5.1	The linear PLL	71
5.2	Digital phase detection	74
5.2.1	Ultrafast comparator	76
5.2.2	The AD9901 phase/frequency discriminator chip	77
5.2.3	Digital divider chips	79
5.3	Carrier-envelope frequency control	80
5.4	Repetition rate control: lock to 1S-2S spectroscopy laser	85
5.4.1	Heterodyne beat detection setup	86
5.4.2	Stabilization electronics	92
5.5	A note on passive stabilization	94
5.5.1	Vibration isolation	96
5.5.2	Temperature control	96
6	Carrier-envelope phase dynamics and noise analysis	98
6.1	Carrier-envelope phase dynamics of mode-locked lasers	100
6.2	Noise analysis of f_{CE} -stabilized lasers	108
6.2.1	Transfer function representation for the pulse energy versus pump power dynamics	110
6.2.2	Determination of the carrier-envelope phase error	117
7	Applications to frequency metrology of ultracold hydrogen	124
7.1	Measuring the 2S-8S transition	125

7.2 Measuring the 1S-2S transition	131
8 Conclusion and outlook	133
8.1 Outlook	135

List of Figures

2-1	Harmonic frequency chain built at the PTB.	19
2-2	Schematic diagram of Kerr-lens mechanism.	23
2-3	Schematic of typical KLM Ti:sapphire laser.	26
2-4	Schematic picture of electric field emitted from a mode-locked laser. . . .	28
2-5	Schematic representation of the frequency comb emitted from a mode-locked laser.	30
3-1	Schematic of fast saturable absorber mode-locking pulse evolution.	36
3-2	Schematic representing the order of the dispersive and nonlinear elements in the resonator.	43
3-3	Numerical simulation of dispersion-managed mode-locking.	44
3-4	Soft aperture KLM.	47
3-5	(a) Standard Bragg mirror, (b) simple chirped mirror, (c) double-chirped mirror (DCM).	48
3-6	DCM pairs.	50
3-7	Reflectivity and group delay of DCM pairs covering one octave.	51
3-8	Measured transmission of ZnSe/MgF ₂ quarter-wave dielectric stack used as an output coupler in the octave-spanning laser.	53
4-1	Schematic representation of the laser cavity.	56
4-2	Computer simulation to determine optimum operating point for KLM. . . .	60
4-3	Output spectrum of octave-spanning 191 MHz repetition rate laser. . . .	62

4-4	Octave-spanning spectra for 80 MHz and 191 MHz octave-spanning lasers.	63
4-5	Influence of output coupler transmission on laser output spectrum.	65
4-6	Carrier-envelope frequency detection setup for 80 MHz (a) and 191 MHz (b) lasers.	67
4-7	Radio frequency spectrum of carrier-envelope beat signal.	69
5-1	Block diagram of linear PLL.	72
5-2	Linear model of the PLL.	74
5-3	Schematics of digital phase detector board.	75
5-4	Schematics of ultrafast comparator AD96687 chip.	76
5-5	Functional block diagram of AD9901.	77
5-6	Sequence of waveforms describing the functionality of the AD9901.	78
5-7	Effect of frequency pre-division on the linear phase detection range of the PLL.	79
5-8	Schematic of f_{CE} phase lock setup.	80
5-9	Schematic of loop filter designed by Lia Matos and Cort Johnson.	82
5-10	Spectrum of phase locked f_{CE} beat, seen over three different frequency ranges.	83
5-11	Power spectral density (PSD) of the carrier-envelope phase fluctuations.	85
5-12	Representation of fully stabilized frequency comb, referenced to the 1S-2S transition in ultracold hydrogen.	87
5-13	Schematic representation of sum-frequency generation of comb light for locking to 1S-2S spectroscopy laser.	88
5-14	Conversion efficiency of sum-frequency generation of comb light at 972 nm to 486 nm.	90
5-15	Drawing of fast PZT-mounted mirror and schematic of setup for measuring PZT resonance response.	93
5-16	Experimental setup for frequency comb lock to dye laser.	95

6-1	Carrier-envelope frequency shift (left axis) and relative change in intracavity power (right axis) as a function of pump power	107
6-2	Relative intensity noise (RIN) of a Coherent Verdi-V6 (black curve) and a Spectra-Physics Millennia Xs (dark grey curve).	109
6-3	Comparison of the carrier-envelope phase noise of two self-referenced 200 MHz Ti:sapphire frequency combs pumped by different lasers.	110
6-4	Block diagram of the phase-lock loop (PLL) composed of the f_{CE} -stabilized laser.	111
6-5	Mode locking related energy-dependent loss $q_{ml}(E)$	113
6-6	Calculated amplitude and phase response of intracavity power with pump power for cw operation and for different values of saturable absorption.	115
6-7	Schematic of the transfer function measurement setup.	116
6-8	Measured and modelled amplitude and phase response of OSFC laser.	117
6-9	Block diagram describing the addition of intensity noise to the laser PLL.	119
6-10	Measured and calculated transfer functions for loop filter and AOM.	119
6-11	Calculated and measured carrier-envelope phase noise spectrum of the Millennia-Xs-pumped OSFC.	120
6-12	Calculated (black) and measured (grey) phase noise spectrum of carrier-envelope phase stabilized laser without taking the laser gain dynamics into account in the simulation. Because the low-pass filtering effect of the laser dynamic is absent, it is in theory possible to suppress the noise further without compromising the loop stability.	121
6-13	Amplitude and phase of open-loop transfer function of the laser PLL.	123
7-1	Schematic representation of complete setup to perform optical frequency metrology of ultracold hydrogen.	127
7-2	Complete optical setup for metrology of ultracold hydrogen.	128
7-3	Schematic representation of measurement of frequency gap between the optical frequencies of 1S-2S spectroscopy laser and 2S-8S spectroscopy laser.	130

7-4 Frequency measurement setup, with four frequency counters to measure the comb parameters f_{CE} and f_R as well as the heterodyne beats with the cw lasers. 130

List of Tables

4.1	Table indicating all cavity optical elements, with specifications and part numbers, where present	57
4.2	Relevant geometrical values of laser cavity	57
6.1	Transfer functions of the Ti:sapphire laser, phase detector, loop filter, and AOM.	118

Acknowledgments

The past six and a half years have been the most important and fruitful period of my life, and I have so many people to thank for that. If I were to remember every single one of them here, it would take endless pages, so I will do justice to only a few.

My first thank you goes to Franz Kärtner. I started working with Franz well into the third year of my PhD and since then I cannot understate how much he has supported, encouraged and inspired my work. Besides being one of the brightest minds I ever met, Franz joins together so many qualities which make him not only an amazing scientist but also a great mentor. Even though he was not my official thesis advisor, this work is to an enormous extent his time and effort. I saw Franz's group at MIT grow over the years, from two students and a postdoc to now what I would define as an army of people! I am always impressed with how well he manages it all. Even with so many students of his own, I cannot remember a time when Franz could not give at least a few minutes of his time to discuss our work. I am excited to see what great science and technology will come out of his group in the years to come.

I also owe many thanks to my advisors, Tom Greytak and Daniel Kleppner. I admire how many successful people have come out of this group over the past decades, and my experience here has been a great school of life. In the Ultracold Hydrogen group, I learned a great deal about how to be an independent thinker and worker and how to keep up the optimism even when the experiment was going through rough times, something I will take with me wherever I may go in the years to come. I thank Tom and Dan for trusting me with the research project I was given, which turned out to be a great research experience for me, well beyond my initial expectations. Special thanks goes to Dan for his constant support during my thesis preparation.

Six years is a lot of time. So many people who were a great support in my initial years at MIT are now well into their new lives and careers outside of grad school, but I could not forget to thank them. Stephen Moss, my first office mate and a senior graduate student when I started in the group, always brings me good memories of support and

encouragement in the first years when everything seemed so overwhelming: the course load was large and the qualifying exams were a nightmare. Looking back at it, these experiences made me grow as a person and I thank Stephen for helping me get through them and always showing me "the light at the end of the tunnel". I also cannot forget to mention Julia Steinberger, who immediately became a good friend with whom I got to enjoy many common tastes, like that for Brazilian music for example. She always showed her concern for my mental well being, something I will never forget. I will keep many good memories of the times we spent together in my first years at MIT.

Kendra Vant, my faithful lab, course and general exams companion over the years of MIT, became a great friend with whom I shared all important moments over these years, both in times of happiness and of struggle. Even though Kendra is actually younger than me, I have always thought of her as a big sister since she shaped who I am in so many ways, always serving as an inspiration to me with her strength and maturity. I thank her immensely for that. I could not have been a mother in graduate school without her support, also sharing the same experiences and telling me ahead of time what to expect from the challenges and joys that these little people (Clara and Tycho) would bring us. There was a big empty space in our lives after she left with her family for Los Alamos. Even after five months, Clara still talks about Thyco, and Pedro and myself truly miss him as well. Now the Ball-Vant family is growing and in my heart I wish that some day we can all spend time together again. I wish Greg and Kendra all the best in their new lives after grad school.

Cort Johnson came into the group in 2001, and brought new life to the lab. I am yet to meet someone who is more diligent, friendly, humorous, enthusiastic and calm than Cort, all of those qualities which make him the ideal lab partner! At the beginning, when I was teaching him about the laser system, I was quickly impressed with what a fast learner he was, and by now he is the lab member with the largest amount of combined knowledge in lasers and cryogenics. This I am sure guarantees him a bright future. Besides sharing many great moments with Cort in the lab figuring out electronics and laser bugs, Cort

and his wife Corey have become great friends. I thank them for all the joyous times we spent together and will miss them a lot.

Other members of the Ultracold Hydrogen Group have joined in the later years but with whom I also spent great moments. I saw Bonna through her first years going through much the same experiences as myself and I hope that I was able to provide her at least a little with the same support I could count on from the older students. It is great now to see her enthusiasm working in the lab and I hope the rest of her graduate career is a great success! I thank her as well for always being willing to help no matter what the circumstances were.

Despite not having a chance to work together in the lab with Rob de Carvalho, I enjoyed our many interesting discussions on random topics over lunch break, and his essential help with Scientific Word during my thesis writing. It has also been great to have someone in the lab with whom I could speak my native language of Portuguese. In the new lab, Rob, Nate, Bonna, Cort and Chih-Hao have really revived the hydrogen experiment! My special thanks goes to Chih-Hao for helping a lot in these last few months. I feel very relieved that someone as bright as him will take over my laser system and wish him the best of luck with his time at MIT.

Wow, I am running out of space and still so many people to thank...

Changing research groups, I cannot forget to thank all the people in the Ultrafast Optics Group who contributed so much to my time at MIT being a great one. At the beginning of my thesis project, I learned a lot from Thomas Schibli and thank him for the good times spent in the lab and over the long hours of soldering during our visit to JILA. In the later years, Jungwon Kim, Richard Ell and Oliver Mücke were always great company and I enjoyed working and chatting over lunch break with all of them very much. I especially thank Oli, with whom I have worked a lot over the last few months, for his endless support with the work and manuscript preparation.

Outside of MIT, the family-like environment provided by my Brazilian friends was essential to my survival. I saw many friends come and go over these years, but I owe

special thanks to a few who have always been there for me, some for as long as 10 years. Obrigada Rafa, Si, Andre, Diego e Mari. Valeu galera, sem vocês, a nossa familhinha brasileira aqui em Boston, não seria possível, de jeito nenhum.

I have always been so thankful to grow up in a family like mine. My parents, Maria and Pedro Paulo, have supported our intellectual pursuits since my remote memories. As a little kid, learning and studying was never a drag but always fun. I hope they teach me how they did it so I can do the same with my children! My mom, a physicist herself, has supported me since my first college years, always bringing her "inside view" which was so useful. If not for her, instigating my joy for physics and for having an inquiring mind, I would not be where I am today. My dad has always provided the emotional support, encouragement and trust which impuled me towards my achievements. As the little sister in the house, I have always admired and inspired myself in my brother and sister, Andre and Corina. They have, each in their own ways, supported me through my years in the US for which I will always be thankful. I really look forward to going back home to Brazil and seeing our families grow together.

Finally, to the extent that I can put it in paper, I want to thank the constant, unquestioning love and support from my husband Pedro. Over the last six years, first as friends and roommates, then as a family, we have grown so much together and seen ourselves trough some difficult but joyful times, like handling the challenges of being parents and invest in a career at the same time. Our family is my most important achievement and I only hope for a life of love and fulfillment with him, Clara and whoever may arrive in the future.

Chapter 1

Introduction

The past 5 years have been an exciting time for the field of optical frequency metrology. In the beginning of year 2000, the groups of Ted Hänsch and John Hall demonstrated an innovative technique for optical frequency synthesis based on mode-locked lasers. This development represented a merger of two distinct fields of study. On one side the techniques of laser stabilization learned over the past 30 years, aimed at achieving increasingly precise optical frequency measurements, on the other the developments of ultrafast science, in which the search for generation of yet shorter pulses reached the few-cycle regime. From this point onwards, both fields were to gain immensely from this joint venture.

This thesis represents the essence of this collaboration between ultrafast science and optical metrology, one of the first steps in a quest to develop a simple apparatus which has both capabilities: to generate a source with the shortest phase stabilized pulses and a self-referenced comb of frequencies directly from the laser. The focus of this work has in some sense been the optical frequency metrology, but the development of this apparatus has motivated us to improve our understanding of the control of the phase of light pulses or, more precisely, the carrier-envelope phase dynamics in mode-locked lasers, especially of those which produce octave-spanning spectra. This study presents the first complete noise analysis of carrier-envelope phase controlled laser pulses, taking into account the

effects of the laser dynamics on the carrier-envelope phase.

The scope of this thesis is twofold. We developed a system which is to be used for optical frequency metrology of ultracold hydrogen atoms. Specifically, we planned to perform two distinct experiments: first, to measure two-photon transitions originating from the metastable 2S state with an apparatus that offers several advantages if compared to previous experiments [1],[2]. Second, with a phase coherent link between the narrow (1.2 Hz natural linewidth) 1S-2S transition and the radio frequency domain given by the frequency comb, we would set out to perform the world's first measurement of this transition in a cold, trapped atomic sample. Unfortunately, a series of superfluid cryogenic leaks which could not be fixed with the resources available at the time became an impediment to our previously routine production of trapped hydrogen atoms. The laser systems will have to await further development of a new trapping apparatus for the realization of these experiments.

In the mean time, however, we have developed a fully controlled octave-spanning frequency comb, suitable for metrology applications in general, as well as time domain applications where the carrier-envelope phase control of the laser pulses is important. The complete noise analysis performed in such systems represents an important contribution to the understanding of the carrier-envelope phase dynamics of mode-locked lasers. Furthermore, we have gained insight into new possible mechanisms of carrier-envelope phase control that offer the potential for ever lower carrier-envelope phase jitter and at the same time a cheaper and simpler system.

This thesis is organized as follows: A quick review of the fundamental aspects of Kerr-lens mode-locked lasers and their application to frequency metrology is presented in Chapter 2. The discussion aims at introducing the inexperienced reader to the topic as well as to motivate the development of octave-spanning lasers. In Chapter 3 we present the theory which describes the dynamics of ultrashort pulse generation, with the goal of understanding the mechanisms that lead to the generation of very broad spectra. We follow with a discussion of the technological challenges that need to be overcome

to allow for octave-spanning spectra to be created directly from the laser. Chapter 4 describes the first experimental implementation of a prismless octave-spanning laser, with emphasis on the resonator design and carrier-envelope frequency detection setup. A discussion of the importance of the output coupler design on the generated spectrum is also presented. In Chapter 5 we present the details of the experimental implementation of the frequency comb stabilization, namely the control of the carrier-envelope frequency and laser repetition rate. In Chapter 6 we present a detailed discussion of the carrier-envelope phase dynamics in octave-spanning lasers and its impact in the noise analysis of such systems. We derive a transfer function representation of the octave-spanning laser and incorporate that into the analysis of the carrier-envelope phase locked loop to obtain excellent agreement between the measured and modeled residual phase noise. We discuss a possible new scheme for carrier-envelope phase control which circumvents fundamental as well as technical limitations of the current method of control by pump power modulation. Chapter 7 briefly describes how the developed system is to be used for making precise optical transition frequency measurements in ultracold atomic hydrogen. Finally, Chapter 8 concludes with a brief summary and outlook.

Chapter 2

Kerr-lens Mode-locked Lasers for Metrology Applications

The use of femtosecond lasers for frequency comb generation has revolutionized the technology of frequency metrology over the last 7 years. Previously, optical frequency measurements required large, expensive and labor intensive harmonic frequency chains. These chains consisted of an array of diode lasers and oscillators that could coherently link an optical frequency to the cesium standard. A serious drawback was that significant effort was required to measure a different frequency if it was more than a few hundred GHz away from the original. An example can be seen in Fig. 2-1 [3], which linked the $^1P_1 - ^1S_0$ intercombination transition of atomic ^{40}Ca in a magneto-optical trap to the cesium standard at the Physikalisch-Technische Bundesanstalt (PTB) in Braunschweig, Germany. The construction of these chains was so labor intensive that they became accessible only to a few large scale laboratories around the world.

In 1999, T. W. Hänsch and his group at the Max-Planck Institute in Garching, Germany developed a totally new approach to optical frequency measurements, based on ultrashort pulsed lasers[4][5][6]: in the frequency domain, the continuous pulse train emitted from a mode-locked laser consists of a comb of equally spaced optical lines which map, in one single step, two radio frequencies f_R and f_{CE} onto an optical frequency ν_m

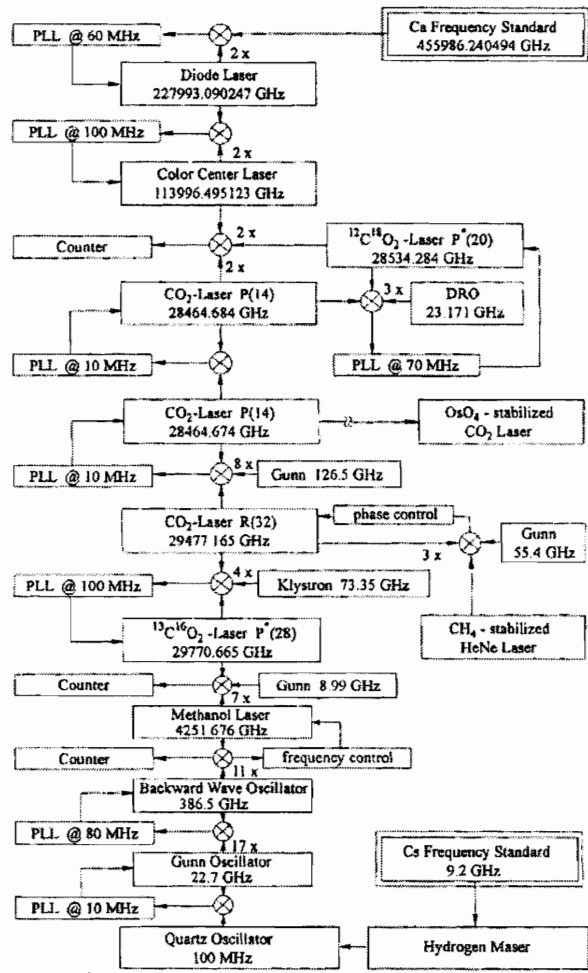


Figure 2-1: Frequency chain built at the PTB to link the Cs standard at 9.2 GHz to an intercombination line in ^{40}Ca .

via a large integer number on the order of one million. Thus, precise control of f_R and f_{CE} entitles full control of all the optical lines within the comb spectrum, generating a precise ruler with which to measure both large frequency differences and absolute frequencies in the optical region. Although Hänsch *et al.* had recognized the existence of the frequency comb properties of short pulses back in 1977[7], it was not until the advent of broadband femtosecond lasers that such realization became a reality.

The experiments by the Hänsch group revealed that the frequency comb lines emitted by a mode-locked laser are remarkably coherent. The mode spacing across the comb (even after spectral broadening in a standard single-mode optical fiber) was confirmed to be uniform within 3 parts in 10^{17} and the mode spacing was found to agree with the laser repetition frequency within 6 parts in 10^{16} [8]. These experiments guaranteed the great potential of femtosecond frequency combs as clockworks for ultra-high precision frequency metrology.

In this chapter, we present an overview of the implementation of mode-locked lasers as optical rulers. Section 2.1 gives a basic introduction to Kerr-lens mode-locked lasers, specifically to the concept of Kerr-lensing (Section 2.1.1) , which leads to the generations of ultrashort pulses. A description of the typical laser systems used for frequency comb applications is given in subsection 2.1.2, followed by a derivation, in 2.2 of the spectrum of the mode-comb and an overview of the main aspects involved in its stabilization. Finally, Section 2.3 hopes to motivate the reader to the development of comb systems based on octave-spanning lasers.

2.1 Kerr-lens mode-locked lasers

There are several different techniques for generating short pulses, or equivalently, the lasing of many longitudinal modes in a phase synchronous fashion. The earliest development consisted of what is known as active mode locking, where an active element (for example an electro-optic modulator) is placed in the cavity and modulates the intracavity losses

at a frequency precisely tuned to the inverse cavity round-trip time. The resulting pulse width in such lasers is limited by the electronic speed of the modulator, giving at best 1 ps pulse duration. This limitation is overcome in passively mode-locked lasers, where the loss (or gain) is modulated by the pulse itself. Since in such lasers the net gain window shortens with the pulse, passively mode-locked lasers can generate much shorter pulses than actively mode-locked lasers.

For passive mode locking to occur, a suitable saturable absorber mechanism is required. There are two distinct operating regimes which are differentiated by the relationship between the recovery time of the absorber T and the final pulse width τ . When $T \gg \tau$, we have *slow saturable absorber mode locking* [9], where the pulse is generated by a dynamic interplay between saturable gain and loss. In this case, gain saturation occurs on the time scale of the pulse itself. This is the case for semiconductor or dye lasers, which have large enough cross section for stimulated emission for the pulse to saturate the gain medium in a single pass. When $T \ll \tau$ and the absorber reacts instantaneously to the pulse, we get *fast saturable absorber mode locking* [10]. In the case of solid-state lasers, where the pulse energy is not large enough to saturate the gain medium in one single pass due to small gain cross sections, gain saturation on the time scale of the pulse can be neglected. Therefore, a fast saturable absorber must be present to open and close the gain window immediately before and after the arrival of the pulse.

Saturable absorption which is quasi-instantaneous has so far only been achieved through *artificial absorbers* by two methods: Kerr-lens mode locking (KLM) (see, for example, [11][12][13]) and Additive-pulse mode locking (APM) (see, for example, [14][15][16]). Specifically, in KLM, the self-focusing which occurs in the gain medium due to the non-linear Kerr effect, combined with a soft aperture created by the overlap of the laser beam with the gain profile creates a fast saturable absorption due to the ultrafast response of the Kerr effect, which is expected to be as fast as a few femtoseconds.

2.1.1 Self-focussing due to the Kerr effect

In a Kerr medium, the refractive index n is intensity dependent and for high enough intensities this nonlinearity becomes important

$$n = n_0 + n_2 I \quad (2.1)$$

where n_2 is the nonlinear index and I is the laser intensity. The Gaussian intensity profile of the beam

$$I(r) = \frac{2P}{\pi\omega^2} \exp[-2\left(\frac{r}{\omega}\right)^2] \quad (2.2)$$

generates also a Gaussian index profile in the material, which can be approximated by a parabolic index medium in the center of the beam by expanding 2.2 up to second order in r [17]:

$$n(r) = n'_0 \left(1 - \frac{1}{2} \gamma^2 r^2\right), \quad (2.3)$$

with

$$n'_0 = n_0 + n_2 \frac{2P}{\pi\omega^2}, \quad \gamma = \frac{1}{\omega^2} \sqrt{\frac{8n_2 P}{n'_0 \pi}} \quad (2.4)$$

Such a parabolic index medium is equivalent to a lens. It can be shown that the ABCD propagation matrix for a medium of thickness l under normal incidence is given by[18]

$$\begin{bmatrix} \cos(\gamma l) & \frac{1}{n'_0 \gamma} \sin(\gamma l) \\ -n'_0 \gamma \sin(\gamma l) & \cos(\gamma l) \end{bmatrix} \quad (2.5)$$

which in fact reduces to the ABCD matrix for a thin lens in the limit where $l \rightarrow 0$ while $n'_0 \gamma^2 l$ remains constant. Therefore, we can see that for high enough intensities, the transverse intensity profile of the beam generates focussing of the beam itself.

Such self-focussing of a Gaussian beam in a nonlinear medium is exploited in a Kerr-lens Mode-locked (KLM) laser to generate an artificial saturable absorber action and create short pulses. As the beam enters the nonlinear medium, the beam slightly focusses,

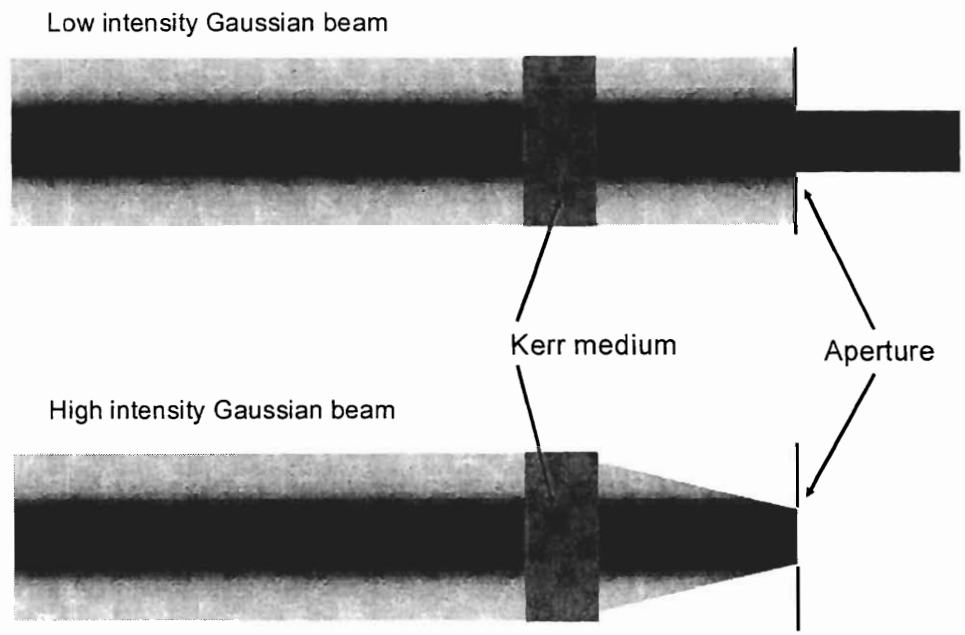


Figure 2-2: Schematic diagram of Kerr-lens mechanism. Above: low intensities experience higher losses as the light does not pass completely through the aperture. Below: high intensities, in contrast, experience no loss since the light gets fully transmitted through the aperture.

and the focussing increases with increasing light intensity. If an effective aperture is placed at the correct position, a saturable absorber can be created by allowing high intensities to be fully transmitted while low intensities experience losses (see Fig. 2-2). Since pulses produce higher peak powers than CW light, they will experience lower losses, causing this mechanism to favor pulsed over CW operation.

2.1.2 Typical KLM Ti:sapphire lasers

KLM Ti:sapphire lasers represent the basic building block for frequency comb generation. There, the nonlinear medium is also the gain medium, i.e. the Ti:sapphire crystal. An effective aperture is created by the proper selection of the pump mode size in the crystal. In this case, the change in the laser beam waist enhances the overlap between the laser mode and the pump mode and therefore enhances the gain of the self-focused laser mode. As a consequence, because the pulse peak sees higher gain/lower losses than the wings, the pulse shortens in each round trip. The response time of the nonresonant Kerr effect is on the order of a few femtoseconds, allowing the nonlinear index of refraction to follow the pulse almost instantaneously, enhancing the KLM action.

The ultimate limit on pulse width in a KLM laser stems from an interplay between KLM action, dispersion management and net gain bandwidth. An important reason for using Ti:sapphire is the fact that its gain bandwidth extends over 400 nm, from 680 nm to 1080 nm [19] and lasing can be obtained beyond this bandwidth. If the KLM laser can support a pulse short enough such that its spectrum spans beyond the gain bandwidth of Ti:sapphire, a spectrum which spans a full octave can be achieved. The achievement of such octave-spanning spectra is the central topic of this thesis and will be discussed in great detail in the following chapters. More often however, the typical pulse widths which can be achieved ranges from 10 to 30 fs, which has a spectrum well below one octave.

A schematic of a typical KLM Ti:sapphire laser can be seen in Fig. 2-3. The crystal is pumped by green light, typically from a diode-pumped solid-state laser emitting around 5 W of 532 nm light. A prism pair is placed in one of the cavity arms, introducing negative dispersion onto the pulse to compensate for positive dispersion in the laser crystal. Such setups are widely available commercially and represent the most common type of frequency comb setup.

The advantage of being commercially available and relatively simple to build is offset by many drawbacks. First, in order to be utilized as an optical ruler, the frequency comb

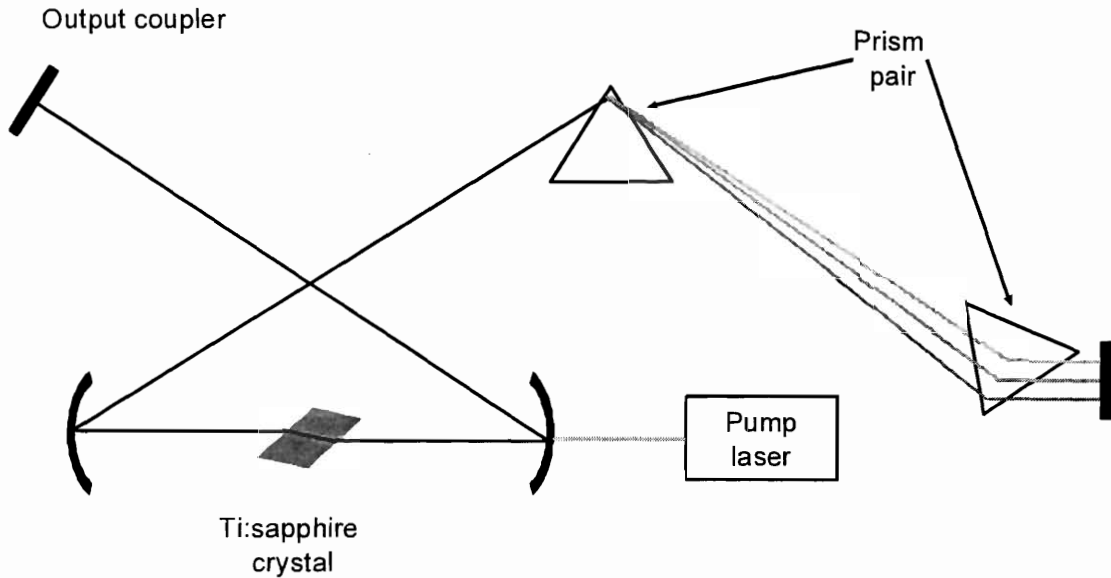


Figure 2-3: Schematic of traditional KLM Ti:sapphire laser. Prism pairs provide the dispersion balancing to allow for short pulse sustainable operation.

needs to be broadened in microstructure fibers to generate an octave of spectrum [20]. Although microstructure fibers can easily broaden the femtosecond laser spectrum to bandwidths exceeding one octave, they have severe limitations with regard to long-term operation in optical clockworks, since the burning of the tips of these fibers under high intensities requires constant re-alignment and even replacement of the fiber. The carrier-envelope (CE) phase noise added by amplitude-to-phase conversion in microstructure fibers has been thoroughly investigated by Fortier *et.al* [21][22]. They found that amplitude noise in the output light might mask the heterodyne beats in the radio-frequency spectra if too much broadening is necessary. Second, having prisms for dispersion compensation limits the choice of repetition rates in such laser systems: in order to introduce negative dispersion, the prism sequence needs to be at least about 30 cm apart, introducing an upper bound for the repetition rate of about 100 MHz. In metrology, high repetition rates are desirable for two reasons: first, they provide more power per comb line, allowing for higher signal-to-noise ratios when heterodyning with CW lasers; second,

the comb lines can conveniently be resolved with commercial wave meters.

2.2 The spectrum of the mode comb

Let us consider a periodic pulse train emitted by a mode-locked laser, where the pulse duration is much shorter than the time interval between pulses. If the pulses are unchirped, i.e. their frequency does not vary with time, it is straightforward to decompose the electric field of each pulse into a carrier wave and an envelope function $\varepsilon(t)$:

$$\hat{E}(t) = \varepsilon(t)e^{-i(\omega_C t + \phi_{CE})} \quad (2.6)$$

where ω_C is the carrier frequency and ϕ_{CE} is the relative phase between the carrier and the envelope. As the pulse propagates through dispersive elements in the laser cavity, the carrier propagates at the phase velocity while the envelope propagates at the group velocity, thus causing ϕ_{CE} to evolve. There are also nonlinear contributions to ϕ_{CE} , that will be described in detail in Chapter 6. Here, the important thing is to note that when such a pulse undergoes one round trip in the laser cavity, the dispersive and nonlinear contributions will cause its phase to change over time, such that each time it gets coupled out through the output coupler, perturbations will cause the phase to have a different value. In reality, ϕ_{CE} will evolve over many cycles, but for our purposes it is only the change modulo 2π that matters. We will designate this quantity by $\Delta\phi_{CE}$.

For the periodic pulse train, we can write the electric field as

$$\begin{aligned} E(t) &= \sum_{n=-\infty}^{+\infty} \hat{E}(t - nT) \\ &= \sum_{n=-\infty}^{+\infty} \varepsilon(t - nT)e^{-i(\omega_C(t-nT) + n\Delta\phi_{CE} + \phi_0)} \end{aligned} \quad (2.7)$$

where T is the round trip time of the pulse in the laser cavity. A schematic of the electric field of two consecutive pulses can be seen in Fig. 2-4. We have made the substitution

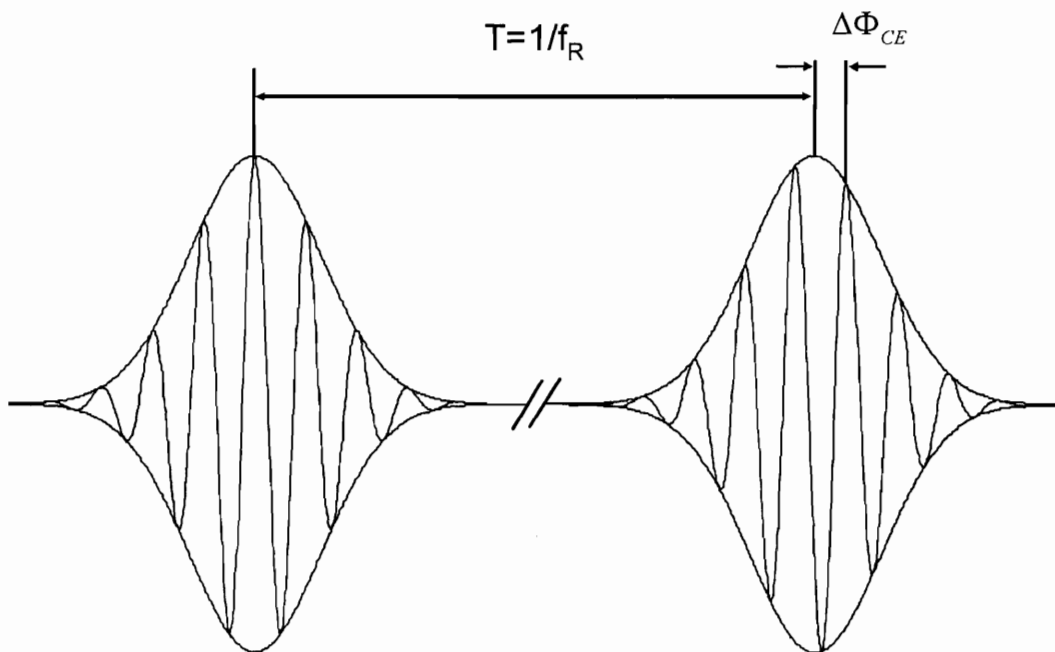


Figure 2-4: Schematic picture of the electric field of two consecutive pulses coupled out from a mode-locked laser. T is the round trip time in the laser cavity and $\Delta\phi_{CE}$ is the phase slip between the two consecutive pulses.

$\phi_{CE} = \phi_0 + n\Delta\phi_{CE}$ for the phase of the n^{th} pulse. The spectrum is found by taking the Fourier transform of the above expression:

$$\begin{aligned}\tilde{E}(\omega) &= \int \sum_{n=-\infty}^{+\infty} \varepsilon(t - nT) e^{-i(\omega_C(t-nT) + n\Delta\phi_{CE} + \phi_0)} e^{i\omega t} dt \\ &= \sum_{n=-\infty}^{+\infty} e^{i(n(\omega_C T - \Delta\phi_{CE}) - \phi_0)} \int \varepsilon(t - nT) e^{i(\omega - \omega_C)t} dt\end{aligned}\quad (2.8)$$

Making the change of variables $t' = t - nT$, we get

$$\begin{aligned}\tilde{E}(\omega) &= \sum_{n=-\infty}^{+\infty} e^{i(n(\omega_C T - \Delta\phi_{CE}) - \phi_0)} \int \varepsilon(t') e^{i(\omega - \omega_C)t'} dt' \\ &= e^{-i\phi_0} \tilde{\varepsilon}(\omega - \omega_C) \sum_{n=-\infty}^{+\infty} e^{i(\omega T - \Delta\phi_{CE})n},\end{aligned}\quad (2.9)$$

where $\tilde{\varepsilon}(\omega - \omega_C)$ is the Fourier transform of the pulse envelope. Using the Poisson formula $\sum_{n=-\infty}^{+\infty} e^{inp} = \sum_{m=-\infty}^{+\infty} \delta(p - m2\pi)$, we find that the spectrum of an infinite train of pulses consists of discrete comb lines underneath the spectrum envelope:

$$\tilde{E}(\omega) = e^{-i\phi_0} \tilde{\varepsilon}(\omega - \omega_C) \sum_{m=-\infty}^{+\infty} \delta(\omega T - \Delta\phi_{CE} - m2\pi) \quad (2.10)$$

with frequencies given by $\omega_m = \frac{1}{T}(2\pi m + \Delta\phi_{CE})$. Converting from angular frequency, we obtain for the spectrum of the mode comb

$$\nu_m = mf_R + f_{CE} \quad (2.11)$$

where $f_{CE} = \Delta\phi_{CE}f_R/2\pi$ and f_R is the laser repetition rate, or the inverse cavity round-trip time.

Equation 2.11 makes it clear that two RF frequencies f_R and f_{CE} uniquely determine the frequency of each comb line in the laser spectrum. Therefore an optical ruler with millions of stable optical lines can be obtained by precise control of these two quantities.

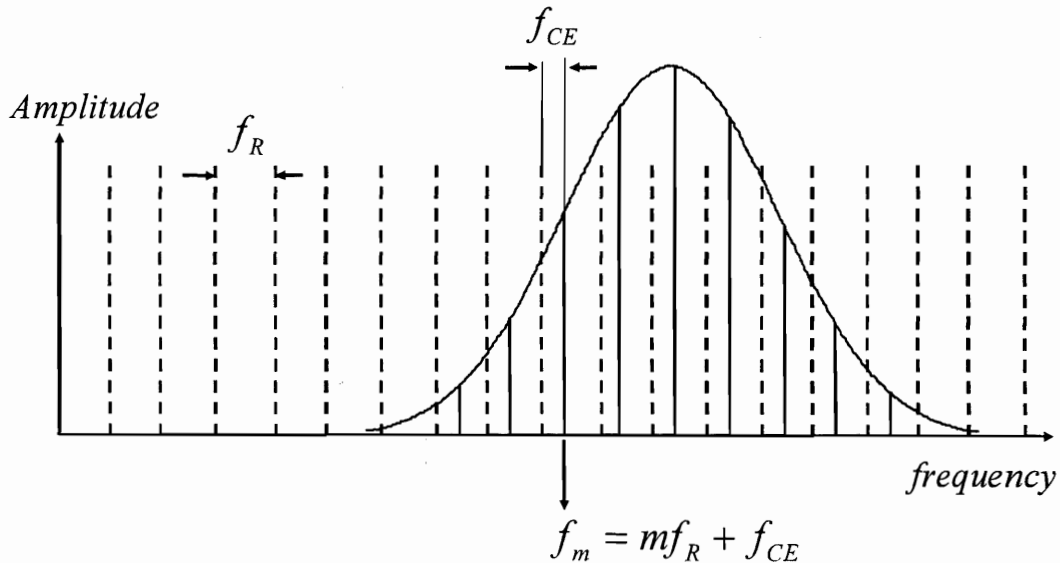


Figure 2-5: Schematic representation of the frequency domain picture of short pulses. The spacing between the comb modes is the inverse round trip time in the laser cavity. The offset frequency f_{CE} is the manifestation in the frequency domain of the carrier-envelope phase $\Delta\phi_{CE}$.

A schematic of the frequency comb is shown in Fig. 2-5.

2.2.1 Self-referenced control of f_{CE}

The simplest and most widely used technique for controlling the carrier-envelope phase of ultrashort pulses, the $f - 2f$ self referencing stabilization scheme was first implemented by researchers at JILA and NIST in 2000 , soon followed by the Max Plank institute [5][23][24]. Self-referencing provides a measurement of f_{CE} without the need for any external reference, such as a molecular or atomic transition. In this method, the long wavelength part of the spectrum is doubled and brought to interference with the short wavelength part. If the comb spectrum is sufficiently broad that it covers an optical octave, the doubled part of the spectrum will overlap with the high frequency end, permitting direct carrier-envelope frequency detection. By heterodyning of these

two spectral components, the beat frequency yields

$$f_{\text{beat}} = 2\nu_m - \nu_{2m} = 2(mf_R + f_{\text{CE}}) - (2mf_R + f_{\text{CE}}) = f_{\text{CE}} \quad (2.12)$$

As will become clear in the following chapters, in a mode-locked laser f_{CE} has both a linear and a nonlinear contribution. Given an error signal, by comparing f_{CE} with a stable RF signal via a phase detector, an active control can be implemented in two distinct ways, by controlling either the beam insertion in the prism [5] or the pump power [25]. In the first method, the end mirror of the laser in the arm which contains the prism pair (see Fig. 2-3) is rotated about an axis perpendicular to the beam path, which has the effect of changing the relative path length between short and long wavelengths, which is equivalent to a group delay. In the second method, in which the pump power is controlled, the change in f_{CE} will be due to the nonlinear contribution to the carrier-envelope phase. A change in the pump power has the effect of changing the nonlinearity in the crystal due to the Kerr effect, which in turn affects both the group and phase velocities of the pulse. Because this is the method employed in this work, it will be described in great detail in the following chapters.

2.2.2 Repetition rate control

After implementation of the self-referenced lock, the absolute position of the comb is fixed, but the spacing between the lines still drifts due to perturbations in the repetition rate caused mainly by cavity length fluctuations. The repetition rate is stabilized by feeding an error signal to piezo actuators which control the cavity length. The reference which is used for this lock will depend on the experiment in question. Very often, the repetition rate is locked to a microwave generator locked to the cesium standard. If care is not taken to reduce noise in the detection process, this kind of lock might end up printing electronic noise on to the optical comb lines, which are the one millionth harmonics of the fundamental repetition rate in the case of 100 MHz lasers. For this reason, typically

the 20th harmonic of repetition rate is detected instead of the fundamental [6],[5],[24].

If an optical transition is used as a reference, the achievable precision is greatly increased. In this case, a CW laser locked to an atomic or molecular transition is heterodyned with a comb line, and the beat signal can then be phase locked to a very stable oscillator. Depending on the stability of the CW laser, such a lock can generate a very stable clock signal. This fact provides the basis for the implementation of frequency combs as the clockwork in atomic clocks based on optical transitions [26],[27]. There, the incredibly high quality factor of some optical transitions can be transferred phase-coherently, in one single step, from hundreds of terahertz down to hundreds of megahertz.

2.3 Octave-spanning lasers: why?

Although an octave of spectrum can be generated by spectral broadening in microstructure fiber, the discussion in Section 2.1.2 made it clear that there are many potential advantages to using a laser that can generate an octave directly. Therefore, much experimental effort has been devoted to developing more reliable, more stable, and simpler optical clockworks without the need for external spectral broadening. Because no laser gain medium has a gain bandwidth which spans an octave, nonlinearity plays an important role in octave-spanning lasers, generating spectrum well beyond the gain bandwidth of the laser crystal. The first demonstration of an octave-spanning laser utilized a second intracavity focus on a glass material to enhance the nonlinearity [28]. More recently, there have been several demonstrations of Kerr-lens mode locked Ti:sapphire lasers that utilize the laser crystal alone as the nonlinear medium [29][30].

By eliminating the microstructure fiber, issues of coupling and damage are also eliminated. The very small core diameters of microstructure fibers cause the coupling to degrade over time due to great alignment sensitivity. Also the high intensities which are present tend to burn the tips of the fibers over time. Both these effects pose a

limit of at most 10 hours on the duration of experiments. Although this is likely to be long enough for many applications, optical clockworks need to run continuously for days without interruption. Octave-spanning laser development provides great potential for this achievement.

The system developed in this thesis is the first realization of an octave-spanning laser where the ultrabroadband dispersion control is achieved with mirrors only, eliminating the need for intracavity prisms. Other octave-spanning lasers have been demonstrated which utilize intracavity prisms [30]. However, prismless cavities have the advantage of being scalable to high repetition rates, more convenient for metrology. Correspondingly the cavity size can be scaled down to create very compact systems which are more stable against environmental perturbations, therefore enhancing the long term stability.

Other approaches are being explored beyond octave-spanning lasers to control f_{CE} without the need for fiber broadening. Ti:sapphire laser systems with repetition rates up to 1 GHz have been f_{CE} phase stabilized without the need for external broadening using the more complex $2f - 3f$ self-referencing technique [31]. More recently, direct $f - 2f$ self-referencing has also been demonstrated with these high repetition rate lasers [32]. Also, f_{CE} has been detected in few-cycle Ti:sapphire lasers using the interference between spectral components generated by self-phase modulation (SPM) and second-harmonic generation (SHG) in thin ZnO crystals [33][34] and using the interference between SPM and difference-frequency generation (DFG) in a periodically-poled lithium niobate (PPLN) crystal [35]. Fiber laser-based frequency combs are also an attractive alternative for metrology because of their turnkey operation [36][37][38]. However, at present measurements of f_{CE} in these lasers exhibit significantly higher linewidths relative to Ti:sapphire, indicating increased phase fluctuations compared to Ti:sapphire laser-based combs. This results in decreased short-term stability and longer averaging times for precision measurements.

This field is far from having reached a final stage and new developments are published every few months. The system which will eventually prove to be the preferred optical

clockwork for optical atomic clocks is yet to be determined. However, the development presented in this thesis represent a significant step in this direction.

Chapter 3

Octave-spanning lasers: theory and challenges

In this chapter, we will give a brief overview of the theory needed to understand the generation of octave-spanning spectra directly from the laser. We will start by introducing the master equation for mode locking, which describes the dynamics of the pulse formation process, in a general and straightforward fashion. We will then apply it to the case of the Ti:sapphire lasers developed here. This is followed by a discussion in Section 3.3 of the main technical challenges that must be overcome to enable the generation of ultrabroadband spectra.

3.1 The master equation for mode locking

The *Master Equation of Mode Locking* was first derived by H. Haus in 1975 [39] to describe the dynamics of the pulse formation process in mode locked lasers. His derivation is based in the assumption that the pulse undergoes only small changes in each round trip through the resonator. Therefore, a natural time scale to consider in the pulse evolution is the cavity round trip time T_R . The change in the pulse envelope in one round trip can

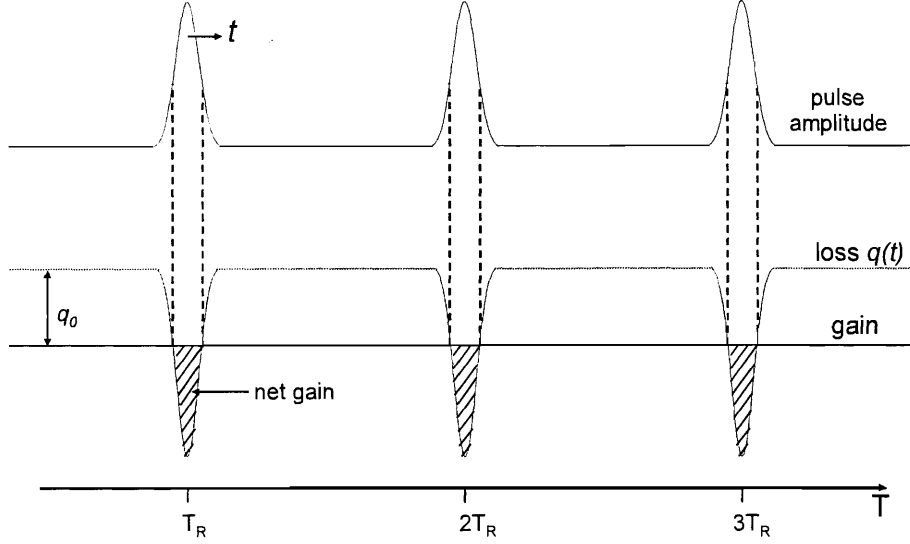


Figure 3-1: Schematic of fast saturable absorber mode-locking pulse evolution, described by the Master Equation of Mode Locking. The two time scales describing the pulse evolution and resulting shape, T and t , are shown in the diagram.

then be written as

$$\Delta A(T, t) = A(T, t) - A(T - T_R, t) \approx T_R \frac{\partial A(T, t)}{\partial T}, \quad (3.1)$$

where $A(T, t)$ is the slowly varying field envelope. The evolution of $A(T, t)$ is examined in two time scales, which are depicted in the diagram of Fig. 3-1. The global time T is coarse grained on the time scale of the cavity round trip time, while the local time t resolves the pulse shape itself. $A(T, t)$ is normalized to the instantaneous power such that $|A(t)|^2 = P(t)$.

The description of mode-locking in terms of a pulse envelope dependent on the variable t that evolves in time according to 3.1 can be described interchangeably by a pulse spectrum that evolves on the same time scale T . Thus, the Master Equation of Mode

Locking can be written in either the time or frequency domain, simply by taking the Fourier-transform according to

$$A(T, t) = \int e^{-i\omega t} \tilde{A}(\omega, T) d\omega \quad (3.2)$$

$$\tilde{A}(\omega, T) = \frac{1}{2\pi} \int e^{i\omega t} A(t, T) dt. \quad (3.3)$$

In a passively mode locked laser, the resonator is composed of elements of gain, loss and saturable absorption. Let us start by considering the gain. As described in Section 2.1, for Ti:sapphire the gain does not react on the time scale of the pulse itself but on the average power. Let us consider a gain medium with a Lorentzian gain profile

$$g(\omega, T) = \frac{g(T)}{1 + \left(\frac{\omega}{\Omega_g}\right)^2} \quad (3.4)$$

In the limit in which the pulse spectrum is narrow compared to the gain bandwidth Ω_g , we can make a parabolic approximation to Eq. 3.4 to obtain an expression for the amplitude changes to the pulse spectrum over the time T by

$$\Delta \tilde{A}(\omega, T) = g(T) \left[1 - \left(\frac{\omega}{\Omega_g}\right)^2 \right] \tilde{A}(\omega, T)$$

Which gives in the time domain

$$\Delta A(t, T)_{gain} = g(T) \left(1 + \frac{1}{\Omega_g^2} \frac{\partial^2}{\partial t^2} \right) A(T, t) \quad (3.5)$$

where the second derivative comes from taking the Fourier transform of a Lorentzian gain profile with width Ω_g under a parabolic approximation. $g(T)$ is an average gain, which can be computed by averaging the rate equation over one round trip [17].

The effect of the linear, non-saturated cavity loss is simple

$$\Delta A(t, T)_{loss} = -l_0 A(T, t) \quad (3.6)$$

where l_0 is the loss per round trip. The round trip change in the pulse due to the saturable absorber has the same form as 3.6, replacing l_0 by $q(t)$, the response function of the saturable absorber. For the case of fast saturable absorption, $q(t)$ responds instantaneously to the pulse power

$$q(t) = q_0 \frac{1}{1 + \frac{|A(t, T)|^2}{P_A}} \quad (3.7)$$

which, in the limit of small saturation, can be expanded to give

$$q(t) = q_0 - \gamma |A(t, T)|^2, \quad \gamma = \frac{q_0}{P_A}. \quad (3.8)$$

This gives a contribution to the change in the pulse over a round trip of

$$\Delta A(t, T)_{sat. loss} = (q_0 - \gamma |A(t, T)|^2) A(T, t) \quad (3.9)$$

Thus, the total change due to all the above contributions is

$$\Delta A(t, T)_{total} = \Delta A(t, T)_{gain} + \Delta A(t, T)_{loss} + \Delta A(t, T)_{sat. loss} \quad (3.10)$$

Which leads to the simplest form of the master equation

$$T_R \frac{\partial A(T, t)}{\partial T} = (g - l) A(T, t) + \frac{g}{\Omega_g^2} \frac{\partial^2}{\partial t^2} A(T, t) - \gamma |A(t, T)|^2 A(T, t). \quad (3.11)$$

where $g \equiv g(T)$ and $l = l_0 + q_0$. This equation has a steady state solution, when $\Delta A(t, T)_{total} = 0$, given by a hyperbolic-secant shaped pulse $A(t) = A_0 \text{sech}(t/\tau)$, with the pulse width given by the relations $1/\tau^2 = \gamma A_0^2 \Omega_g^2 / 2g$ and $l - g = g/\Omega_g^2 \tau^2$. Although it is not a stable solution, it gives analytic insight to this formalism. A stabilized solution

can be obtained if saturation of the absorber is explicitly included [40].

3.2 Pulse dynamics in octave-spanning lasers

For femtosecond lasers, the high peak intensities render the nonlinear self-phase modulation (SPM) effect occurring in the nonlinear laser medium appreciable, as well as the influence of dispersion on the pulse formation. Therefore, an appropriate model to describe the dynamics of short pulses needs to include such effects in the master equation. In order to clearly understand how these terms are included, a short detour on nonlinear pulse propagation will be given. Then, we will present a modified master equation which describes the pulse dynamics in our octave-spanning lasers, a regime called dispersion-managed mode-locking.

3.2.1 Nonlinear pulse propagation

In this section we present a phenomenological derivation of the effects of dispersion and nonlinearity on the pulse propagation. The electric field of a pulse propagating in a nonlinear dispersive medium is given by

$$E(z, t) = \text{Re} \left[\frac{1}{2\pi} \int_0^\infty \tilde{E}(\Omega) e^{i(\Omega t - K(\Omega)z)} d\Omega \right]$$

which is the sum of plane waves with frequency Ω . In a dispersive medium the refractive index varies with frequency. Therefore the wave vector has the frequency dependence $K(\Omega) = n(\Omega)\Omega/c_0$, where c_0 is the speed of light in vacuum. If the spectrum of $E(z, t)$ is centered at ω_0 , we can make the transformation of variables: $\omega = \Omega - \omega_0$, $k(\omega) = K(\Omega) - K(\omega_0)$ and write the electric field as a carrier and an envelope function:

$$E(z, t) = \text{Re} [A(z, t) e^{i(\omega_0 t - K(\omega_0)z)}]$$

where

$$A(z, t) = \frac{1}{2\pi} \int_0^\infty \tilde{E}(\Omega) e^{i(\omega t - [K(\Omega) - K(\omega_0)]z)} d\Omega \equiv \frac{1}{2\pi} \int_{-\omega_0}^\infty \tilde{A}(\omega) e^{i(\omega t - k(\omega)z)} d\omega. \quad (3.12)$$

Taking the derivative of Eq. 3.12 with respect to z we get

$$\begin{aligned} \frac{\partial A(z, t)}{\partial z} &= \frac{1}{2\pi} \int_0^\infty -i[K(\Omega) - K(\omega_0)] \tilde{E}(\Omega) e^{i(\omega t - [K(\Omega) - K(\omega_0)]z)} d\Omega \\ &= \frac{1}{2\pi} \int_{-\omega_0}^\infty -ik(\omega) \tilde{A}(\omega) e^{i(\omega t - k(\omega)z)} d\omega. \end{aligned} \quad (3.13)$$

To consider both the effects of dispersion and nonlinearity, recalling Eq. 2.1 we write the index of refraction as $n(\Omega, I) = n(\Omega) + n_2 I$, where $I(z, t) = |A(z, t)|^2 / A_{eff}$, A_{eff} being the laser mode cross sectional area in the nonlinear medium. This gives the following expression for the wave vector $K(\Omega)$

$$\begin{aligned} K(\Omega) &= n(\Omega) \frac{\Omega}{c_0} + n_2 I \frac{\Omega}{c_0} \\ &= n_2 I \frac{\omega}{c_0} + n_2 I \frac{\omega_0}{c_0} + \left. \frac{\partial k(\omega)}{\partial \omega} \right|_0 \omega + \frac{1}{2} \left. \frac{\partial^2 k(\omega)}{\partial \omega^2} \right|_0 \omega^2 + \frac{1}{6} \left. \frac{\partial^3 k(\omega)}{\partial \omega^3} \right|_0 \omega^3 + O(\omega^4). \end{aligned} \quad (3.14)$$

If we assume that the spectrum is narrow such that $\omega \ll \omega_0$, we can consider only the nonlinear term which contains the center frequency ω_0 and incorporate this expansion into Eq. 3.13. Remembering that in a Fourier transformation $\omega^n \Leftrightarrow (-i \frac{\partial}{\partial t})^n$, we obtain an equation describing the nonlinear propagation of the pulse envelope in a nonlinear medium

$$\frac{\partial A(z, t)}{\partial z} = \left[i \sum_{n=1} D_n \left(-i \frac{\partial}{\partial t} \right)^n + i \frac{\omega_0}{c} n_2 \frac{|A(z, t)|^2}{A_{eff}} \right] A(z, t).$$

Where $D_n = \left. \frac{1}{n!} \frac{\partial^n k(\omega)}{\partial \omega^n} \right|_{\omega_0}$ is the n^{th} order dispersion coefficient. The first term in the sum describes the simple propagation of the pulse at the group velocity $v_g = 1/D_1$. We eliminate this trivial propagation by a coordinate transformation to the local time $t' = t - z/v_g$, $z = z'$. In this derivation, t' corresponds to the local time t in the master equation. We have eliminated the prime to simplify the notation. If we consider only the

effect of second order dispersion and nonlinearity on the pulse propagation, we obtain the nonlinear Schrödinger equation (NLSE) in which the potential energy term is proportional to the square of the envelope function itself

$$\frac{\partial A(z, t)}{\partial z} = \left[-iD_2 \frac{\partial^2}{\partial t^2} + i \frac{\omega_0}{c} n_2 \frac{|A(z, t)|^2}{A_{eff}} \right] A(z, t). \quad (3.15)$$

This equation describes the propagation of a soliton, i.e. a pulse which propagates in a nonlinear dispersive medium without changing its shape. The stability is due to the balance between the nonlinearity (SPM) and the dispersion. Soliton propagation is a general physical phenomenon and is described extensively in the literature (see, for example [41]).

3.2.2 The modified master equation

From the previous discussion, it becomes clear how to include dispersion and self-phase modulation into the master equation. We can replace the longitudinal coordinate z in the NLSE by the global time coordinate T in the master equation by the transformation $T = z/v_g \Rightarrow \partial/\partial z = T_R/L \partial/\partial T$. If we include also the effects of gain and loss already described in Sec. 3.1, the dynamics of a laser mode-locked with a fast saturable absorber, that produces pulses short enough to "feel" the effects of dispersion and nonlinearity is described by the master equation

$$T_R \frac{\partial A}{\partial T} = (g - l)A + (D_f - iD_2) \frac{\partial^2}{\partial t^2} A + (\gamma + i\delta) |A|^2 A \quad (3.16)$$

Here, $D_f = g/\Omega_g^2$ is the effective gain curvature, and the associated filtering action is represented by $D_f \frac{\partial^2}{\partial t^2} A$. For octave spanning lasers, gain filtering is an important factor limiting the ultimate pulse width, by causing a monotonic increase in loss with decreasing pulse width. Now, $D_2 = \frac{d^2 k}{d\omega^2} L/2$ is the group-velocity dispersion (GVD) parameter for a medium of length L with wave number $k(\omega)$. The Kerr coefficient is $\delta =$

$(2\pi/\lambda_C)n_2L/A_{eff}$, where λ_C is the carrier wavelength, n_2 is the nonlinear index in cm/W, and A_{eff} is the effective mode cross-sectional area in cm. To simplify the dynamics, the gain is taken to follow adiabatically the intracavity pulse energy as applicable for a gain medium with a relatively long relaxation time (which is the case for Ti:sapphire lasers). This equation has a simple steady state solution [42]

$$A(T, t) = A_0 \operatorname{sech}^{(1-i\beta)}\left(\frac{t}{\tau}\right) e^{-i\theta} \quad (3.17)$$

A thorough discussion of the impact of the variation of different parameters on the pulse solution is given in [40]. Analogously to the NLSE, a chirp-free soliton ($\beta = 0$) solution exists for weak gain filtering (small D_f) and small self-amplitude modulation (SAM) coefficient γ

$$A(T, t) = A_0 \operatorname{sech}\left(\frac{t}{\tau}\right) e^{-i\delta|A_0|^2 T/2T_R} \quad (3.18)$$

where we can see that the pulse acquires a phase shift per round trip due to the Kerr effect of $-\frac{1}{2}\delta|A_0|^2$. This nonlinear contribution to the phase manifests itself in the frequency domain by contributing to the carrier-envelope offset frequency a term dependent on intensity equal to $-\frac{f_R}{4\pi}\delta A_0^2$.

Equation 3.16 describes the pulse evolution in a medium with continuously distributed dispersion and SPM [43]. However, as first pointed out by C. Spielmann *et. al* [44], for lasers generating pulses as short as 10 fs and below, large changes in the pulse width occur within one round trip through the resonator because the dispersive elements, positive and negative, as well as the SPM section are placed discretely and the ordering of the elements of the resonator has a large impact on the resulting pulse width. This effect was first observed in a fiber laser and is called stretched-pulse mode locking [45].

The spectral bandwidth of our octave-spanning Ti:sapphire lasers indicate that the pulse propagating in the cavity should be as short as 5 fs (measured spectra will be shown in the experimental results). Therefore, we should consider the impact of the discrete action of dispersion and nonlinearity in the laser on the spectral shape of the laser pulses.

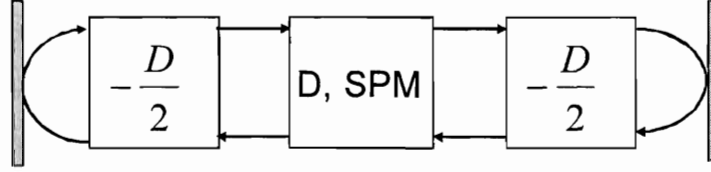


Figure 3-2: Schematic representing the order of the dispersive and nonlinear elements in the resonator.

A mode-locked laser consists of a gain medium (i.e., the Ti:sapphire crystal) and dispersion balancing components, in our case double chirped mirrors (DCMs). The system can be decomposed into the linear resonator arms and the nonlinear gain crystal, see Fig. 3-2[43]. To achieve the shortest pulses, the net dispersion in the cavity should be close to zero. However, the dispersive elements individually produce significant group delay over the broad bandwidth of the laser pulse. It has been shown in [46] that nonlinear propagation along dispersion-managed fiber near zero net GDD possesses a narrower spectrum in the segment of positive dispersion than in the segment of negative dispersion. Thus, the effect of negative dispersion is greater than that of the positive dispersion and imparts to the pulse an effective net negative dispersion. This effective negative dispersion can balance the Kerr-induced phase, leading to steady-state pulses analogous to the soliton case discussed above, but they are not secant-hyperbolic in shape. Figure 3-3, taken from [43] shows a numerical simulation of a self-consistent solution of the pulse propagation problem over one round trip through the resonator. But in contrast to Eq. 3.16, here the pulse undergoes large changes in one round trip due to the discrete positioning of the different elements, and the equation needs to be formulated, analogously to the NLSE, in terms of the longitudinal variable z . The pulse first propagates in a linear medium with negative dispersion and then propagates in a nonlinear medium with positive dispersion and self-phase modulation. This is accounted for in the modified master equation by making the coefficients functions of the longitudinal variable z . Implicit in the transformation of variables from T to z the coefficients D_2 , δ , g , l and q are now defined per

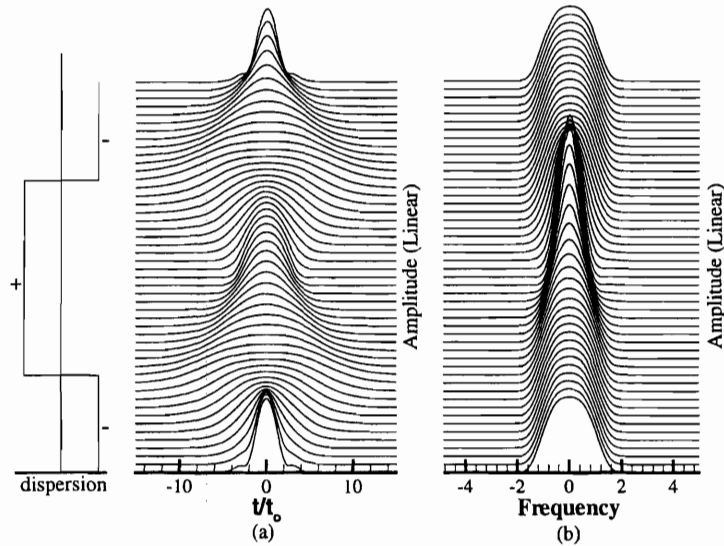


Figure 3-3: Numerical simulation of pulse shaping over one round trip in the resonator. (a) and (b) represent the pulse width in the time and frequency domain, respectively. The dispersion map can be seen on the left-hand side.

unit length. The modified master equation for the case of dispersion-managed soliton formation is given by

$$\frac{\partial A(z, t)}{\partial z} = \left[-iD_2(z) \frac{\partial^2}{\partial t^2} + i\delta(z) |A(z, t)|^2 + g(z) \left(1 + \frac{1}{\Omega_g^2} \frac{\partial^2}{\partial t^2} \right) - l(z) - q(z) \right] A(z, t). \quad (3.19)$$

The steady-state pulse formation can be understood in the following way. By symmetry the pulses are chirp-free in the middle of the crystal. A chirp free pulse starting in the center of the gain crystal, i.e., nonlinear segment, is spectrally broadened by the self-phase modulation and disperses in time due to second order dispersion, which generates a linear chirp over the pulse. Subsequently, the pulse experiences negative dispersion in the arms of the laser resonator, which compresses the dispersed pulse to its transform limit at the end of each arm, where an output coupler can be placed. Back propagation towards the crystal imposes a negative chirp, generating the time reversed solution of

the corresponding master equation. Therefore, subsequent propagation in the nonlinear crystal is compressing the pulse spectrally and temporally to its initial shape in the center of the crystal. As can be seen in Fig. 3-3, the pulse width can vary substantially within a round trip. This fact will be important in our later analysis of the nonlinear contributions to the carrier-envelope frequency of octave-spanning lasers.

In a laser where the negative dispersion is equally distributed in both arms of the resonator, which is the case for the octave-spanning laser described here, the pulse runs through the dispersion map twice per round-trip. The pulse is short at each end of the cavity and, most importantly, the pulses are identical in both paths through the crystal, which exploits the KLM action twice per round trip [47] in contrast to an asymmetric dispersion distribution in the resonator arms, as is the case for lasers with intracavity prisms for dispersion compensation. Thus, a symmetric dispersion distribution may lead to an effective saturable absorption that is twice as strong as an asymmetric dispersion distribution, which results in substantially shorter pulses in prism less lasers.

In octave-spanning lasers, the observed output spectrum extends well beyond the gain bandwidth of Ti:sapphire. Rather, the mirrors and output couplers are what form a hard spectral filter for the pulse. In this case, the saturable absorber action is strong enough to generate spectrum beyond the high reflectivity bandwidth of the output coupler and the output spectrum shows strong wings due to the enhanced output coupling. This will become evident when we show the experimental results in Chapter 4. The pulse is still shaped by the interplay between dispersion and self-phase modulation analogous to soliton formation. However, this pulse is not stable in the presence of a finite spectral filter bandwidth. Stabilization is achieved by saturable absorber action due to KLM that favors the pulse and suppresses background radiation that can benefit from the peak of the gain at the passage of the pulse through the crystal.

3.3 Technical challenges in generating octave-spanning spectra

To make use of the full potential of the dispersion-managed soliton pulse formation, several technical challenges need to be overcome. We will highlight here the three most important aspects to be considered in the design of such ultrabroadband lasers.

3.3.1 Resonator design

The first important aspect in designing octave-spanning lasers is to incorporate the Kerr effect into the laser design, by finding a configuration which maximizes the artificial saturable absorber action in the laser crystal. As mentioned earlier, fast saturable absorption is obtained by combining the self-focusing due to the Kerr effect in the crystal with a soft aperture caused by the proper selection of the pump mode size in the crystal. In this case, the change in the beam waist enhances the overlap between the laser mode and the pump mode and therefore enhances the gain of the self-focused laser mode, as can be seen in the schematic in Fig. 3-4.

The proper resonator design for optimum KLM is a complex, time-consuming problem. In order to map out the complete parameter range of the laser system, a complete spatiotemporal evolution of the pulse needs to be done numerically, until steady state is reached, which is a challenging task even with today's computers. However, a resonator design based on ABCD matrices similar to Eq. 2.5 or q-parameter analysis, where the KLM is modeled by an intensity-dependent lens, already gives a good starting point for the laser construction. The final optimization is then done by the experimentalist by varying the cavity parameters in order to achieve the strongest KLM, i.e., broadest spectrum. More details on the optimization process will be given in the next chapter.

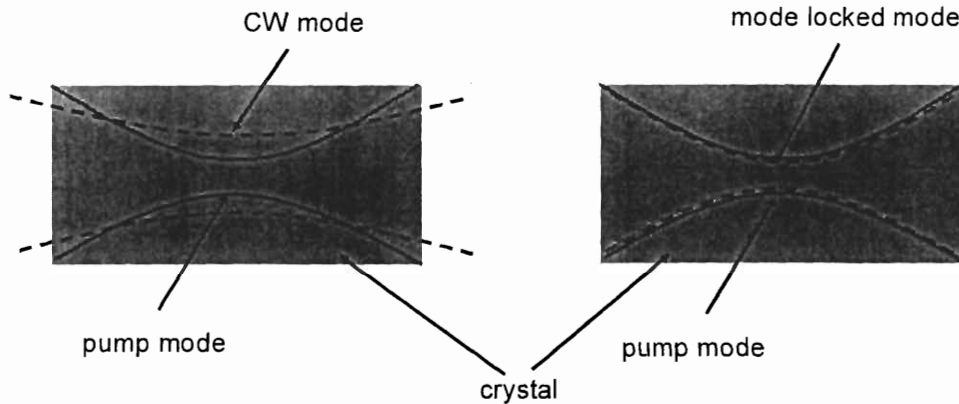


Figure 3-4: Schematic of soft aperture effect due to differentiation between pump mode size and CW operation mode size. Gain is enhanced in mode locked operation due to better overlap with gain region, given by the pump mode volume.

3.3.2 Dispersion management

The second essential element in the generation of octave-spanning spectra is a mirror technology that supports an octave-spanning spectrum with high reflectivity and custom designed dispersion properties. For this purpose, Kärtner *et. al* invented so-called double-chirped mirror pairs (see Figs 3-5 and 3-6). DCMs have been developed to enable precise dispersion control and high reflectivity simultaneously over a fractional bandwidth of as much as $\Delta f/f_0 = 0.4$, where f_0 is the center frequency of the pulse [48][49]. DCMs work on the principle of chirped mirrors, where the Bragg wavelength of the mirror pairs is continuously chirped to generate a wavelength-dependent penetration depth into the mirror. However, chirping of the Bragg wavelength is not enough to accomplish this. In addition to the Bragg wavelength, impedance matching has to be ensured such that the waves do not encounter spurious reflections before the turning point in the mirror is reached. Both the Bragg wavelength and the impedance matching have to be tuned over the operation wavelength of the mirror which is emphasized by the name double-chirped mirror[49]. Most importantly to avoid reflections at the surface of the mirror to the air, a high quality antireflection (AR) coating is necessary. To avoid spurious

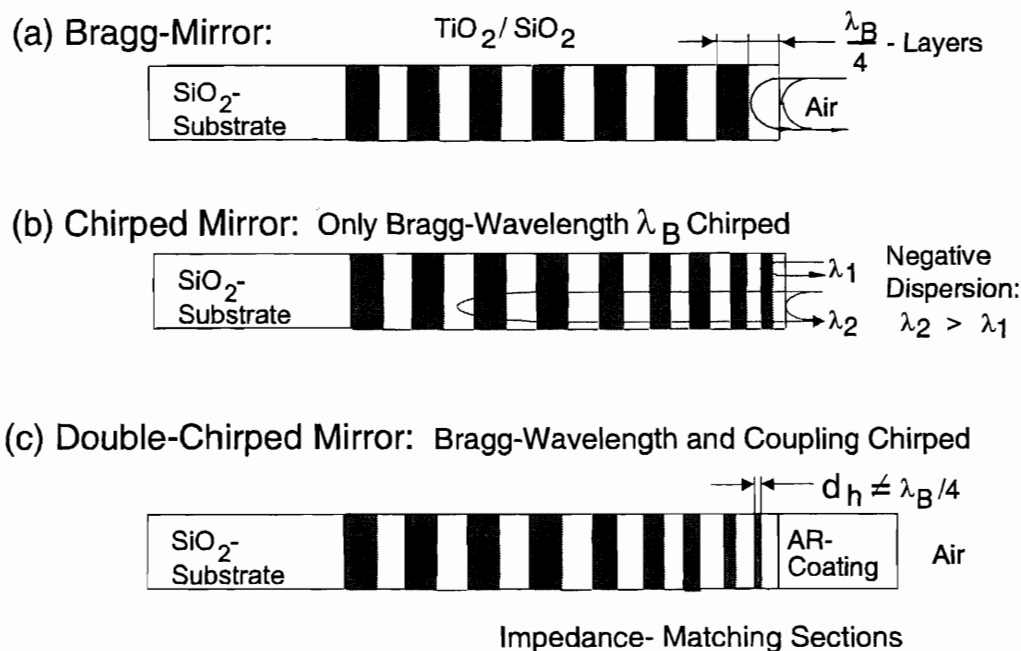


Figure 3-5: (a) Standard Bragg mirror, (b) simple chirped mirror, (c) double-chirped mirror (DCM) with matching sections to avoid residual reflections that cause undesired oscillations in the group delay [43].

reflections during propagation through the grating structure, the grating is switched on adiabatically by increasing the thickness of the high index layer continuously from small values to a quarter wave thickness, see Fig. 3-5(c). However, to extend this concept to cover one full octave, i.e., $\Delta f/f_0 = 0.66$, the requirements on the quality of the AR coating of such mirrors become impossible to realize and even after re-optimization of the mirror, a small amount of impedance mismatch is still present leading to undesired large oscillations in the GDD.

The high reflectivity range of the back mirror can easily be extended to one octave by simply chirping slow enough and a sufficient number of layer pairs. However, the smooth-

ness of the resulting GDD strongly depends on the quality of the matching provided by the AR coating.

The reflections occurring at the AR coating, similar to those in Gires-Tournois interferometers (GTIs), add up coherently when multiple reflections on chirped mirrors occur inside the laser over one round trip, leading to pre- and post pulses if the mode locking mechanism is not strong enough to suppress them sufficiently. Experimental results indicate that a residual reflection in the AR coating of $r < 0.01$, depending on the number of reflections per round trip, is required so that the pre- and post pulses are sufficiently suppressed. This corresponds to an AR coating with less than 10^{-4} residual power reflectivity, which, for a bandwidth approaching one octave, is not any longer possible. A way out of this limitation is offered by the observation that a coherent subtraction of the pre- and post-pulses to first order in r is possible by reflections on a mirror pair M1 and M2, see Fig. 3-6. A series of two reflections on mirror M1 and on a similar mirror M2 with an additional phase shift of π between the AR coating and the back mirror leads to coherent subtraction of the first-order GTI effects.

Figure 3-7 shows in the top graph the designed reflectivity of both mirrors of the pair in high resolution taking into account the absorption in the layers. The graph below shows the reflectivity of the mirror, which has in addition high transmission between 510-550 nm for pumping of the Ti:sapphire crystal. Each mirror consists of 40 layer pairs of SiO₂ and TiO₂ fabricated using ion-beam sputtering [51][52]. The design was done by Franz Kärtner and the mirror dispersion measurements were performed by Onur Kuzucu [53]. Both mirror reflectivities cover more than one octave of bandwidth from 580 to 1200 nm or 250 to 517 THz, with an average reflectivity of about 99.9% including the absorption in the layers. In addition, the mirror dispersion corrects for the second- and higher-order dispersion of all intracavity elements. The choice for the lower wavelength boundary in dispersion compensation is determined and limited by the pump window of Ti:sapphire. The oscillations in the group delay of each mirror are about 10 times larger than those of high-quality DCMs covering 350 nm of bandwidth[47]. However, in

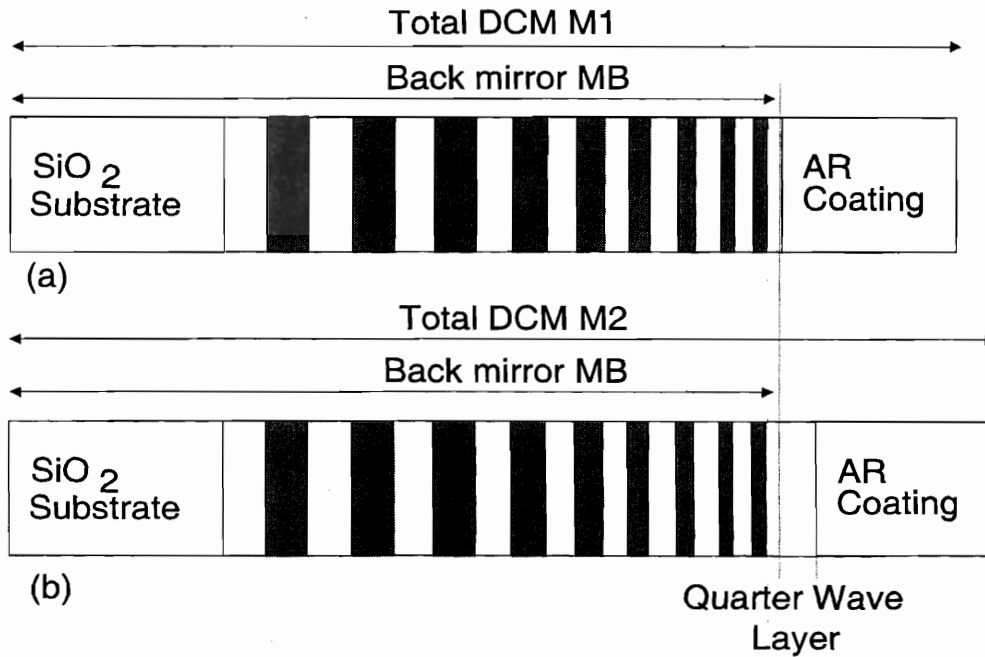


Figure 3-6: DCM pair consisting of DCMs M1 (a) and M2 (b). M1 can be decomposed into a double-chirped back-mirror BM matched to a medium with the index of the topmost layer. In M2, a layer with a quarter-wave thickness at the center frequency of the mirror and an index equivalent to the topmost layer of BM is inserted between the back mirror and the AR coating. The new mirror containing BM and the quarter-wave layer can be re-optimized to achieve the same phase as M1 with an additional π phase shift over the whole octave of bandwidth [50].

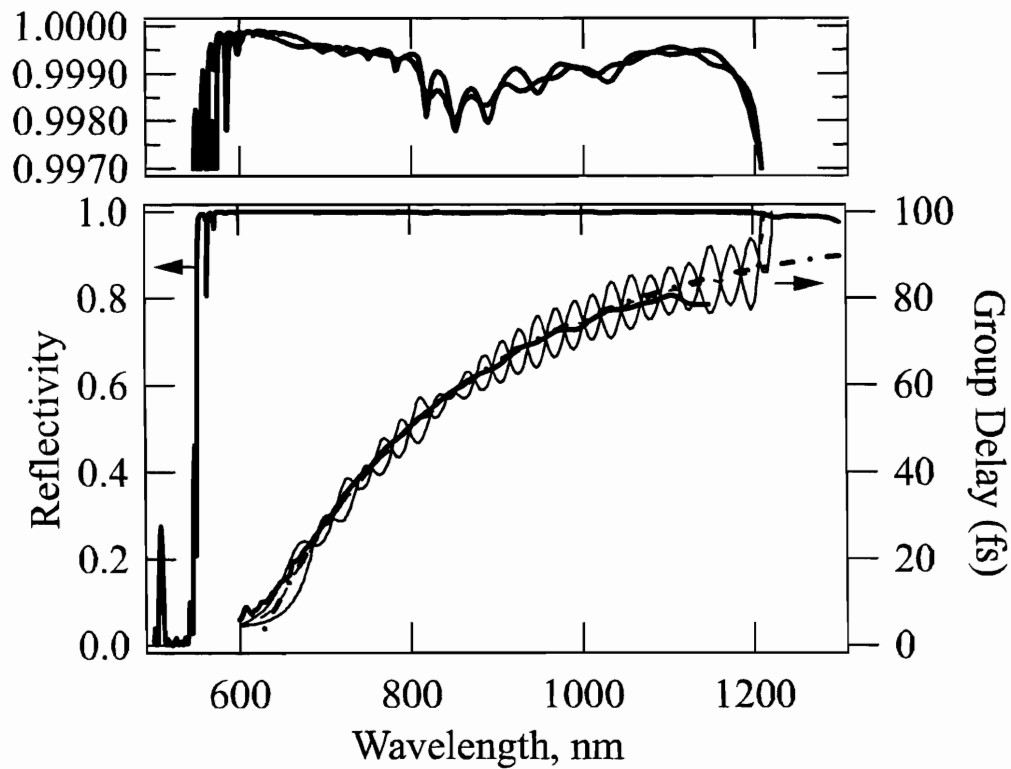


Figure 3-7: Reflectivity (left scale) of the type I DCMs shown as thick solid line. The group delay design is given by the thin dashed line. The individual group delays (right scale) of type I and II DCMs are shown as thin lines and its average as a thick-dotted line, which is almost identical to the design goal over the wavelength range of interest from 650-1200 nm. The measured group delay, using white light interferometry, is shown as the thick grey line from 600-1100 nm. Beyond 1100 nm the sensitivity of Si detector limited the measurement [29].

the average group delay of both mirrors the oscillations are ideally suppressed due to cancellation by more than a factor of ten. Therefore, the effective residual reflectivity of the mirror pair covering one octave, r^2 , is even smaller than that of conventional DCMs. Because of slight fabrication errors the oscillations in the group delay still do not precisely cancel, especially close to 900 nm and 1000 nm deviations from the design goal on the order of 1-2 fs occur, which will lead to observable spectral features in the spectral output of the lasers described in chapter 4.

3.3.3 Output coupler design

The last key element in the laser design is the output coupling mirror. In order for an ultrashort pulse to build up in the laser cavity, the output coupler should have a large enough reflectivity bandwidth as not to impose significant spectral filtering on the pulse. However, to perform direct $f - 2f$ detection from the laser, the wings of the spectrum need to be enhanced by increased output coupling relative to the center of the spectrum. Therefore, the reflectivity curve of the output coupler has to be chosen to balance these two effects. In the next chapter, we will show experimental results which illustrate the importance of this effect.

Unfortunately, engineering a broadband reflectivity OC with no penalties to the GDD is not an easy task. If the ripples in the GDD are too large, they will prevent the mode locking completely. In order to employ a simple quarter-wave dielectric stack which presents no dispersion ripples, the bandwidth which can be obtained is essentially determined by the index contrast of the high- and low-index layers. The best material combination which we have found that can provide a high contrast and at the same time be deposited on the substrate with reasonable precision is ZnSe/MgF₂. With such structure we have designed output couplers which successfully produce broadband spectra as will be shown in chapter 4. They have a 1% transmission from 750 nm to 950 nm, as can be seen in Fig. 3-8.

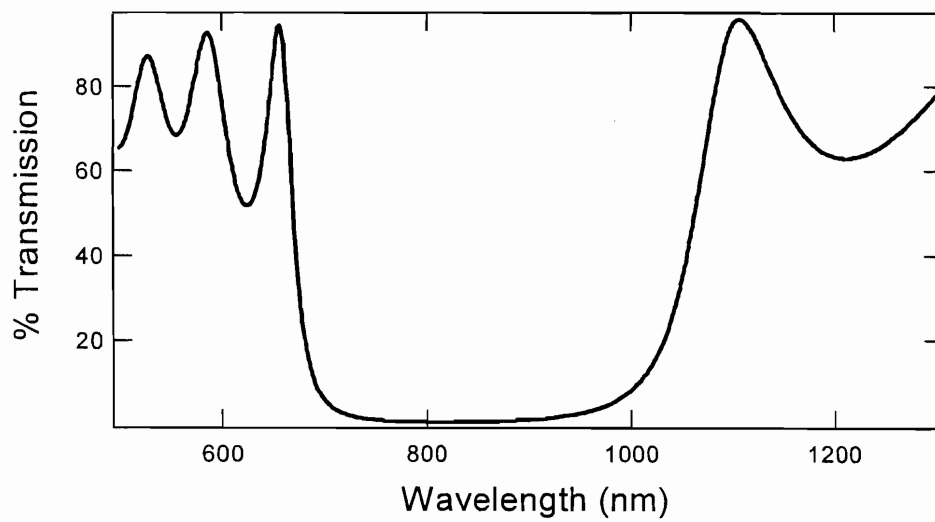


Figure 3-8: Measured transmission of ZnSe/MgF₂ quarter-wave dielectric stack. This output coupler successfully generated stable octave-spanning spectra. As the plot shows, the bandwidth of the transmission curve does not span a full octave, rather it is obtained by enhancement of the spectral wings due to increased output coupling at the f and $2f$ points.

Chapter 4

Octave-spanning laser: experimental results

At the beginning of this thesis project, at the end of 2001, self-referencing directly from the laser had been demonstrated by Ell *et. al* [28]. The cavity design consisted of DCM pairs and a prism sequence for dispersion compensation and a second intracavity focus on a BK7 plate to enhance the SPM. The measured f_{CE} beats had a signal-to-noise (S/N) ratio of 20 dB at most, which was insufficient for phase-locking without cycle slips. This setup was unduly complex because of the prism sequence and the second intracavity focus. Therefore we aimed for elimination of the second focus and the prism sequence by an improved DCM design which supported on its own the generation of octave-spanning spectra.

By the end of 2002, such design had become a reality when the coating run to produce the DCM pairs described in Section 3.3.2 was successful. A prismless, octave-spanning laser was now possible and by May of 2003, we had demonstrated an 80 MHz repetition rate laser with direct self-referencing [54]. Subsequently, built a higher repetition rate laser at 191 MHz with some technical improvements and also improved the setup for f_{CE} detection . This is the setup currently in use and the technical description that follows will focus on it entirely, although there is fundamentally no difference between the two

generation of lasers (the 80 MHz and the 191 MHz). For specific details on the 80 MHz laser setup, see reference [29]. The first demonstration of a 200 MHz laser was done by Oliver Mücke, and is described in reference [55].

4.1 Resonator design

The octave-spanning laser demonstrated here consists of an astigmatism-compensated cavity (see Fig. 4-1). The gain medium is a 2 mm long Ti:sapphire crystal with an absorption of $\alpha = 4.1 \text{ cm}^{-1}$ at 532 nm. The laser is pumped by a diode-pumped, frequency-doubled Nd:YVO₄ laser, Millennia Xs by Spectra-Physics. The radius of curvature (ROC) of the folding mirrors is 7.5 cm, and the pump lens has a 50 mm focal length. All mirrors in the cavity, except for the end mirrors, are type I (grey) and type II (white) DCMs that generate smooth group-delay dispersion when used together in pairs, as already described in Section 3.3.2. Because an exact number of pairs is necessary for proper dispersion balancing, one cavity end mirror needs to be an "inert" mirror, with no contributions to the overall cavity dispersion. To achieve this we employed a silver mirror, which generates minimum phase distortion to the pulse. Despite contributing to great losses which deteriorate the laser efficiency, the characteristic broad bandwidth of these mirrors ($R > 95\%$ from 450 nm to 12 μm) has so far been essential for successful broadband generation. The other cavity end mirror consists of an output coupler, with the broadband design demonstrated in Section 3.3.3. The output power in CW operation is typically 70 mW with 5.5 W pump power. In mode-locked operation, the average power is 200 mW. Specific details of the cavity elements are given in table 4.1.

We have tried implementing different broadband output couplers to replace the silver mirror in the cavity. The idea behind this was to make use of the power which is "dumped" in the silver mirror and have a laser with two useful optical outputs and twice the output power. In a metrology experiment for example, one could use one output exclusively for f_{CE} detection and the other output for beating with the cw lasers employed

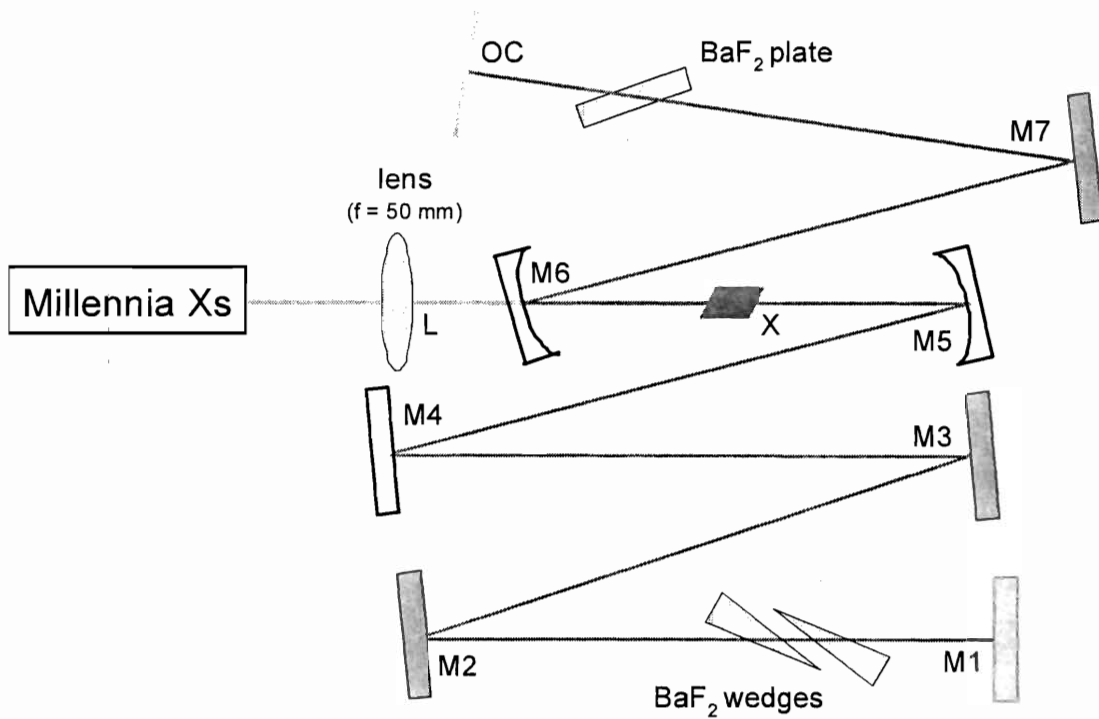


Figure 4-1: Schematic representation of the laser cavity. The lengths of the different segments as well as the incidence angles are indicated in table 4.2.

in the spectroscopy. This would mean enhanced S/N in the optical beats since currently separating the spectral wings from the remainder of the spectrum unavoidably results in optical losses. However, these trials were never successful, most likely because the spectral filter imposed by an extra output coupler, which effectively created enhanced losses to the pulse, became too strong and the strength of the KLM was no longer able to sustain stable short pulse operation. As discussed in Section 3.3.3, designing a transmissive mirror with a bandwidth which supports the generation of our short pulses and causes no damage to its phase is a technically challenging task.

element	description
M1	New Focus model 5103 silver coated mirror, minimal phase distortion
M2, M3 and M7	DCM, R (right)
M4, M5 and M6	DCM, L (left)
L	Newport XPX049AR.14 PCX lens, $f=50.2$ mm
X	Ti:Al ₂ O ₃ , 2.15 mm path length (~ 1.9 mm thick), $\alpha = 4.1$ cm ⁻¹
OC	MgF ₂ /ZnSe quarter wave stack at 800 nm, 1 mm thick.
BaF ₂ plate	1 mm thick.
BaF ₂ wedges	1.65 mm on thin end, 1.95 mm on thick end, 2.5 cm length.

Table 4.1: Table indicating all cavity optical elements, with specifications and part numbers, where present

geometric quantity	value
$\overline{M1M2}$	163 mm
$\overline{M2M3}$	65 mm
$\overline{M3M4}$	83 mm
$\overline{M4M5}$	176 mm
$\overline{M5M6}$	80 mm
$\overline{M6M7}$	147 mm
$\overline{M7OC}$	70 mm
\overline{LX}	58 mm
$\overline{M6X}$	38 mm
$\overline{XM5}$	42 mm
$\angle M2, \angle M3, \angle M7$	19.6°
$\angle M4, \angle M5, \angle M6$	11°

Table 4.2: Relevant geometrical values of laser cavity

In one round trip of the laser pulse through the cavity, the 12 bounces on DCMs

generate the precise negative dispersion required to compensate for the positive second- and up to sixth-order dispersion caused by the laser crystal, the air path in the cavity, and the BaF₂ plate and wedges used to fine-tune the dispersion. We used BaF₂ for dispersion compensation because it has the lowest ratio of third- to second-order dispersion in the wavelength range from 600 – 1200 nm and the slope of the dispersion of 0.5 mm BaF₂ is nearly identical to that of 1 m of air. This makes it possible to scale the cavity length and repetition rate without changing the overall intracavity dispersion, simply by removing air path and correspondingly adding BaF₂ to maintain the proper dispersion balancing. This is not possible in lasers with intracavity prisms because a minimum distance between the prisms is required to provide negative dispersion.

The dispersion measurements showed in Fig. 3-7 were performed with each mirror of the pair under a different incidence angle of the beam. The design was intended for both mirrors under an angle close to the astigmatism compensation angle for 10 cm curvature cavity mirrors, 11°. That way, each of the curved mirrors would be of a different kind. However, due to fabrication tolerances it turned out that putting one of the mirrors at the astigmatism angle and the other at 19.6° was what lead to the best dispersion compensation. At these angles, the oscillations in the GVD were minimized as the measurement shows. This explains the arrangement of the DCMs in the cavity in Fig. 4-1, both curved mirrors being of the same DCM type. Table 4.2 gives all the relevant distances and incidence angles for the laser cavity.

Besides choosing the cavity length based on the desired repetition rate for the laser, it is important to verify that the laser mode has the proper size. As already explained, the laser mode must be larger than the pump mode in order to generate a soft aperture for the Kerr-lens mode-locking. This requires a simulation in which the ABCD propagation matrix for the cavity determines the mode size in the crystal. It has been shown, by computer simulations and experiments that Kerr-lens mode-locking is strongest for an asymmetric cavity[53]. The arm ratio as well as the cavity length can be fine tuned in the simulation to obtain the desired mode size. Figure 4-2 shows such a simulation for

the laser cavity in consideration, the values used being the ones given in table 4.2. The plot shows the mode size as a function of the distance between the curved mirrors. In this simulation, for simplicity the crystal is not considered and astigmatism is not taken into account. It is used as a starting point to assure the existence of a stable resonator and the larger mode size relative to pump size. The asymmetry in the resonator creates two stability regions, given by the two maxima in the plot. The pump mode size has been calculated to be $w_{0p} = 13 \mu\text{m}$, which corresponds to a confocal distance equal to the crystal length of 2 mm. We have experimentally observed that the operating points which allow for the strongest KLM and therefore the shortest pulses are the inner parts of the stability regions for the asymmetric cavity, as shown in Fig. 4-2. We can see that in this region, the mode size varies from 15 to 19 μm , which is larger than the pump mode size. This plot helps to explain how the mode-locked operation is initiated in the laser. When the laser is in such instability region, the mode size is extremely sensitive to the distance d between the folding mirrors. Therefore it is easy to generate a large decrease in the mode size and a corresponding increase in the intensity by simply "jiggling" any mirror in the cavity. In this process, several longitudinal modes are generated and locked by the saturable absorber action, which generates an intensity spike that initiates the pulse formation process.

To achieve mode-locked operation, it is usually necessary to reduce the amount of BaF₂ inside the laser cavity (by withdrawing one of the wedges). The broadest spectrum can be achieved by optimizing the insertion of the BaF₂ wedge. The spectral width of the laser critically depends on the dispersion balance. With the prismless lasers adjusting the dispersion does not significantly change the cavity alignment. In contrast to prism-compensated cavities, a slight misalignment of the resonator does not affect intracavity dispersion. Consequently, the alignment is robust and as a result it is possible to operate the laser in octave-spanning mode for as much as a few days without interruption.

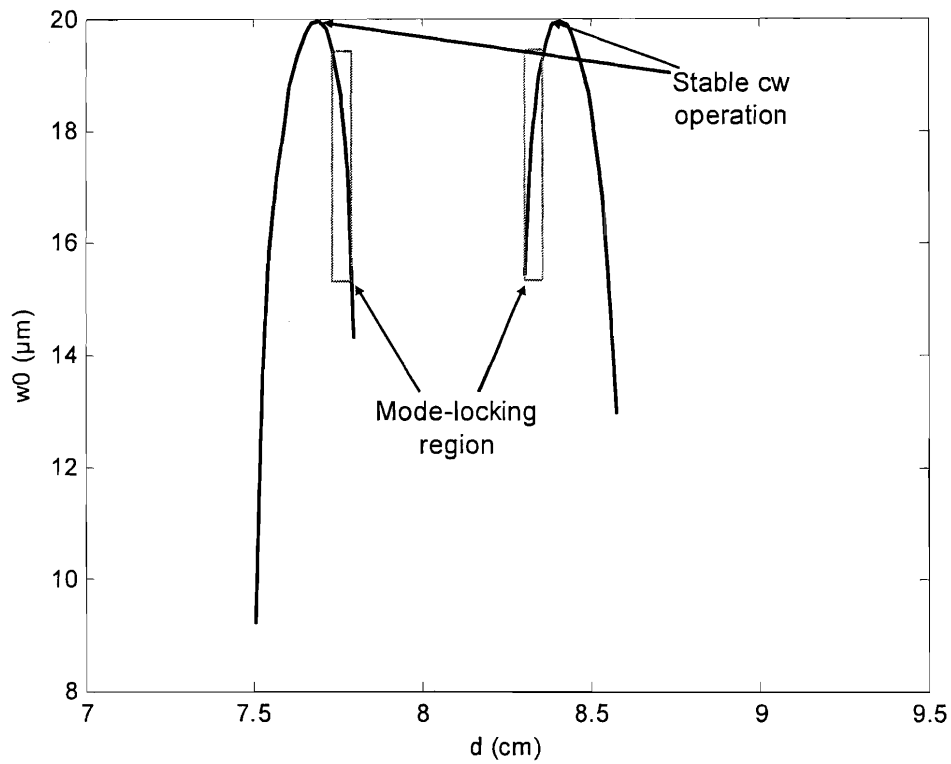


Figure 4-2: Results of computer simulation to determine the waist size in the crystal as a function of the distance between the curved mirrors. It has been empirically verified that the optimum mode-locking region is the one indicated in the plot. Also shown are the stable cw operating points.

4.2 Results

4.2.1 Generating ultrabroadband spectra

Figure 4-3 shows the spectrum of the 191 MHz laser under broadband operation. The octave is reached at a spectral density about 25 dB below the average power level. The same plot also shows the OC reflectivity curve. As explained in Sec. 3.3.3, the width of the output spectrum depends upon the detailed shape of this reflectivity curve which significantly enhances the spectral wings and simultaneously allows for spectral buildup inside the cavity. To show that our prismless lasers are indeed scalable while still producing broadband spectra, we show in Fig. 4-4 the spectrum for the 80 MHz laser and the 191 MHz laser. The overall structure of the two lasers is the same, with the only significant difference being, besides the different cavity lengths and corresponding BaF₂ insertion, that they employ different output couplers. They are of the same type (MgF₂/ZnSe quarter-wave stack) but with slight design differences. Although small, these differences can be noted in the spectra. For example, the 191 MHz (grey trace in the figure) laser has a more pronounced spike in the low wavelength due to a correspondingly pronounced feature in its OC not present in the 80 MHz laser OC. In the long wavelength, the slightly larger bandwidth of the 191 MHz laser OC results in a slightly broader spectrum for that laser. The experimentally observed spectra represent stable laser operation and sufficient power at the f and $2f$ points for f_{CE} detection.

4.2.2 Importance of the output coupler design

To investigate the importance of the output coupler design in the output spectrum, we have measured the intracavity and external spectra, as well as output coupler transmission curves, for two different output couplers OC1 and OC2, which can be seen in Fig. 4-5. In the case of OC1, the output coupler is a strong spectral filter in the laser, which limits the spectrum that can be generated to a bandwidth similar to that of the transmission curve. Although there is some enhancement of the spectral wings, it is not sufficient

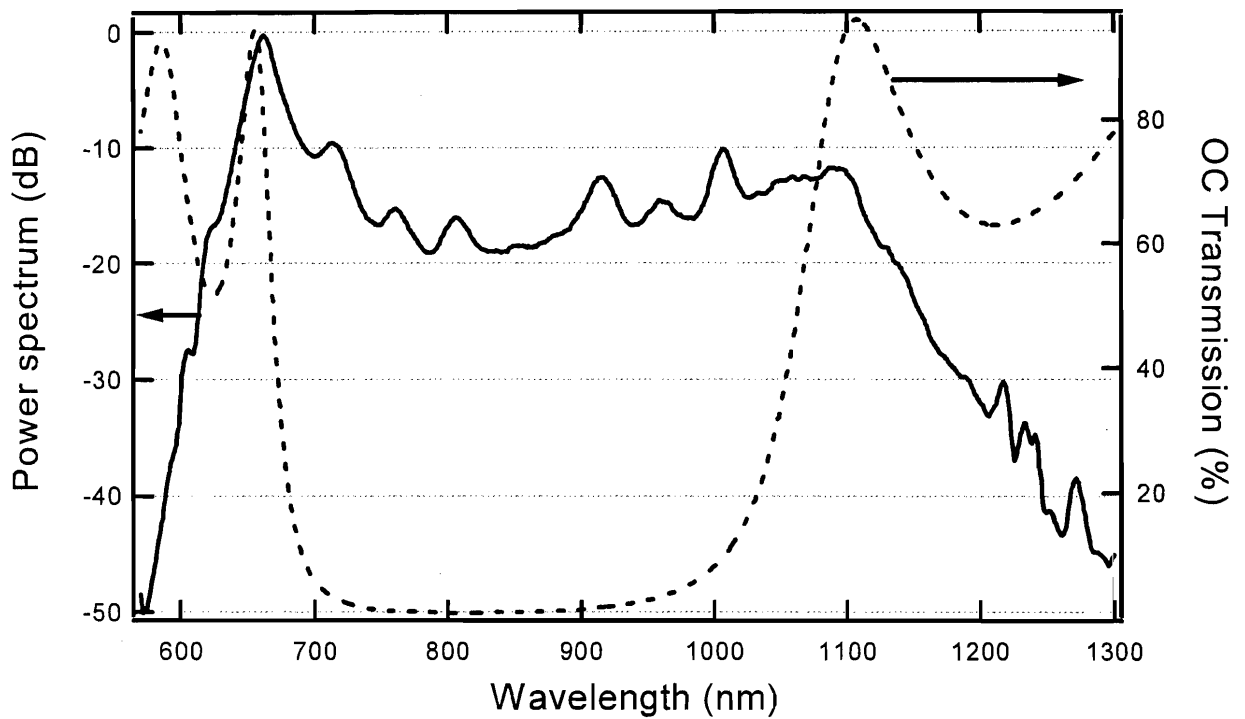


Figure 4-3: Spectrum of octave-spanning laser at 191 MHz, with scale on the left; transmission of output coupler with scale on the right. It is clear from this figure that the output coupler strongly shapes the spectrum. The octave is reached at 20 dB below the average power level.

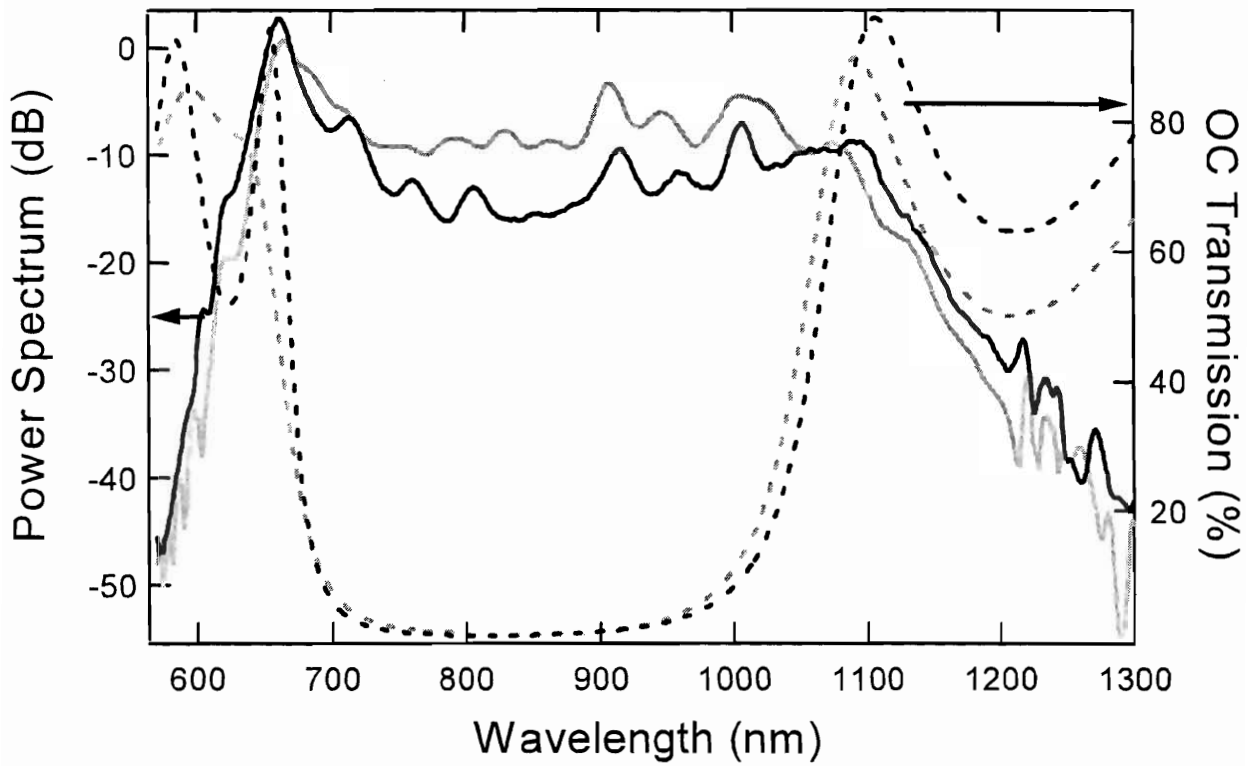


Figure 4-4: Spectrum (solid curves) and corresponding output coupler transmissivity curve (dashed curves) for 191 MHz and 80 MHz repetition rate lasers (blue and red, respectively). The similarity in the spectrum confirms the scalability of the repetition rate in prismless lasers.

to achieve enough power at the f and $2f$ points. In contrast, in the case of OC2 the spectral filter is relatively weak which allows a broader pulse to be generated inside the cavity, and properly enhanced to achieve significant power at the spectral wings. Even though the spectrum shown in Fig. 4-5 (b) is of the broadest we have observed, long term stable mode-locked operation was never achieved with these OCs. It is believed that this is due to ripples in the measured dispersion profile that affected the laser operation [53].

4.2.3 Generating the carrier-envelope beat signal

Even though the spectra just shown suggest that the laser is indeed octave-spanning, the only useful definition of octave-spanning is that the laser can be self-referenced directly from its output. Observing the spectrum however is the first step in the laser optimization process and a reference spectrum should always be kept in case of accidental misalignment.

Self-referencing, as already described, involves referencing the laser to itself by beating the second harmonic of the long wavelength part of the spectrum with the short wavelength part, which gives a direct measurement of f_{CE} as Eq. 2.12 shows in the case of octave-spanning spectra. The self-referencing setup built for the 191 MHz laser represents a major improvement over the previous one used in the 80 MHz laser frequency comb: there, to generate an f_{CE} beatnote with sufficient S/N for phase locking without cycle slips (minimum 30 dB in 100 kHz resolution bandwidth), the short- and long-wavelength portions of the laser spectrum were spatially separated (using a dichroic mirror in a Mach-Zehnder type interferometer), the long-wavelength portion was frequency doubled in a second-harmonic generation (SHG) crystal (BBO), and the short-wavelength fundamental light and the SHG light were recombined again, as can be seen in Fig. 4-6a. The wavelength components that interfere with each other generating the carrier-envelope beatnote could be overlapped in space and time. However, maintaining this overlap over long periods of time was a challenge. This interferometer setup was bulky and extremely alignment sensitive. On a day to day operation, a significant amount of time was spent

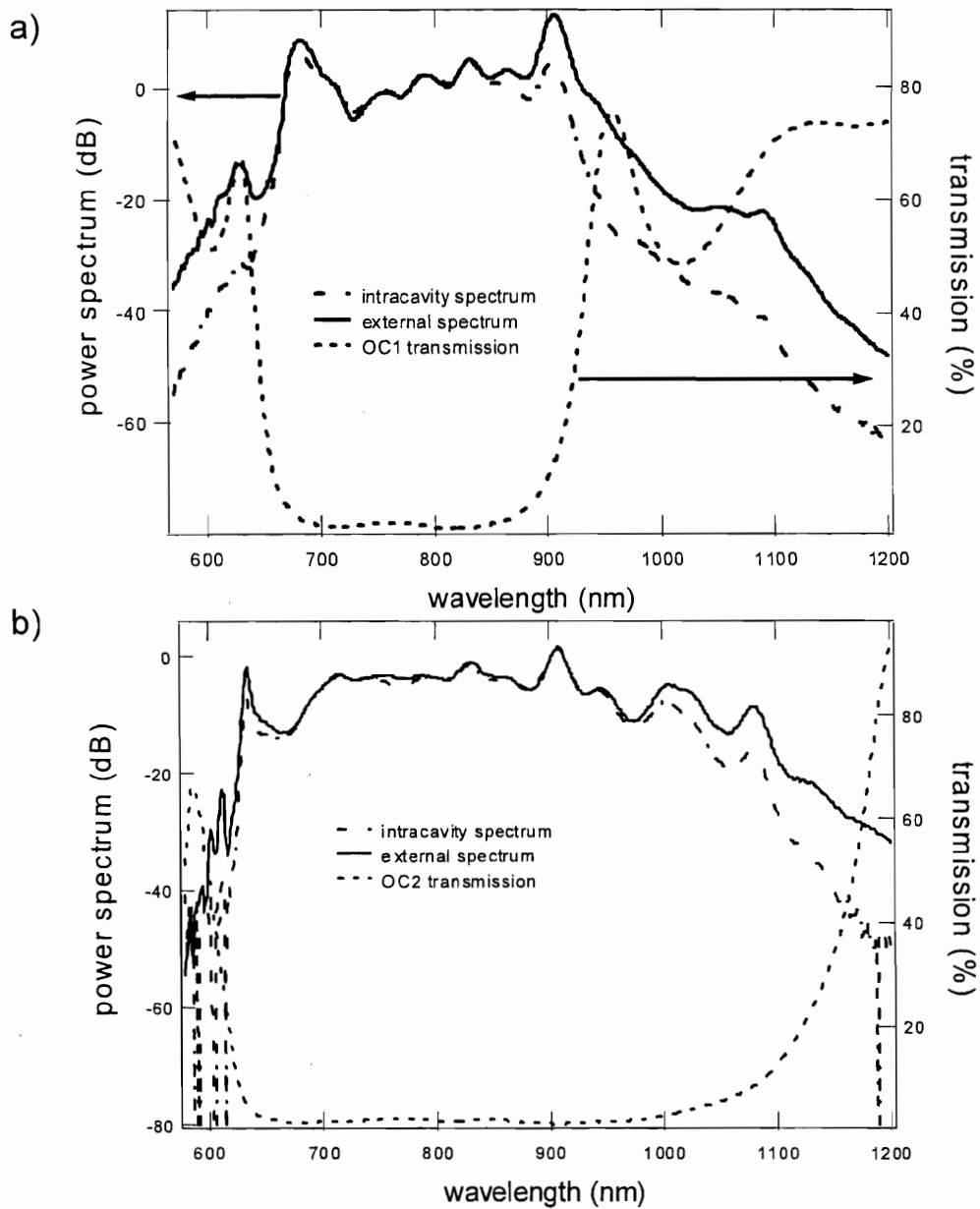


Figure 4-5: Output spectra (solid curves) and intracavity spectra (dash-dotted curves) generated by a 80 MHz Ti :sapphire laser using (a) a broadband output coupler OC1, and (b) an ultrabroadband output coupler OC2. The output coupler transmission (black dashed curves) are shown for comparison.

simply realigning this setup, which was almost always necessary due to the natural change in the laser alignment.

In the current setup (see Fig. 4-6b), in contrast, the time delay between the 570 and 1140 nm spectral components used for $f - 2f$ self-referencing is produced by 8 bounces on DCMs, which compensates for the total group delay between 570 nm and 1140 nm caused by the optical components in the setup external to the laser (output coupler, BBO crystal and crystal focussing lens). This setup is intrinsically more stable than the above-mentioned interferometric setup, with virtually no need for day-to-day realignment. Spatial overlap is assured since the two wavelength components are never separated. After the DCM-based delay line, the Ti:sapphire output is focused onto a 1 mm thick BBO crystal cut for type I SHG at 1160 nm. The emitted SHG light and the orthogonally polarized fundamental light are projected onto a common axis using a polarizing beam splitter cube. Then it is spectrally filtered using a 10 nm wide interference filter centered at 570 nm, spatially filtered using an aperture, and finally detected using a photomultiplier tube (PMT) (Hamamatsu H6780-20). Although advantageous from the point of view of stability, the DCM-based delay line has a few drawbacks, one being the fact that the control over the time delay generated by the DCMs is discrete, given by the number of bounces multiplied by the group delay of -68 fs between 570 nm and 1140 nm produced in one bounce, whereas in an interferometer based setup it is continuous, which could produce a larger S/N. However, a direct comparison between the two methods has not been performed.

The typical total optical power at 1140 nm is 800 μ W and we observe roughly a conversion efficiency of 10^{-3} . For the fundamental 570 nm light, we observe a few microwatts of average power. These values vary from day to day laser operation. However, the fundamental and doubled optical power do not fully contribute to the measured beat signal. This is due to the difference in spatial profile of the transverse modes at these two wavelengths. As can be seen in Fig. 4-3, the power in the spectral wings is produced in a single pass through the crystal and is subsequently almost fully coupled out of the

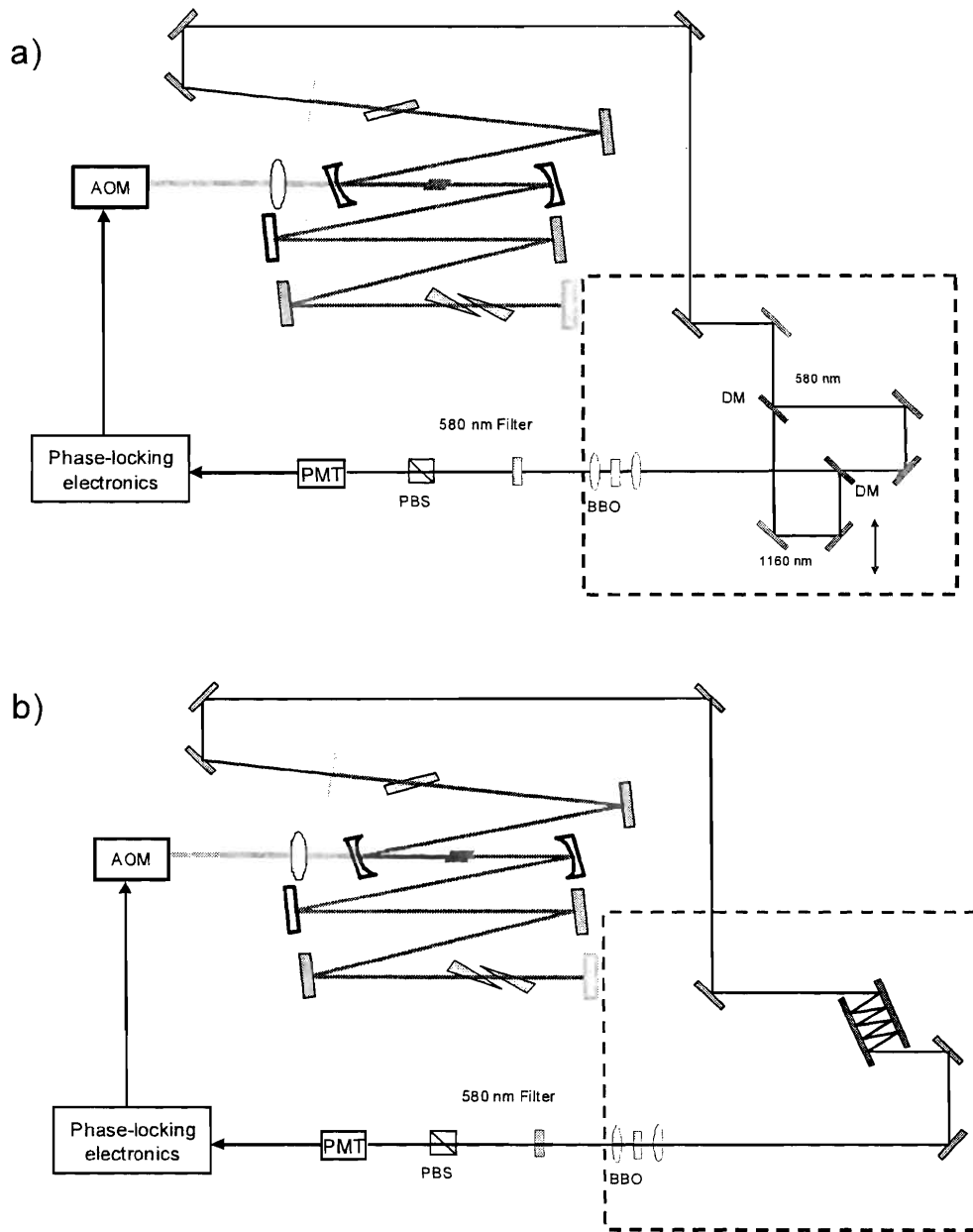


Figure 4-6: Schematic of f_{CE} detection setup for 80 MHz (a) and 191 MHz (b) lasers. The difference is indicated in the dashed region, where a Mach-Zender type interferometer was replaced by a DCM-based delay line. More details in the text.

laser (output coupler transmission is about 80% at 570 nm and 1140 nm). Therefore, it is not necessary that the transverse mode of these spectral components be resonant with the TEM₀₀ mode in the resonator. We have confirmed that the transverse profile of the beam at 800 nm is a good TEM₀₀ mode and deviates from it as the spectral components approach the 3 dB bandwidth of the spectrum. After the aperture which is used for spatial filtering, we observe about 100 nW of average power at 570 nm.

In the RF power spectrum shown in Fig. 4-7, we can see the measured f_{CE} beat as well as its mixing product with the repetition rate signal, both indicated in the figure. The largest spike is the repetition rate signal itself. The measurements indicate a S/N of ≈ 35 dB in a 100 kHz resolution bandwidth. This S/N is sufficient for direct and routine f_{CE} phase stabilization. The f_{CE} beat is intrinsically stable. In the absence of active feedback, the frequency stays within an 8 MHz window for a full day. On the time scale of seconds, it can jitter by about 100 kHz. The next chapter will describe the details of the electronic stabilization systems.

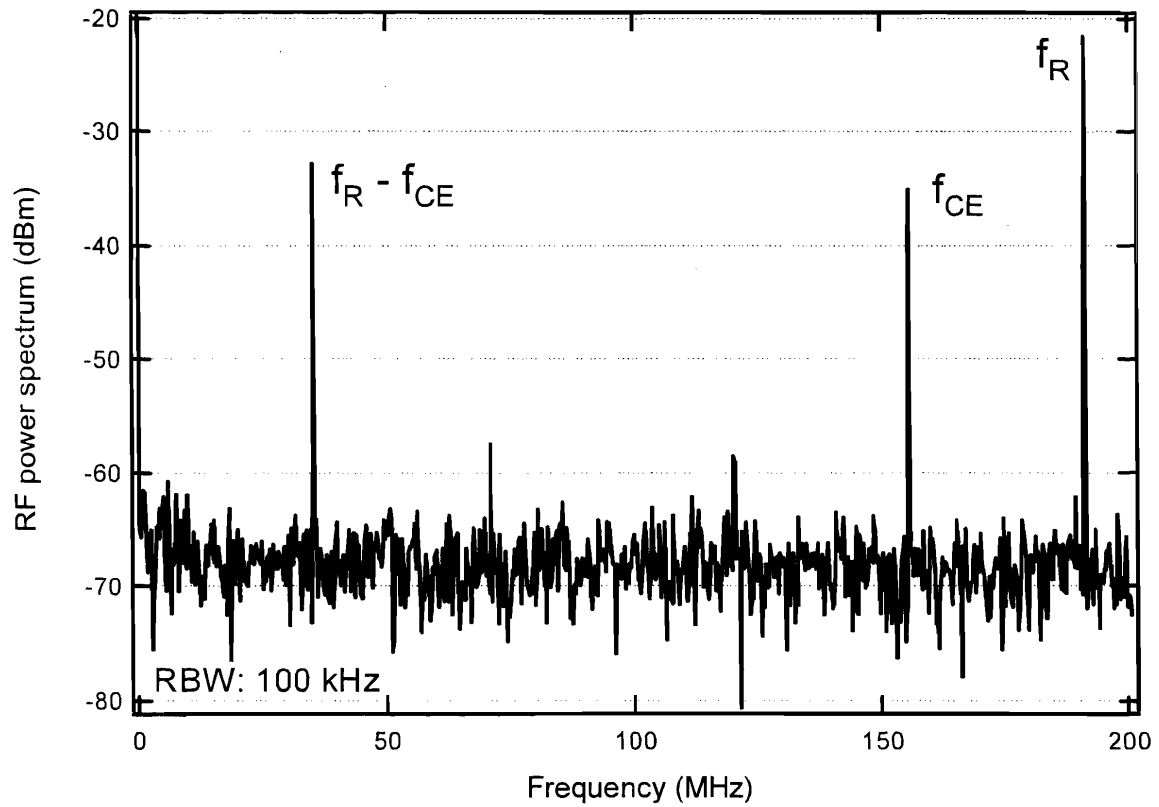


Figure 4-7: Radio frequency spectrum of carrier-envelope beat signal. The two symmetric beat frequencies are the carrier-envelope and its mixing product with the repetition rate, as indicated in the plot. The largest spike, at 191 MHz, is the repetition rate signal. The observed S/N is 35 dB in a 100 kHz RBW.

Chapter 5

Stabilizing the octave-spanning frequency comb

The implementation of octave-spanning frequency combs (OSFCs) as optical rulers requires precise control of the two comb degrees of freedom, f_R and f_{CE} . In this chapter we will describe how this control is implemented in our frequency comb, which is intended for frequency measurements in ultracold hydrogen. In general, the fundamental difference in frequency combs is how their repetition rate is controlled. In some cases a harmonic of the repetition rate is locked to a microwave standard, while in others the repetition rate is stabilized by locking a comb line to a stable optical reference.

All the frequency stabilizing systems described here employ phase-locked loops (PLLs). A beat signal is generated by heterodyning two optical beams. This signal is filtered and sent to a digital phase detector, which generates an error signal. The error signal is properly filtered and amplified, then sent to a transducer that corrects for the error. The signal to the transducer, a voltage, is converted to a frequency change. The transducer is either a PZT that modulates the cavity length (in the repetition rate lock), or an acousto-optic modulator that modulates the pump light (in the carrier-envelope phase control). In either case, the voltage is converted to a frequency, and the process is simply represented by a voltage-controlled oscillator (VCO). Because it is important to understand

the principals of operation, Sec. 5.1 will be dedicated to an overview of the functionality of a PLL. Because digital phase detection is used at the phase detection method in our PLLs, Section 5.2 will be devoted to describing how a digital phase detector works.

5.1 The linear PLL

A PLL is a kind of feedback control system which causes the phase and therefore the frequency of a certain signal to track with that of a reference signal, completely synchronizing the two. In this so called locked state, the phase error between the signal and the reference remains constant over time.

The basic building blocks of a PLL are as follows.

1. A phase detector (PD).
2. A loop filter (LF).
3. A voltage-controlled oscillator (VCO).

These components come together as depicted in the block diagram on Fig. 5-1. The VCO oscillates at a center frequency ω_0 if no voltage is applied to it. The oscillation frequency is then given by:

$$\omega_2(t) = \omega_0 + K_0 u_f(t) \quad (5.1)$$

where ω_0 is the center frequency of oscillation of the VCO and K_0 is the VCO gain.

It is convenient to write the input signal and VCO output respectively as $u_1(t) = A_1 \cos(\omega_1 t)$ and $u_2(t) = A_2 \sin(\omega_2 t + \phi(t))$, where $\phi(t)$ is the time-dependent relative phase between the two signals. The output of the phase detector is then given by:

$$\begin{aligned} u_d(t) &= A_1 A_2 \cos(\omega_1 t) \sin(\omega_2 t + \phi(t)) \\ &= A_1 A_2 \{ \sin((\omega_1 - \omega_2)t - \phi(t)) + \text{high frequencies} \} \end{aligned} \quad (5.2)$$

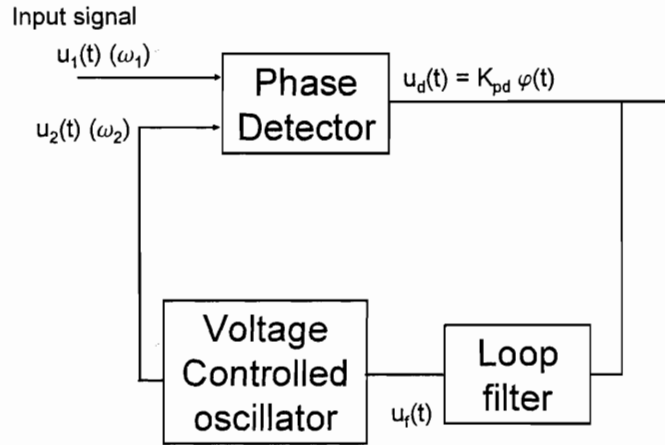


Figure 5-1: Block diagram of linear PLL. The basic building blocks are explained in text.

where the second term is suppressed by low-pass filtering, either in the PD itself or at the loop filter. Since we will be analyzing the case where the system is locked or close enough to locking, we can safely approximate this expression for the moment as

$$u_d(t) = K_{pd}\phi(t). \tag{5.3}$$

where K_{pd} is a proportionality constant given in volts/radian.

We are interested in understanding how the phase of the VCO tracks with that of the reference signal, but the VCO transfers a voltage change into a *frequency* change. Therefore we need to know the *phase* transfer function. Integration of relationship 5.1 gives us the time-dependent VCO phase:

$$\theta_2(t) = \int K_0 u_f(t') dt' + \omega_0 t \tag{5.4}$$

We can take the Laplace transform of the first term in the above equation to find the

frequency response of the VCO:

$$\begin{aligned}
\theta_2(s) &= K_0 L \left\{ \int u_f(t') dt' \right\} = K_0 \int \int e^{st''} u_f(t') dt' dt'' \\
&= \frac{K_0}{s} U_f(s) \\
&= H_{VCO}(s) U_f(s)
\end{aligned} \tag{5.5}$$

Therefore we can see that the VCO represents an integrator for the phase transfer function. In the locks described in the following sections, the equivalent VCO will be composed of different elements. In the f_{CE} lock, a voltage applied to the acousto-optic modulator translates to a shift of f_{CE} , while in the f_R lock, a voltage applied to the piezoelectric transducer translates to a shift of f_R . To analyze the system further, we can investigate the frequency response of the overall system, given by the individual transfer functions of each block.

Knowing the transfer function of the loop filter, $H_{LF}(s)$, allows us to determine the closed-loop transfer function of the PLL. Since we are interested in the residual phase error, we look at the output of the phase detector (see Fig. 5-2). We can apply Black's formula [56] and derive the phase error transfer function:

$$\begin{aligned}
H_{CL}(s) &= \frac{\Delta\theta(s)}{\theta_1(s)} = \frac{K_{pd}}{1 + K_{pd} \frac{K_0}{s} H_{LF}(s)} \\
&= \frac{K_{pd} s}{s + K_{pd} K_0 H_{LF}(s)}
\end{aligned} \tag{5.6}$$

For the remainder of this chapter, we will focus on the implementation of the PLLs, rather than on a detailed phase error analysis. Therefore the relevant aspect for the following discussion is simply to understand the basic building blocks of a PLL. In the next chapter, however, a detailed noise analysis based on this theory will be presented.

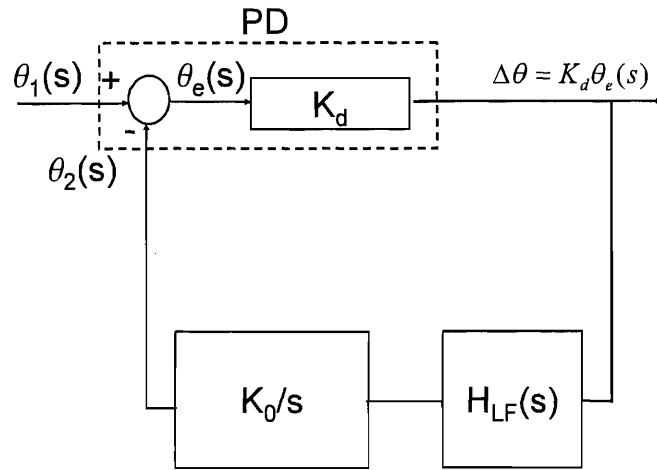
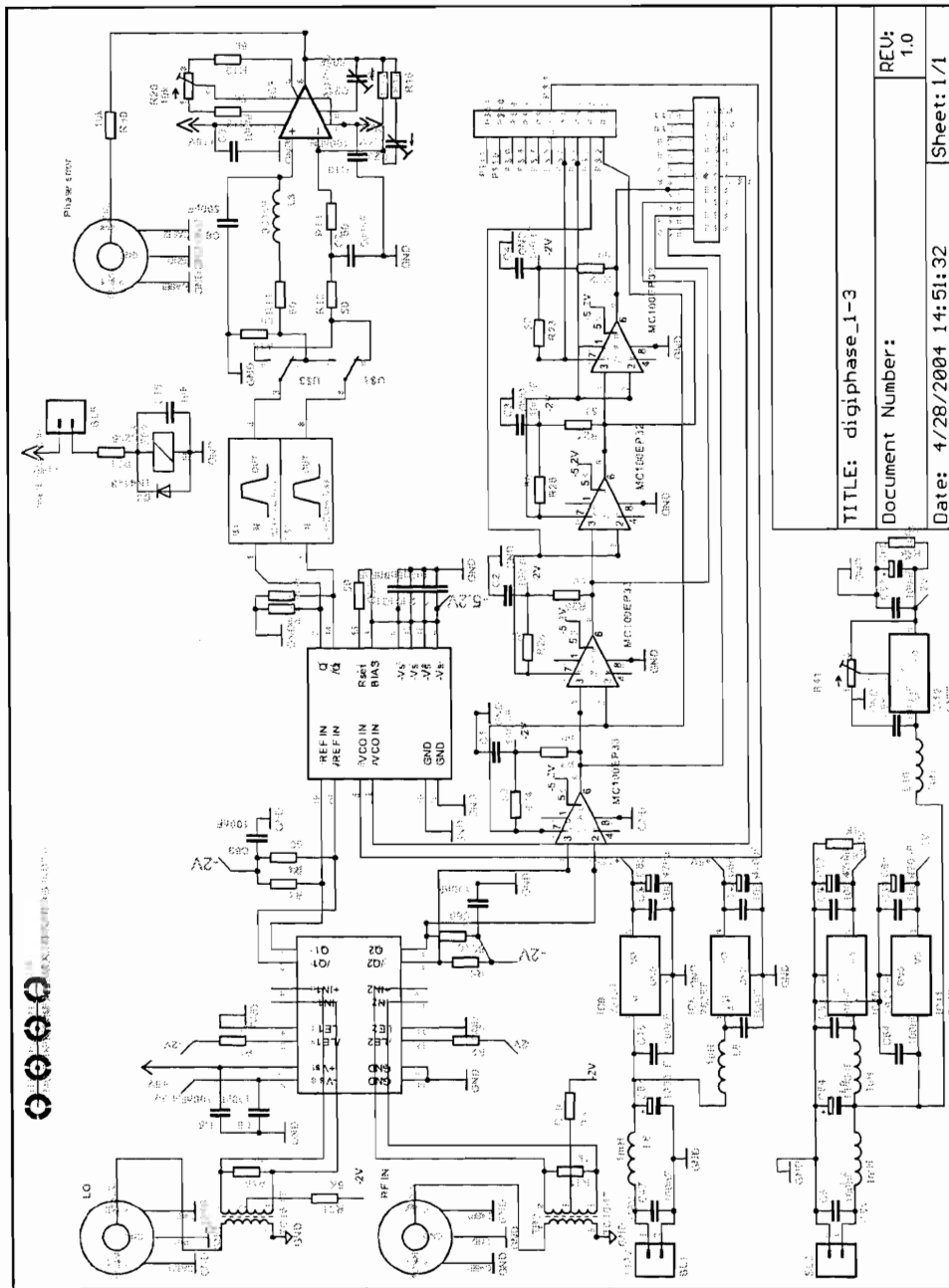


Figure 5-2: Linear model of the PLL. All symbols described in text.

5.2 Digital phase detection

The two most common methods of implementing phase detectors are (1) analog mixers and (2) a number of sequential logic circuits which together function as a digital phase detector. Our approach has been to use digital phase detection for the frequency comb stabilization. A digital phase detector offers the advantage of also serving as a frequency discriminator, which facilitates locking when the frequencies involved drift significantly. The first design of the digital phase detector board was done in collaboration with Thomas Schibli after a visit to the laboratory of John Hall and Jun Ye at JILA. Since then, it has been modified to better fit our experimental needs. A schematic of the circuit is shown in Fig. 5-3. The three key components in this design are an ultrafast comparator (AD96687), a digital phase detector/frequency discriminator (AD9901) and digital divider chips (MC100EP33 and MC100EP32).



TITLE: digiphase_1-3

Document Number:

Date: 4/28/2004 14:51:32

REV: 1.0

Sheet: 1/1

Figure 5-3: Schematics of digital phase detector board. Design by Lia Matos adapted from design by Thomas Schibli, itself adapted from JILA design.

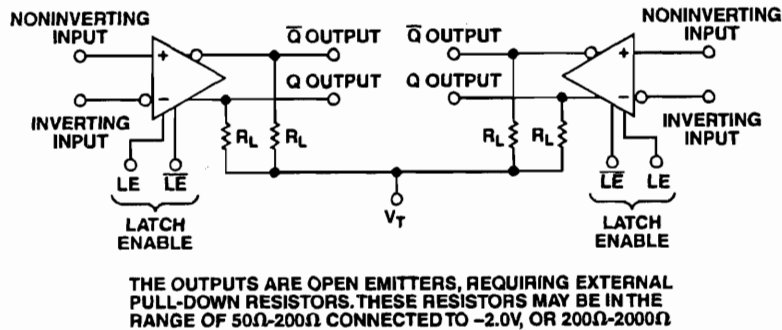


Figure 5-4: Schematics of ultrafast comparator AD96687 chip. The LO and RF signal are AC coupled to the inverting and noninverting inputs of the chips, and the Q and \bar{Q} ECL compatible outputs are generated.

5.2.1 Ultrafast comparator

The incoming signals from the local oscillator (LO) and the heterodyne detection (RF) are analog sine waves and in order to be recognized by the digital phase detector, they first need to be digitized. For this purpose the AD96687 ultrafast comparator is used, which contains two voltage comparators. The signals are AC coupled to both the inverting and noninverting inputs of the chip, and a positive voltage swing leads to a logic high while a negative voltage swing leads to a logic low. The schematic of the chip is shown in Fig. 5-4. The chip provides an ECL compatible output, which stands for Emitter Coupled Logic. ECL signals are often used for high speed applications, due to the differential nature of the design (typical response times are of a few nanoseconds). A differential signal is taken between the inverting and noninverting inputs, causing the average current of both signal paths to be always zero. ECL signals must always be terminated by a proper load to avoid reflections. In the schematics in Fig. 5-3 it can be seen that the signal is referenced to -2V via a 50 Ω resistor at the inputs and outputs of the logic chips.

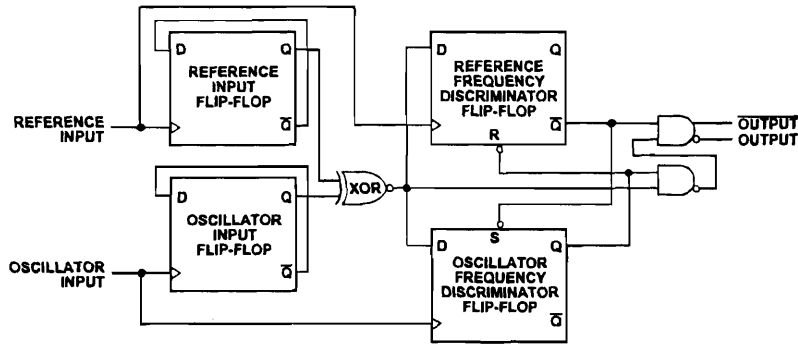


Figure 5-5: Functional block diagram of AD9901.

5.2.2 The AD9901 phase/frequency discriminator chip

The functional block diagram of the AD9901 is shown in Fig. 5-5. The main components are 4 flip-flops, an exclusive-OR gate and some combinational output logic. When the RF and LO signals are very close in frequency, only the phase detection circuit is active. "Very close" means that the PLL system can correct for a phase error of π within its response time. Specific details will be given later. If the RF frequency is substantially far away from the LO frequency, the frequency discriminator circuitry overrides the phase detection circuitry to drive the RF frequency close to the LO frequency and put it within the operating range of the phase detector. This operation is illustrated in Fig. 5-6.

As indicated in the waveforms in Fig. 5-6, the first pair of flip-flops generates a signal with 50% duty cycle, regardless of the duty cycle of the input waves, which can then be used to derive the phase information using the $\overline{\text{XOR}}$ gate. The average value of the $\overline{\text{XOR}}$ output, or the duty cycle of this wave, is proportional to the phase difference between the input signals. This represents the phase detection part of the circuit, which is represented in the sequence of waveforms in the left of Fig. 5-6. In this case, the second pair of flip-flops provide constant high levels to gate the $\overline{\text{XOR}}$ output to the final output.

The frequency discriminator portion of the circuit takes over whenever either the LO

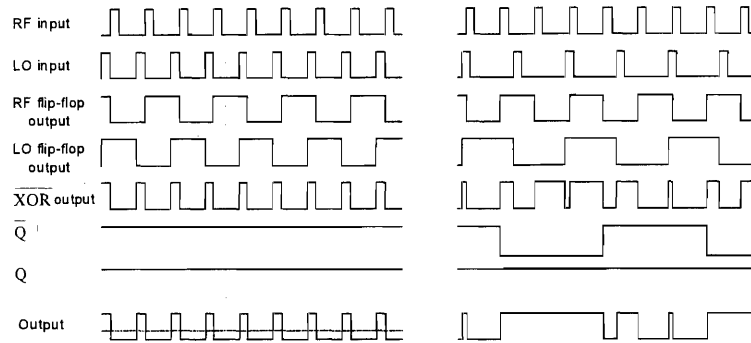


Figure 5-6: Sequence of waveforms describing the functionality of the AD9901. On the left, the two input signals are at the same frequency, and the AD9901 works as a phase detector. On the right, the input signals are at different frequencies and the AD9901 works as a frequency discriminator. The sequence of signals represent the signal flow from left to right in the schematic on Fig. 5-5.

or the RF oscillator input occurs twice before the other. This drives one of the second pair of flip-flops to logic low, which overrides the $\overline{\text{XOR}}$ output and holds the output at the appropriate level to pull the RF signal back towards the LO frequency. Once the frequencies are within less than 2π of each other, the phase detector takes over again. The sequence of waveforms describing the frequency discriminator portion of the circuit is shown on the right of Fig. 5-6.

In the phase detector stage of the AD9901, it has to be noted that the middle of the linear locking range is not at zero volts, but at the midpoint between logic low and high. Since this phase error signal will eventually go into a proportional-integral (PI) controller, we need to have the lock point be at zero volts. To achieve this, we employ a differential amplifier which amplifies the difference between the low-pass filtered DC portion of the inverted and non-inverted outputs of the AD9901. The output of the differential amplifier is at exactly zero volts when the phase difference is π . The differential amplifier can be seen in Fig. 5-3 after the low-pass filters used for averaging the phase detector output.

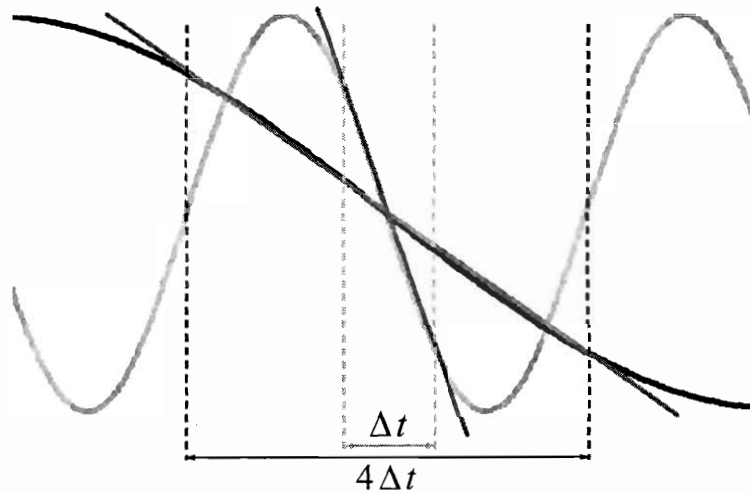


Figure 5-7: Representation of the effect of the divider stage on the linear locking range of the AD9901. For a clear picture, an analog signal is used. The black curve has one quarter of the frequency of the grey curve. The locking range becomes 4 times larger. Since the slope becomes less steep, the resulting lock will not be as tight, but cycle slips are avoided.

5.2.3 Digital divider chips

An important modification to the original design of the DPD board was the introduction of the digital dividers. The purpose of the divider stages is to allow for an increase in the linear phase detection range of the AD9901, thus facilitating the lock. The idea is illustrated in Fig. 5-7. When we consider any lock which is performed in the optical domain by beating a comb line with a cw laser, the jitter caused by the magnified fundamental repetition rate noise will cause the beatnote to drift by tens of MHz in 1 s, barely keeping it within the range of the band-pass filter. In order to catch such a lock, a very fast transducer is necessary. Even with the implementation of the dividers, a piezo actuator with a response of ≈ 100 kHz was necessary to catch the lock of the optical beatnotes which will be described in the next sections. In the design, several division ratios are possible: 4, 16, 32, 64 and 128.

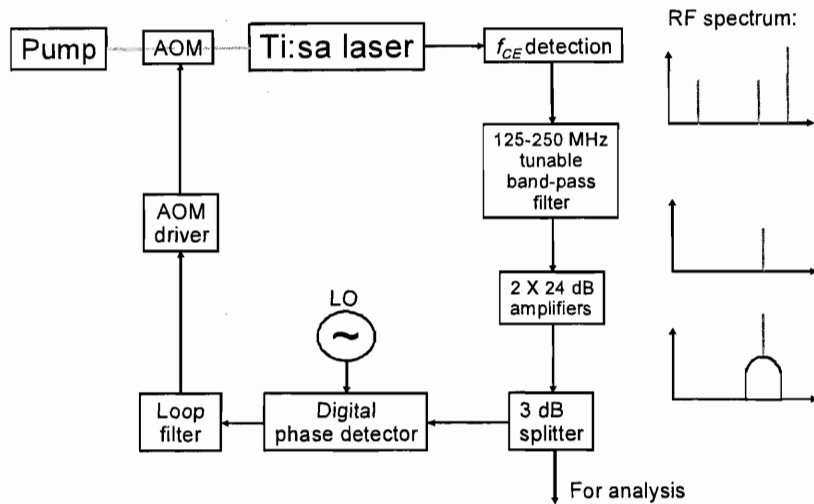


Figure 5-8: Schematic of f_{CE} phase lock setup. A bandpass filter is used to select either f_{CE} or $f_R - f_{CE}$, whichever falls within the range of the band-pass filter. This signal is amplified, split, divided by 4 in frequency to enhance the locking range of the PLL, and compared with a reference frequency supplied by a signal generator (LO) using a digital phase detector. The output signal is amplified in the loop filter, which is a proportional-integral (PI) controller, and fed back to the AOM, closing the loop.

5.3 Carrier-envelope frequency control

Active control of the carrier-envelope (CE) frequency, f_{CE} , of mode-locked lasers is a prerequisite for both time and frequency domain applications. For our octave-spanning lasers which do not use intracavity prisms for dispersion compensation [29],[55] this control can be achieved by utilizing the response of f_{CE} to intracavity power, i.e., by controlling the intracavity pulse energy via modulation of the pump power [57],[58]. Details of the f_{CE} detection setup were described in the previous chapter. Here, we give an overview of its electronic implementation.

A schematic of the stabilization setup is shown in Fig. 5-8. To implement the lock, we filter either the f_{CE} or the $f_R - f_{CE}$ component, whichever lies within the frequency range of the band-pass filter (125 to 200 MHz), from the PMT signal. After amplification of the signal to reach the minimum power level required by the DPD board (-3 dBm), it

is split and half the power is sent to the input of the DPD which generates an error signal relative to an RF synthesizer, used as the local oscillator (LO) in the lock. In general, the linear phase detection range is increased to 4π (by the digital divider) before the phase detector, although the beat is stable enough for locking without any pre-division. The phase error signal is then sent through a proportional-integral (PI) controller that properly filters and amplifies the signal fed to the acousto-optic modulator (AOM), which modulates the pump power, changing the carrier-envelope frequency in such a way as to cancel the phase error.

The loop filter was designed to provide flexibility to match the necessary frequency response of any laser stabilization setup in the laboratory. It has the capability of providing a signal with any voltage range and offset between -15 V and 15 V. It is used in all of the locks described here. A detailed schematic of the circuit is shown in Fig. 5-9. The possible gain settings are 1, 2, 10, 40 and 100. The possible integrator corner frequencies are 0 Hz, 10 Hz, 100 Hz, 1 kHz and 10 kHz. For the f_{CE} lock, the integrator corner frequency is at 10 kHz, to provide enough gain to cancel out the noise due to intensity fluctuations in the pump laser. The AOM driver takes a modulation input signal in the range of 0 to 1 V, so we operate at a voltage offset around 0.5 V.

When the f_{CE} beat is phase locked, its linewidth is 1 Hz FWHM, limited by the resolution of the RF analyzer. The RF spectrum of the phase-locked beat can be seen in Fig. 5-10 over three different frequency ranges. The output of the phase detector is proportional to the remaining jitter between the carrier-envelope phase evolution and the local oscillator reduced by the division ratio of 4. The power spectral density (PSD) of the f_{CE} phase fluctuations S_ϕ measured with a vector signal analyzer (VSA) at the output of the phase detector and properly re-scaled by the division factor is shown in Fig. 5-11. S_ϕ represents the frequency domain representation of the fluctuations in f_{CE} at Fourier frequencies relative to its carrier. The accumulated (root-mean-square) carrier-envelope

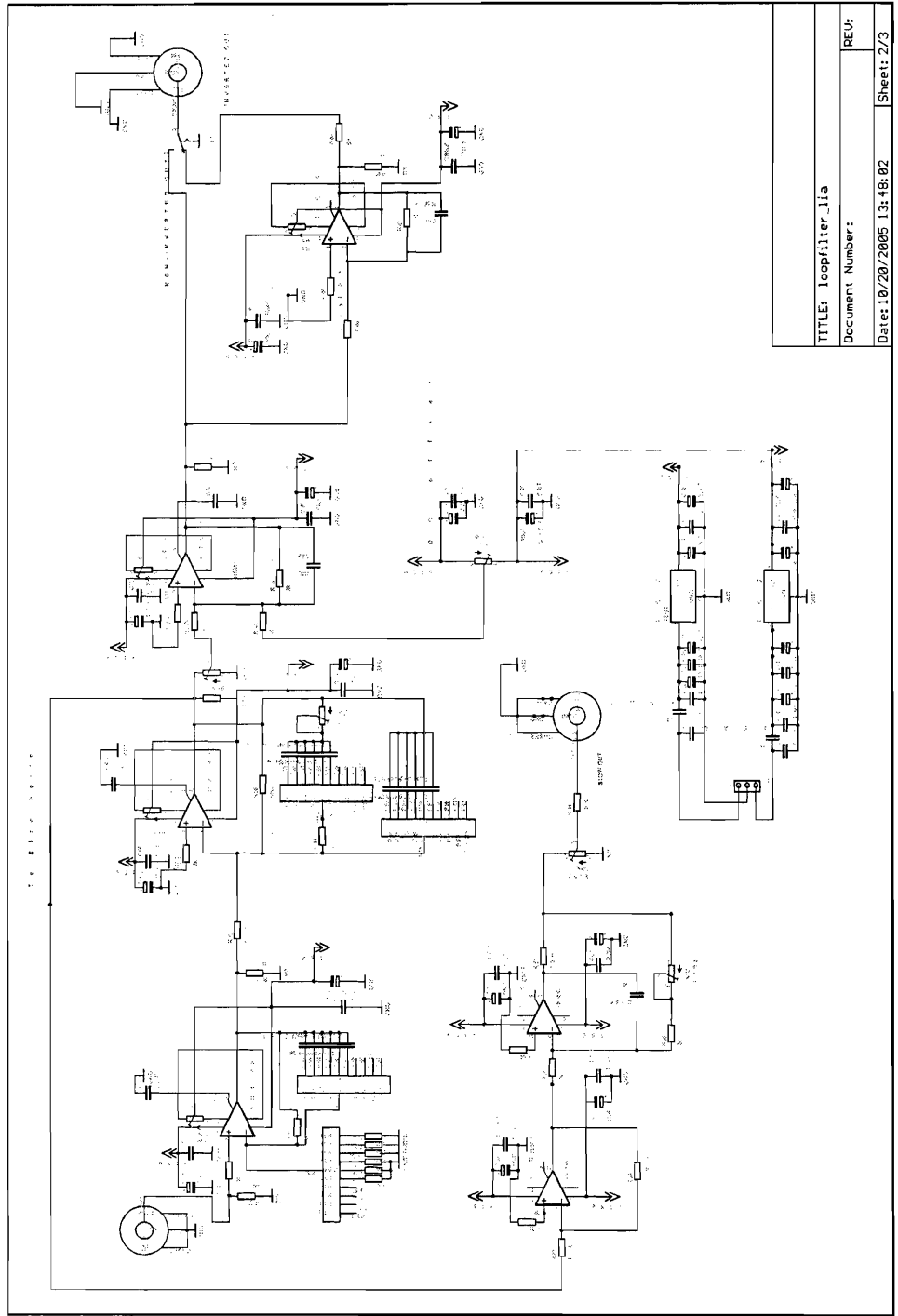


Figure 5-9: Schematic of loop filter designed by Lia Matos and Cort Johnson.

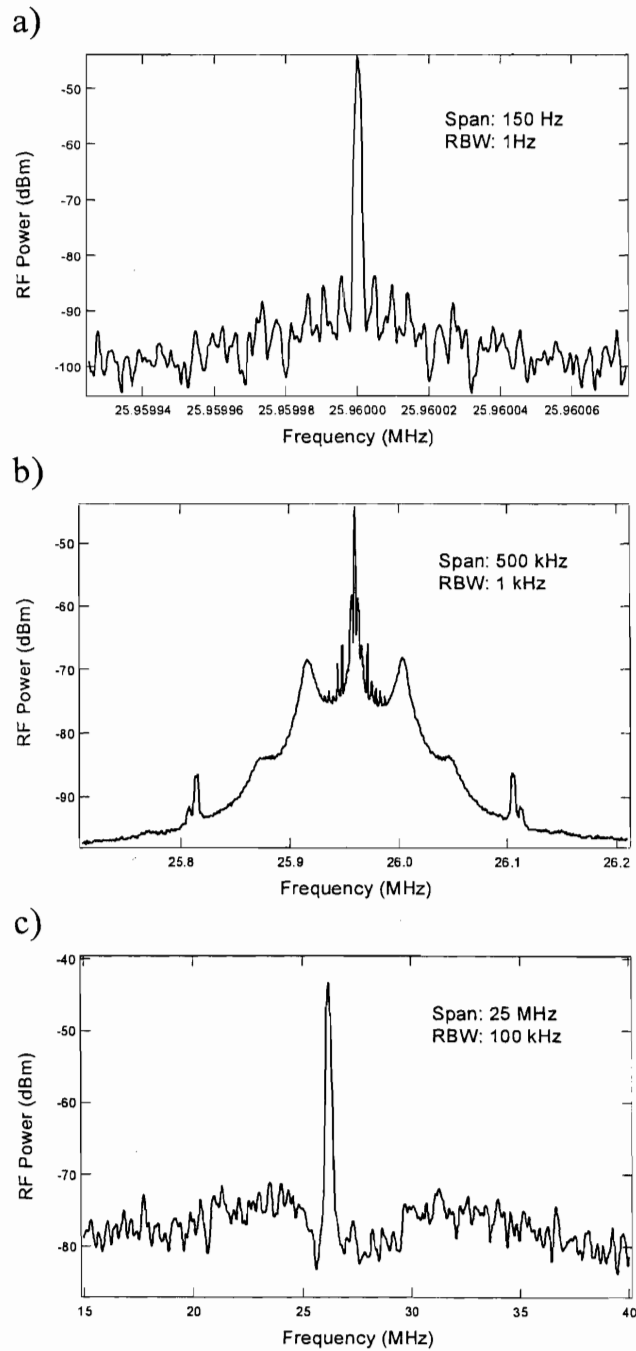


Figure 5-10: Spectrum of phase locked f_{CE} beat, seen over three different frequency ranges. In (a), a FWHM of 1 Hz is measured, limited by the RBW of the device. In (b), we can infer the loop bandwidth, which corresponds to the two spikes on the noise pedestal to the left and right of the signal, ≈ 100 kHz. In (c), we observe a 35 dB S/N in a 100 kHz RBW, which is enough for routine operation.

phase error $\Delta\phi$ can be obtained from S_ϕ by integration over frequency according to [55]

$$\Delta\phi(f) = \Delta\phi = \left[-2 \int_{10 \text{ MHz}}^f S_\phi(f') df' \right]^{1/2}, \quad (5.7)$$

resulting in a value of 0.257 rad (integrated from 2.5 MHz to 10 MHz). This low value reflects the elaborate acoustic vibration isolation and shielding against environmental perturbations (e.g., air currents) as well as the effectiveness of the PI control loop up to ~ 80 kHz. As will become clear in the discussion in the next chapter, at present this limitation is due to two main factors: first, the AOM imposes a phase delay which contributes to a decrease in the phase margin that reduces the closed loop bandwidth. Second, the gain dynamics in the laser also plays an important role in the overall noise performance, since a change in pump power does not translate to an instantaneous change in the pulse energy and therefore in f_{CE} . In chapter 6, a detailed noise analysis of the f_{CE} stabilization and its connection with the theory of mode-locking will be presented.

In the expression for the RMS phase error $\Delta\phi$, Eq. 5.7, f represents the inverse observation time of the measurement while f' represents the frequency relative to the carrier. The factor of two in this equation occurs because S_ϕ is symmetric and the integration is only done over the upper noise sideband. In general, the coherence time of an optical frequency is taken to be the observation time up to which the integration of S_ϕ yields a phase error of 1 radian [59]. In our case, the lower limit of the measurement is 2.5 MHz, indicating a coherence time of at least 400 s. The measurement was limited by the capabilities of the VSA. It is important to note, however, that this measurement was performed in-loop. In general, an out-of-loop measurement will present increased phase error due to the fact that the limited loop bandwidth will attenuate any noise at a frequency higher than this bandwidth, thus yielding a phase error which does not represent the real value. In our case, the digital phase detector output is averaged by using a 1.9 MHz low-pass filter, thus any noise at a frequency higher than this will not be observed in the measurement. However, measurements performed in a similar system [55]

seem to indicate that the difference between in-loop and out-of-loop is not very significant (about 10%). This difference is more critical in frequency combs that employ external fiber broadening, where, if care is not taken, intensity noise on the light translates into phase noise due to the high nonlinearities in the fiber. This phase noise will then be cancelled in the laser, which is not the original noise source and the net effect will be to add phase noise to the light directly out of the laser. For our frequency combs, it is believed that there are no significant f_{CE} noise sources external to the laser, due to the monolithic nature of the f_{CE} detection setup (see Fig. 4-6 b) and to the absence of the broadening fiber.

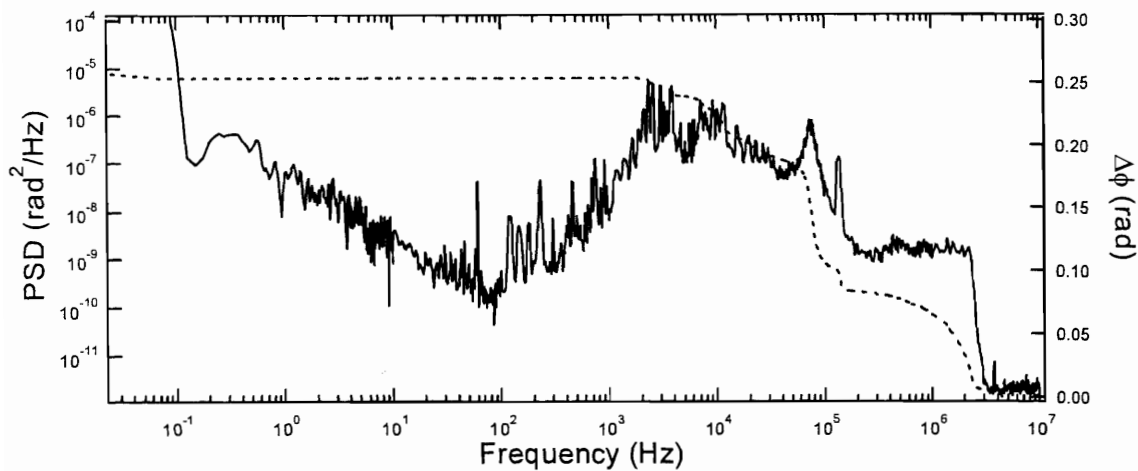


Figure 5-11: Power spectral density (PSD) of the carrier-envelope phase fluctuations S_ϕ (black curve) and integrated phase error $\Delta\phi$ (dashed curve), measured with a vector signal analyser (VSA) at the output of the digital phase detector.

5.4 Repetition rate control: lock to 1S-2S spectroscopy laser

An important motivation for developing the system described here is to apply new frequency comb technology to innovative methods for ultraprecise spectroscopy with ultra-

cold hydrogen, with the goal of creating an optical clock based on the 1S-2S two-photon transition. In all of the experiments for which this frequency comb is intended, it is required that the comb lines be referenced to the hydrogen 1S-2S transition. Since the f_{CE} frequency control is implemented by self-referencing, this is achieved by referencing and locking the laser repetition rate, f_R , to the 1S-2S transition. In practice, this lock is realized in the optical domain by locking a comb line (or the 4 millionth harmonic of f_R) to the 1S-2S transition via a cw dye laser operating at 486 nm. The details of the intended applications to frequency measurements in ultracold hydrogen will be discussed in chapter 7. A schematic of the fully stabilized comb can be seen in Fig. 5-12. A heterodyne beat signal is generated between the second harmonic of a comb line and the dye laser, which performs 1S-2S spectroscopy of ultracold hydrogen [60]. This beat signal is stabilized by controlling the cavity length with two PZT-mounted cavity mirrors.

5.4.1 Heterodyne beat detection setup

The details of the optical heterodyne detection setup is shown in Fig. 5-16. A second output coupler external to the laser cavity spectrally separates the beam into two portions, the transmitted beam contains the low and high wavelengths (what we call the "wings" of the spectrum) used in the $f - 2f - f_{CE}$ detection setup, and the reflected beam contains all of the remaining spectrum (that which lies within the bandwidth of the output coupler seen in Fig. 3-8). The mirror needs to be placed at close to normal incidence for this to work, since the center of the transmission curve will shift as the mirror is placed off normal incidence.

The reflected portion of the external output coupler is focussed into a 1 cm length potassium niobate crystal (KNbO_3), which is non-critically phase matched (NCPM) at -19°C for sum frequency generation of 972 nm. Because the beat signal occurs between one single comb line and the dye laser, it is important to convert the sum frequency of as many comb lines as possible at 972 nm to one single comb line at 486 nm, as the diagram of Fig.5-13 shows. When choosing the crystal length, there is an interplay between

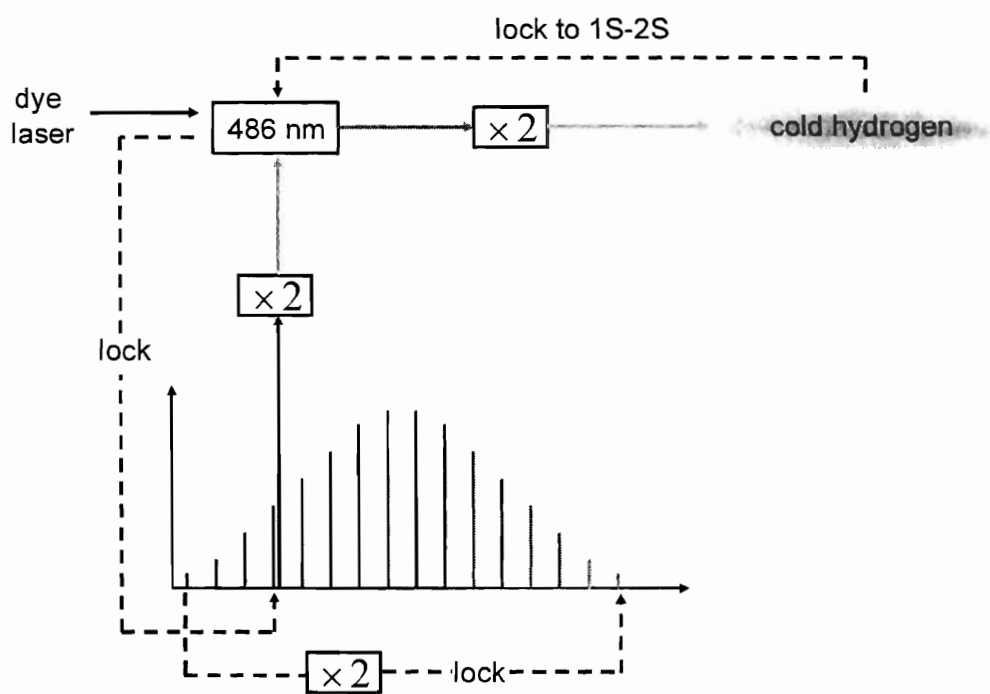


Figure 5-12: Representation of fully stabilized frequency comb, referenced to the 1S-2S transition in ultracold hydrogen.

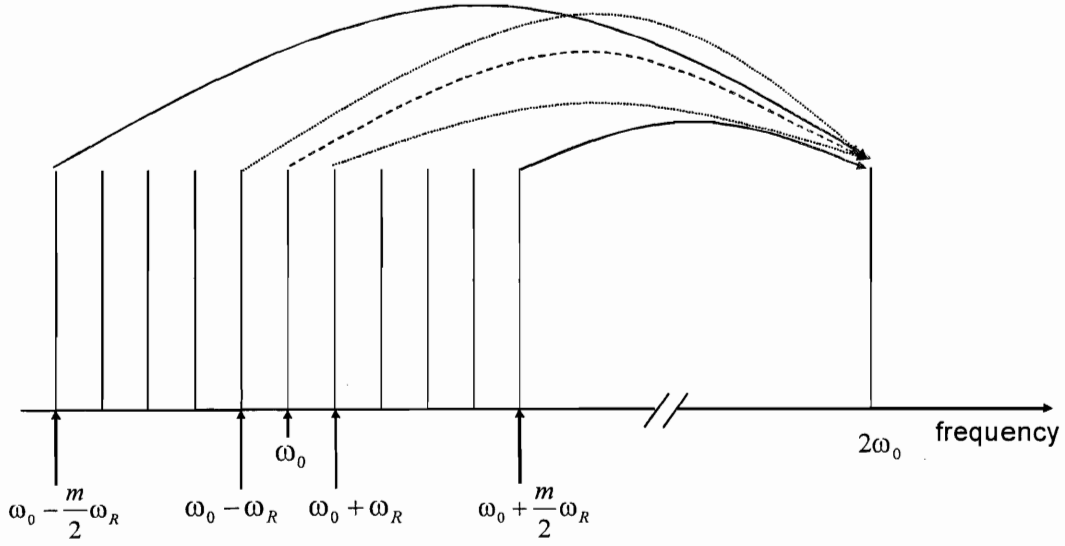


Figure 5-13: Schematic representation of sum-frequency generation of comb light for locking to 1S-2S spectroscopy laser. The process is phase-matched for sum-frequency into a single mode at 486 nm as the diagram shows.

the total amount of nonlinearity that enhances the frequency converted field, which increases with the crystal length, and the bandwidth of the SFG process, which decreases with length due to group velocity dispersion and to a limited phase-matching bandwidth, thus causing less fundamental comb modes to contribute to the sum frequency generation (SFG) process. Because this process is noncritically phase matched and potassium niobate is a uniaxial crystal, it is simple to calculate the optimum crystal length by calculating the total power converted into one comb line at 486 nm as a function of the crystal length l .

The first step in the derivation is to write the evolution of the frequency converted field [61]

$$\frac{\partial E_2(\omega, z)}{\partial z} = -i \frac{\omega_0 d_{eff}}{nc_0} \int_{-\infty}^{+\infty} E(\omega - \omega_1) E(\omega_1) e^{-i[k(\omega) + k(\omega - \omega_1) - k(\omega_1)]z} d\omega_1 \quad (5.8)$$

We convert the above integral to a discrete sum over all comb modes contributing to the SFG process, where we have the following relationship between the angular frequencies

$$\begin{aligned}\omega - \omega_1 &= \omega_0 + n'\omega_R \\ \omega_1 &= \omega_0 - n'\omega_R\end{aligned}\tag{5.9}$$

such that $\omega = (\omega - \omega_1) + \omega_1 = 2\omega_0$ and all modes sum up to the same final optical frequency. n' indicates the index of the comb mode participating in the SFG process. Expanding $k(\omega - \omega_1)$, $k(\omega_1)$ and $k(\omega)$ up to second order and after a little algebra, we obtain that for $\omega = 2\omega_0$ the total power converted to a single comb line at 486 nm due to the sum frequency generation process is

$$P_{486} = \frac{2\omega_0^2 d_{eff}^2}{\epsilon_0 n^3 c^3} \frac{P_i^2}{A_{eff}} l^2 F^2\tag{5.10}$$

where

$$F = \sum_{n'=0}^m e^{-i(l\Delta k' n'^2/2)} \frac{\sin(l\Delta k' n'^2/2)}{l\Delta k' n'^2/2}\tag{5.11}$$

is a convolution of the fundamental pulse with itself. In Eq. 5.10, $\omega_0 = 2\pi c/\lambda$, where $\lambda = 972$ nm, $d_{eff} = 8 \times 10^{-12}$ m/V, $n = 2.2$, $P_i = 100$ nW is the fundamental optical power in one comb line, $A_{eff} = \frac{\pi}{2} w_0^2$ is the effective area for the Gaussian beam and w_0 is determined by the confocal parameter $b = l = 2\pi w_0^2/\lambda$. In Eq. 5.11, $\Delta k' = \frac{1}{2} D_2 \omega_R^2$, $\omega_R = 191$ MHz/ 2π is the comb spacing in rad/s. As shown in Fig. 5-13, we consider the simplified case of a square spectrum, where $m = 50,000$ is the number of modes corresponding to a pulse of 100 fs. We estimated this to be the incident pulse width on the crystal due to pulse stretching caused by the dispersion of the optical elements before the crystal (focussing lens, window for crystal enclosure and external output coupler). Fig. 5-14 shows the converted power as a function of crystal length. We see that making the crystal longer than 0.8 cm does not help the conversion efficiency. The result is a 75% conversion efficiency into the desired mode. This high value is made

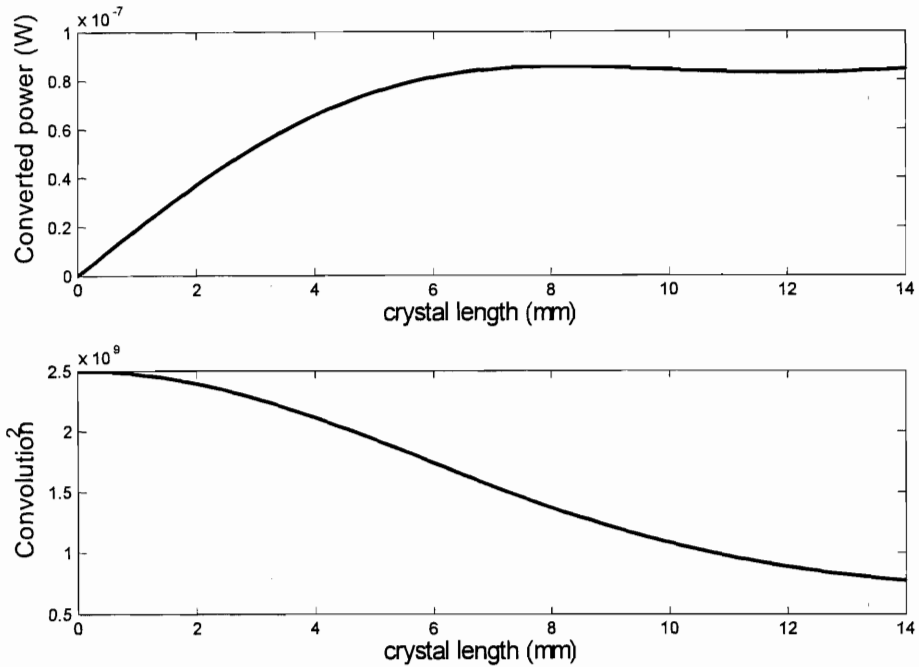


Figure 5-14: Above: conversion efficiency as a function of crystal length for 191 MHz laser. Below: corresponding value of F^2 .

possible only by the broadband nature of the SFG process.

The importance of mode preselection for obtaining low noise beat signals between a comb line and the cw laser has been pointed out by Reichert *et.al* [6]. Because the beat signal is detected between the cw laser and a comb line in the presence of a large number of other comb lines which only contribute to noise, the best effort to eliminate as many unwanted comb lines as possible should be employed. Typically, when beating a cw laser with the fundamental frequency comb, mode preselection is achieved with the help of a grating. In the case described here, however, the SFG process in itself provides optimum filtering of unwanted comb lines, because of its single-frequency mode-matching characteristics. After the KNbO_3 crystal, we split the fundamental comb spectrum (horizontally polarized) from the frequency converted portion (vertically polarized) using a polarizing beam splitter (PBS 1). We observe the converted spectrum in an optical spec-

trum analyzer and measure 0.2 nm FWHM of optical bandwidth, with a total average power of 50 μ W. This corresponds to 665 lines, each with an average optical power of 75 nW, close to our prediction of 82 nW.

In the schematics in Fig. 5-16, the dye laser light, with horizontal polarization, is combined with the frequency converted comb light, with vertical polarization, by means of a second PBS (PBS 2). A half wave plate (wave plate 2 in the schematic) then projects variable amounts of light from each beam on to the vertical polarization which interfere at the avalanche photo detector (APD). Full control of the relative intensity of the matched beams, as well as the initial amount of dye laser power, can be achieved by adjusting wave plates 1 and 2. It has been shown that the S/N can be expressed under such conditions as [6]

$$S/N \approx \frac{\eta}{h\nu B_w} \frac{tP_n(1-t)P_{cw}}{NtP_n + (1-t)P_{cw}} \quad (5.12)$$

where η is the quantum efficiency of the detector, B_w is the detection bandwidth (RBW), $h\nu$ is the energy of a single photon, P_n is the optical power in a single comb line, P_{cw} is the power in the cw laser beam and t is the transmission of the variable beam splitter used to match the two beams (here, wave plate 2). It should be noted that in this expression our initial assumption of a square spectrum must still hold, with equal power in each of the comb lines. Additionally, if we assume that t is always adjusted to obtain the optimal S/N, $t_{opt} = \sqrt{P_{cw}}/(\sqrt{NP_n} + \sqrt{P_{cw}})$ we see that for $N \ll P_{cw}/P_n$, the only limitation in the detection is the shot noise of the weak signal:

$$S/N_{opt} = \frac{\eta P_n}{h\nu B_w}. \quad (5.13)$$

As a rule-of-thumb, the mode preselection process must remove enough comb lines such that the sum of the power of all the remaining lines is much smaller than the power in the cw laser. In our case, the average power of the frequency converted light is 50 μ W and the power from the dye laser is typically on the order of 5 mW, a factor of 100 larger. The S/N obtained is typically around 40 dB in 100 kHz RBW, which is smaller than

the prediction of 54 dB from Eq. 5.13. This is most likely due to poor spacial overlap between the two beams. Even though a telescope is employed after the optical fiber that brings the light from the dye laser, the spatial mode of the comb is not a perfect TEM_{00} mode, and the power which is contributing to the beat is smaller than the full measured power. One possible solution would be to assure perfect overlap by sending both beams through the same optical fiber (there would be a significant power loss in this process, but most likely it would not offset the advantages gained from a perfect spatial overlap). This was not implemented since 40 dB S/N is already enough for routine phase-locking.

5.4.2 Stabilization electronics

The part of the experimental setup between the detection of the heterodyne beat up to the input of the DPD is identical to the carrier-envelope phase lock already described in Sec. 5.3. This beat signal, however, is significantly less stable than the f_{CE} beat. While the latter would take a full day to drift across the bandwidth of the band-pass filter (≈ 8 MHz), the first will do so in a matter of seconds. This makes obtaining this lock significantly more challenging, since a transducer with a fast enough response time to catch it is necessary. When we consider that the mechanism used to control f_R is to change the cavity length via piezoelectric actuators (PZTs), an immediate limitation comes from the mechanical resonances of PZT-mounted mirrors, which are typically in the few kHz range if conventional sized mirrors and optical mounts are used.

To overcome this limitation, a PZT-mounted mirror with as high a mechanical resonance as possible should be employed. Our design is shown in Fig. 5-15(a). While all the cavity mirrors have a 0.5" diameter and 0.5" thickness, the PZT-mounted mirror has .25" diameter and is only 1 mm thick. We mount it on a PZT with a natural resonance frequency of 300 kHz, which is then glued to a very massive mount, machined from copper and filled with lead. This allows it to act as an "infinite mass", or a fixed boundary for the PZT. The resonance frequency is then determined by the combined mass of the PZT itself and the mirror. A Michelson interferometer with the PZT-mounted mirror on

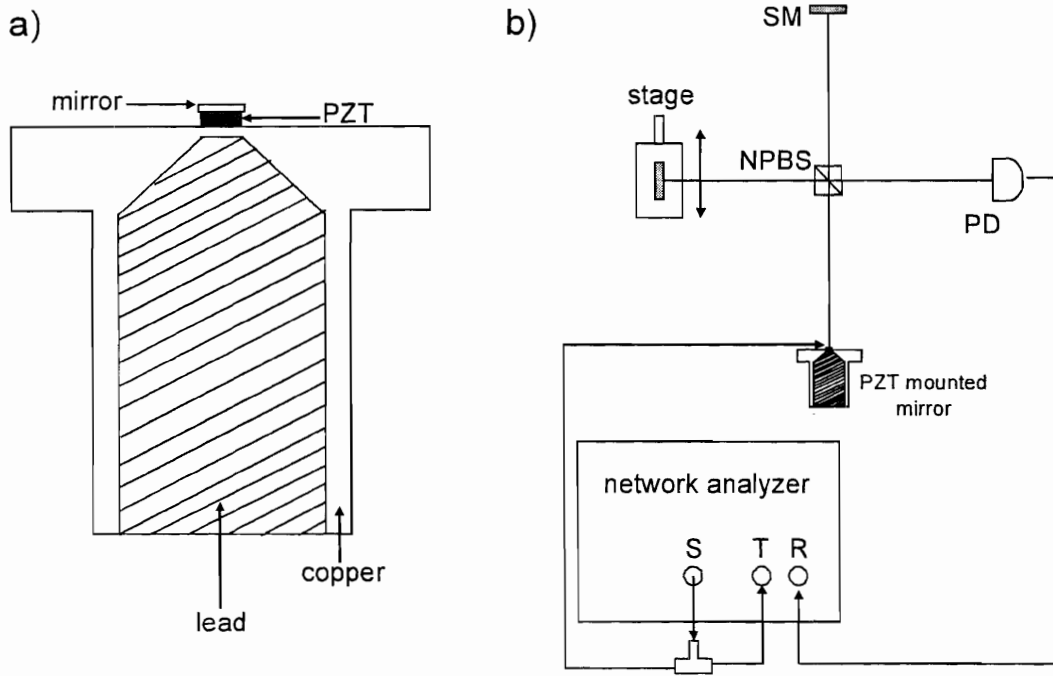


Figure 5-15: (a) Drawing of fast PZT-mounted mirror. The copper portion of the mount was machined and filled with molten lead. (b) Schematic of Michelson interferometer built to measure the mechanical resonance frequency of the PZT-mounted mirror. The source of the network analyzer is split into two portions, half of which goes to the R input and the other half which is used to drive the PZT. The response is then measured by feeding the modulated intensity signal from the photo detector (PD) to the T input of the network analyzer, which then measures the amplitude and phase of T/R as a function of the source frequency.

one of the arms was built to measure the resonance of the PZT. The setup is shown in Fig. 5-15(b). By setting the interferometer arm lengths to the region of highest contrast, a modulation voltage drive to the PZT will cause a corresponding modulation of the intensity of the light on the photo-detector, as the interferometer moves back and forth from a dark to a bright fringe. By driving the PZT with the source signal from a network analyzer, we could measure the frequency response of the PZT. The measurements showed that the lowest mechanical resonance was at 120 kHz.

With the fast PZT in the cavity, we are able to catch the lock by increasing the linear phase detection range to 32π . The fast PZT has a fast response but a small dynamic range of 11 nm/V. It is driven by a low-voltage driver, which can provide at most 15 V, allowing it a maximum travel range of 165 nm. Therefore, it cannot maintain the lock for a very long time because the lab temperature drifts significantly over the course of the day, causing fluctuations of the cavity length. A slow PZT with a large dynamic range is then necessary to keep the lock in place. Once the fast PZT catches the lock, we slowly increase the gain of the slow portion of the loop filter signal which is fed to the slow PZT. Our slow PZT has a travel range of 15 $\mu\text{m}/\text{kV}$ and a resonance frequency, also measured with a Michelson interferometer, of 630 Hz. With this arrangement, the lock can be maintained for several hours.

5.5 A note on passive stabilization

So far we have discussed the techniques used to actively stabilize the frequency comb. All the locks are made significantly less challenging if good passive stabilization is assured to begin with. This short section is aimed at describing our approach to passively stabilizing the system.

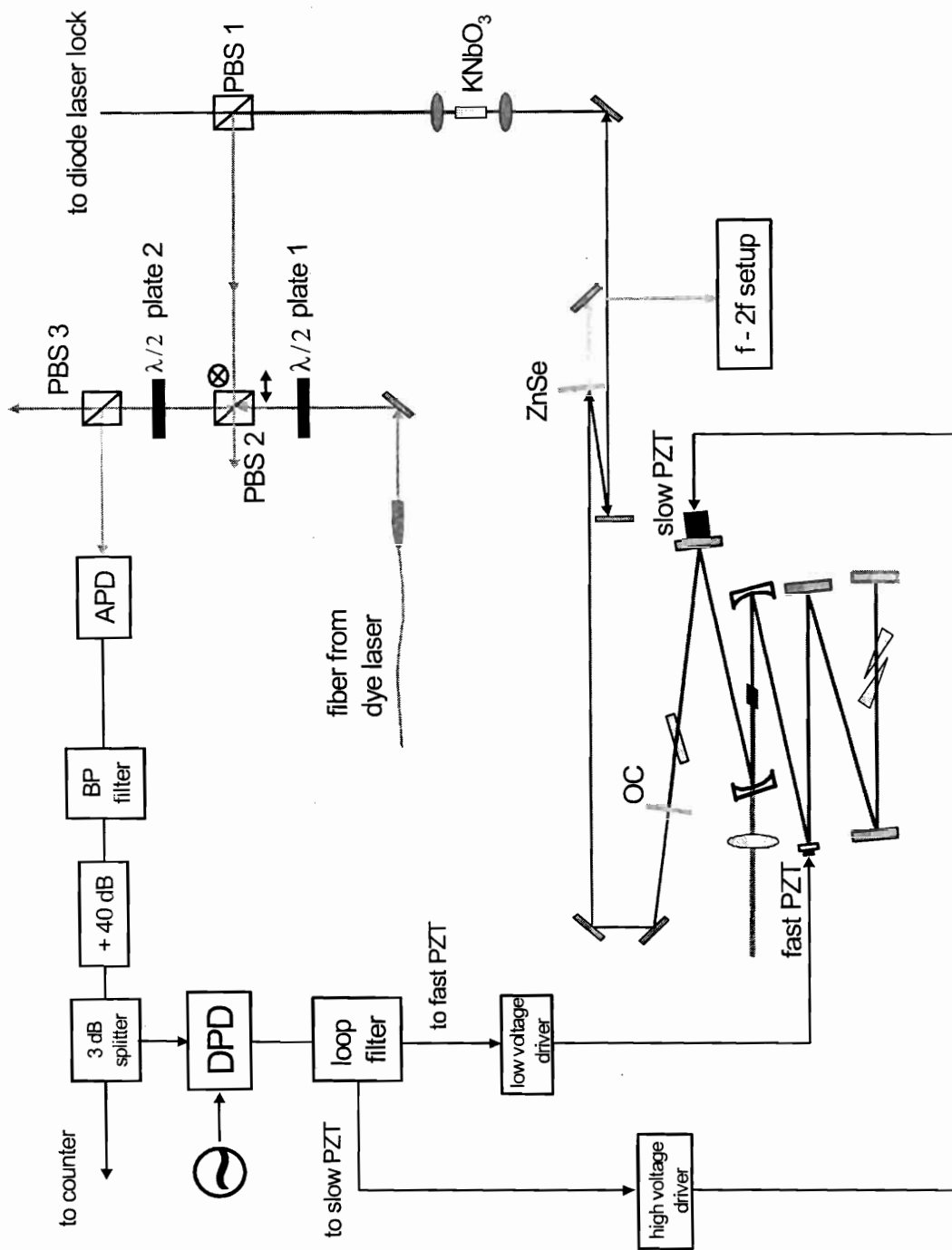


Figure 5-16: Experimental setup for lock to dye laser. A ZnSe mirror reflects the central portion of the spectrum, which is sent through the KNbO_3 crystal for sum frequency generation of 486 nm light, which is separated from the fundamental using a polarizing beam splitter (PBS1). Variable portions of this comb light and the dye laser light are combined and interfere on the surface of the avalanche photo-detector (Menlo Systems APD210). The generated beat signal is then filtered and amplified and sent to the digital phase detector which generates an error signal relative to the local oscillator. The error signal is amplified and filtered in the loop filter, and a fast portion sent to the fast PZT, which is responsible for acquiring the lock, while a slow portion is sent to the slow PZT, responsible for maintaining it over long term (a few hours).

5.5.1 Vibration isolation

To decouple the laser from the building mechanical vibrations, the whole system (laser + optical heterodyne detection setups) is built on a vibrationally isolated breadboard, by means of several layers of material of different mechanical impedances. First, a layer of hard rubber, suited for damping mechanical noise, is used. On top of that we place a multi-layer lead-foam pad (three layers of foam and two layers of lead). The last layer, between the breadboard and the lead-foam, is a double layer of 2 mm lead sheet. This provides sufficient vibration isolation, since strong tapping on the laser table does not disturb either of the locks.

The other important environmental perturbation which leads to mechanical vibrations of the laser mounts is air flow. Air flow from a fan blower unit in the ceiling significantly disturbs the laser operation. Another source of air flow is the convection caused by heating of the pump laser. To suppress this noise source, a 0.5" thick plexiglass enclosure is built around the laser cavity itself, excluding the pump laser. A heavy metal lid is used to avoid resonances of the enclosure which would transfer to the breadboard and to the air pressure inside the enclosure. A second isolation is used by covering the surroundings of the laser table with plastic curtains

5.5.2 Temperature control

In the first version of the frequency comb setup (80 MHz repetition rate), the entire setup (pump laser, laser cavity and heterodyne detection) was built the same large breadboard. The slow misalignment of the laser due to temperature fluctuations in the lab was quite severe, requiring a full re-alignment of the resonator every few days. To minimize this problem, the new 191 MHz version is built on its isolated breadboard, which was specially machined to be water-cooled. The same chiller which cools the pump laser and the Ti:sapphire crystal is also used to temperature control the breadboard. This has improved the problem but not solved it completely since the pump laser is still on the original breadboard, which is not temperature controlled. A larger breadboard which could fit

the laser with its enclosure and the pump laser external to that would most likely improve the situation even further. Currently, the long term stability of the laser depends strongly on the seasons: in the summer, the temperature and humidity fluctuations in the lab are large, making it harder to run the laser over many days without the need for re-alignment. In the winter the climate conditions improve and with it the long term stability.

Chapter 6

Carrier-envelope phase dynamics and noise analysis

For a significant period of time during this project, the long term stability of the carrier-envelope phase lock would vary appreciably from day to day. The reason for this was not well understood, yet it compromised the usefulness of the frequency comb. This motivated us to investigate the underlying mechanisms that affect the carrier-envelope phase and consequently the carrier-envelope offset frequency in octave-spanning lasers. This study enhanced our understanding of the laser operation from the point of view of the carrier-envelope phase dynamics such that it is now possible to consistently find the correct operating point for the carrier-envelope phase lock. More broadly, if such systems are to be used in the future for optical clock applications, these findings will be essential for their reliable and robust operation.

Another area where a thorough understanding of the underlying mechanisms in the carrier-envelope phase control is important is in time-resolved experiments sensitive to the electric field of the pulse. The study here presented opens up the possibility for ultimately low carrier-envelope phase jitter in few cycle optical pulses.

In this chapter, we investigate the carrier-envelope phase dynamics of octave-spanning Ti:sapphire lasers and perform a complete noise analysis of the carrier-envelope phase

stabilization [62]. We model the effect of the laser dynamics on the residual carrier-envelope phase noise by deriving a transfer function representation of the octave-spanning frequency comb. The modelled phase noise and the experimental results show excellent agreement. This greatly enhances our capability of predicting the dependence of the residual carrier-envelope phase noise on the feedback loop filter, the carrier-envelope frequency control mechanism and the pump laser used.

Detailed studies of the intensity-related f_{CE} dynamics have been performed in Ti:sapphire mode-locked lasers which employ external fiber broadening for the generation of octave-spanning spectra and f_{CE} control [63]. A connection between the dependence of the carrier-envelope frequency, the laser repetition rate and the center frequency of the pulse spectrum on intracavity pulse energy was found. The experiments showed that the carrier-envelope phase control coefficient $C_{fP_p} = \Delta f_{\text{CE}}/\Delta P_p$, where ΔP_p is a change in pump power, could change signs, consistent with the shifting of the spectrum with pump power also changing signs. In order to obtain optimum conditions for f_{CE} control, the dependence of C_{fP_p} on intracavity power and, therefore, on pump power is of prime importance.

In octave-spanning lasers the carrier-envelope phase dynamics is much simpler. This is due to the fact that the center frequency of the pulse has no observable change with pump power, because the pulse spectrum fills up all the available bandwidth and is in fact limited by the bandwidth of the output couplers available. Then a change of the carrier-envelope frequency due to changes of the center frequency of the pulse is absent and the carrier-envelope frequency responds only to changes in the intracavity pulse energy and the concomitant changes in phase and group velocity related to the nonlinear refractive index. This response has a simple linear behavior, provided care is taken to work in a power region where the laser is operating in a unique single pulse regime, i.e., no continuous-wave (cw) component or multiple pulse operation is present.

In this chapter, we present a full characterization of the intensity-related carrier-envelope phase dynamics in octave-spanning frequency combs (OSFCs) and its impact

on carrier-envelope phase control. We begin by describing, in Section 6.1, the observation of the intensity-dependent shift of the carrier-envelope frequency and its connection with mode-locking theory. Then, motivated by our observations of different carrier-envelope phase jitter in two OSFCs pumped by different lasers, we present in Section 6.2 a complete noise analysis of a carrier-envelope phase stabilized system, which shows that the laser dynamics related to pulse energy and gain plays an important role in the overall control loop and needs to be taken into account if ultimately low residual carrier-envelope phase jitter is desired.

In order to include the gain dynamics in the noise analysis, a transfer function representation of the OSFC stabilization is given, which enables a quantitative noise analysis and eventually optimization of the overall system. It is shown that there is a major difference in the laser dynamics of the continuous-wave running laser and that of the mode-locked laser and that this dynamics has impact in the noise analysis. Measurement of the transfer function of the OSFC confirms the global behavior of the theoretical predictions and leads to excellent agreement between the computed and measured carrier-envelope phase dynamics and noise characteristics.

6.1 Carrier-envelope phase dynamics of mode-locked lasers

In this section we summarize the linear and nonlinear effects in the laser cavity that may lead to a carrier-envelope phase shift per round trip $\Delta\phi_{\text{CE}}$ and, therefore, contribute to the carrier-envelope frequency via

$$f_{\text{CE}} = \frac{\Delta\phi_{\text{CE}}}{2\pi T_{\text{R}}}. \quad (6.1)$$

If we assume that the laser operates at carrier frequency f_c , then the complex carrier wave of the pulse is given by

$$e^{i2\pi f_c(t-z/v_p)}, \quad (6.2)$$

where v_p is the phase velocity of the carrier wave in the cavity. In the absence of nonlinearities the phase velocity is simply the ratio between frequency and wave number due to the linear refractive index of the media in the cavity, i.e., $v_p = v_p(f_c) = 2\pi f_c/k(f_c)$. The envelope of a pulse that builds up in the cavity due to the mode-locking process will travel at the group velocity due to the presence of the linear media given by $v_g = v_g(f_c) = 2\pi[dk(f_c)/df_c]^{-1}$. Therefore, after one round trip of the pulse over a distance $2L$, which takes the time $T_R = 2L/v_g$, we obtain from Eq. (6.2) that the linear contribution to the carrier-envelope phase shift caused by the difference between phase and group velocities is

$$\Delta\phi_{\text{CE}} = 2\pi f_c \left(1 - \frac{v_g(f_c)}{v_p(f_c)} \right) T_R \quad (6.3)$$

and for the subsequent carrier-envelope frequency

$$f_{\text{CE}} = f_c \left(1 - \frac{v_g(f_c)}{v_p(f_c)} \right). \quad (6.4)$$

In a dispersive medium, group and phase velocities depend on the carrier frequency. Therefore, if the carrier frequency shifts as a function of the intracavity pulse energy, the linear carrier-envelope frequency becomes energy and pump power dependent as found in Ref.[63].

In a mode-locked laser there are also nonlinear processes at work that may directly lead to an energy-dependend carrier-envelope frequency as has been shown by Haus and Ippen .There are many effects that may contribute to such a shift. Here we re-derive briefly the effects due to the intensity-dependent refractive index as discussed by Haus and Ippen [64] for the case of a laser with strong soliton-like pulse shaping which can be evaluated analytically using soliton perturbation theory. We then argue that the same analysis holds for the general case where steady-state pulse formation is different from

conventional soliton pulse shaping.

We start from the description of a mode-locked laser by a master equation of the form

$$T_R \frac{\partial A}{\partial T} = D_{\text{irrev}} A + i D_2 \frac{\partial^2}{\partial t^2} A - i \delta |A|^2 A, \quad (6.5)$$

where we have already factored out the carrier wave [40]. Here, D_{irrev} is an operator that describes the irreversible dynamics occurring in a mode-locked laser such as gain, loss and saturable absorption. $A \equiv A(T, t)$ is the slowly varying field envelope whose shape is investigated on two time scales: first, the global time T which is coarse grained on the time scale of the round-trip time T_R , and second, the local time t which resolves the resulting pulse shape. $A(T, t)$ is normalized such that $|A(T, t)|^2$ is the instantaneous power and $\int dt |A(T, t)|^2$ the pulse energy at time T . $D_2 = \frac{d^2 k}{df^2} \frac{L}{8\pi^2}$ is the group-velocity dispersion (GVD) parameter for a dispersive medium. The Kerr coefficient is $\delta = (2\pi/\lambda_c)n_2 L/A_{\text{eff}}$, where λ_c is the carrier wavelength, n_2 is the nonlinear index in cm/W, and A_{eff} is the effective mode cross-sectional area in cm. Strictly speaking, as already discussed in chapter 3, Eq. (6.5) only applies to a laser with small changes in pulse shape within one round trip. Obviously this is not the case for few-cycle laser pulses where the pulse formation is governed by dispersion-managed mode locking [46]. Nevertheless we want to understand this propagation equation as an effective equation of motion for the laser, where some of the parameters need to be determined self-consistently [40].

Let us assume that the laser operates in the negative GVD regime, where a conventional soliton-like pulse forms and that it is stabilized by the effective saturable absorber action against the filtering effects. Then the steady-state pulse solution is close to a fundamental soliton, i.e., a symmetric sech-shaped pulse that acquires an energy-dependent nonlinear phase shift per round trip due to the nonlinear refractive index

$$A(T, t) = A_0 \text{sech}(t/\tau) e^{-i\phi_s T/T_R}, \quad (6.6)$$

see Ref. [64]. The nonlinear phase shift per round trip is

$$\phi_s = \frac{1}{2} \delta A_0^2, \quad (6.7)$$

so called the Kerr phase shift. The derivation of this phase shift contains an approximation, as discussed in Sec. 3.2.1, where the nonlinear term in $K(\Omega)$ contains only the center frequency of the pulse ω_c . A more careful treatment of the influence of the Kerr effect on the pulse propagation, especially for few-cycle pulses, needs to take the self-steepening of the pulse into account, i.e., the variation of the index of refraction during an optical cycle, by adding to the master equation the term [65]

$$L_{\text{pert}} = -\frac{\delta}{\omega_c} \frac{\partial}{\partial t} (|A|^2 A). \quad (6.8)$$

This term comes into the NLSE directly by considering the two nonlinear contributions to expansion 3.14. Therefore, it is clear that it is a consequence of the Kerr effect and is not related to soliton propagation. It can be viewed as a perturbation to the master equation (6.5). For pulses with τ much longer than an optical cycle, this self-steepening term is unimportant in pulse shaping, because it is on the order of $1/\omega_c \tau \ll 1$. However, this term is always of importance when the phase shifts acquired by the pulse during propagation are considered. Haus and Ippen found, by using soliton perturbation theory based on the eigensolutions of the unperturbed linearized Schrödinger equation, analytic expressions for the changes in phase and group velocity. Obviously, the nonlinear phase shift per round trip of the soliton adds an additional phase shift to the pulse in each round trip.

If the term in (6.8) is applied to a real and symmetric waveform, it generates an odd waveform. An odd waveform added as a perturbation to the symmetric waveform of the steady-state pulse leads, to first order, to a temporal shift of the steady-state pulse. For a soliton-like steady-state solution this timing shift can be evaluated with soliton perturbation theory, i.e., using the basis functions of the linearized operator, and results

in a timing shift [64],[66].

$$T_{\text{R}} \left. \frac{\partial \Delta t(T)}{\partial T} \right|_{\text{self-steep}} = \Delta \left(\frac{1}{v_{\text{g}}} \right) = \frac{\delta}{\omega_{\text{c}}} A_0^2 = \frac{2\phi_{\text{s}}}{\omega_{\text{c}}}. \quad (6.9)$$

In total, the compound effect of self-phase modulation, self-steepening, and linear dispersion on the pulse results in a carrier-envelope frequency of

$$\begin{aligned} f_{\text{CE}} &= \frac{f_{\text{R}}}{2\pi} \Delta \phi_{\text{CE}} = -f_{\text{R}} \frac{\phi_{\text{s}}}{2\pi} + f_{\text{c}} \frac{\partial}{\partial T} \Delta t(T)_{\text{self-steep}} + f_{\text{c}} \left(1 - \frac{v_{\text{g}}(f_{\text{c}})}{v_{\text{p}}(f_{\text{c}})} \right) \\ &= -\frac{f_{\text{R}}}{4\pi} \delta A_0^2 + 2\frac{f_{\text{R}}}{4\pi} \delta A_0^2 + f_{\text{c}} \left(1 - \frac{v_{\text{g}}(f_{\text{c}})}{v_{\text{p}}(f_{\text{c}})} \right). \end{aligned} \quad (6.10)$$

As the above expression shows, the term arising from the group delay change due to self-steepening is twice as large and of opposite sign compared with the one due to self-phase modulation. In total we obtain

$$f_{\text{CE}} = \frac{f_{\text{R}}}{4\pi} \delta A_0^2 + f_{\text{c}} \left(1 - \frac{v_{\text{g}}(f_{\text{c}})}{v_{\text{p}}(f_{\text{c}})} \right). \quad (6.11)$$

We emphasize that soliton perturbation theory was only used in this derivation for analytical evaluation of timing shifts. If the pulse shaping in the laser is not governed by conventional soliton formation but rather by dispersion-managed soliton dynamics [46] or a saturable absorber, the fundamental physics stays the same. If the steady-state solution has a real and symmetric component, the self-steepening term converts this component via the derivative into a real and odd term, which is to first order a timing shift in the autonomous dynamics of the free running mode-locked laser. Another mechanism that leads to a timing shift is, for example, the action of a slow saturable absorber, which absorbs only the front of the pulse. So care needs to be taken to include all relevant effects when a given laser system is analyzed.

The derivation above shows that the group velocity change due to self-steepening of the pulse leads to a change in sign of the energy-dependent contribution at fixed center wavelength of the pulse. We checked this prediction by observing the carrier-envelope

frequency shift in a 200 MHz repetition rate octave-spanning laser. We identified which of the peaks in the RF spectrum corresponded to the carrier-envelope frequency by inserting BaF₂ material in the laser and observing which peak moved up in frequency (adding dispersion causes v_g/v_p to decrease, thus increasing the magnitude of the second term in Eq. (6.11)). We then varied the pump power and observed that the same peak also moved up in frequency, confirming the prediction by Eq. (6.11).

Fig.6-1(a) shows the carrier-envelope frequency shift as a function of pump power. As Eq. (6.5) predicts, the carrier-envelope frequency shift follows linearly the pump power over the range where the intracavity laser power (or pulse energy) depends linearly on the pump power. This is the case as long the laser operates in a unique single pulse regime. For higher pump powers, cw background radiation breaks through and the theory on which Eq. (6.11) is based no longer holds because the intracavity power is now divided between two components, the pulse and the cw solution, see Fig.6-1(b) and (c). The observed turning point is not implicit to the pulse dynamics itself, but is due to the appearance of a cw component in the spectrum, as is easy to see in Fig.6-1. After the cw component is present, any increase in pump power enhances the cw component and most likely decreases the pulse energy, causing f_{CE} to eventually shift in the opposite direction. This is a consequence of the fact that the Kerr lens mode-locking (KLM) action does not increase indefinitely, i.e., there is an upper value for the pulse energy and a further increase in pump power will either contribute to cw breakthrough or lead to multiple pulses. Therefore, care must be taken to operate at an optimum pump power level which is significantly below this threshold value for single pulse instabilities. From the data shown in Fig. 6-1, the pump power to carrier-envelope frequency conversion coefficient for the 200 MHz lasers is $C_{fP_p} = 11 \text{ MHz/W}$. Fig. 6-1 also shows the relative change of the intracavity pulse energy as a function of the same variation in pump power. The appearance of a cw component is also explicitly indicated in this measurement by the abrupt change in the observed slope. The shallow slope of the change in the average power in pulsed operation as compared to the change in power in cw operation is an

indication of the strength of the saturable absorption and the bandwidth limitation of the laser. From this data, we can infer a relatively weak response in the change of the pulse energy in mode-locked operation and therefore a correspondingly weak response in the f_{CE} change, which in fact will be confirmed in the transfer function analysis discussed in the next section.

Now, we can compare quantitatively the measured shift of f_{CE} in Fig. 6-1 with the theoretically derived result from soliton perturbation theory. It turns out that the measurement and theory agree very well, despite the fact that the laser dynamics differ from the ideal conventional soliton operation regime.

The conversion coefficient

$$C_{fP_{\text{intra}}} = \Delta f_{\text{CE}} / \Delta P_{\text{intra}}, \quad (6.12)$$

where P_{intra} is the intracavity power in mode-locked operation, can now be determined in terms of known cavity parameters under the assumption of a fixed pulse width,

$$\frac{\Delta f_{\text{CE}}}{\Delta P_{\text{intra}}} = \frac{Ln_2}{4\lambda_c A_{\text{eff}}\tau} \quad (6.13)$$

where $L = 4\text{ mm}$ is the path length per round trip through the Ti:sapphire crystal, $n_2 = 3 \times 10^{-20} \text{ m}^2/\text{W}$ is the nonlinear index of refraction for Ti:sapphire, $\lambda_c = 800 \text{ nm}$ is the carrier wavelength, $A_{\text{eff}} = \pi w_0^2$ ($w_0 = 16 \mu\text{m}$) is the mode cross sectional area, $\tau = \tau_{\text{FWHM}}/1.76$ with a pulse width of $\tau_{\text{FWHM}} = 5 \text{ fs}$, and $P_{\text{intra}} = 12 \text{ W}$ is the intracavity power. This expression gives, for a 5% change in intracavity power, a corresponding change in f_{CE} of 9.6 MHz, which agrees well with the results shown in Fig. 6-1.

Despite this surprisingly good agreement, one has to be aware that the spot size and other parameters are rough estimates, which may easily change depending on cavity alignment. Also the pulse width is not constant in the crystal but rather stretching and compressing by more than a factor of 2. Nevertheless, the experimental observations in Fig. 6-1 agree well with the above theoretical estimate obtained from conventional soliton

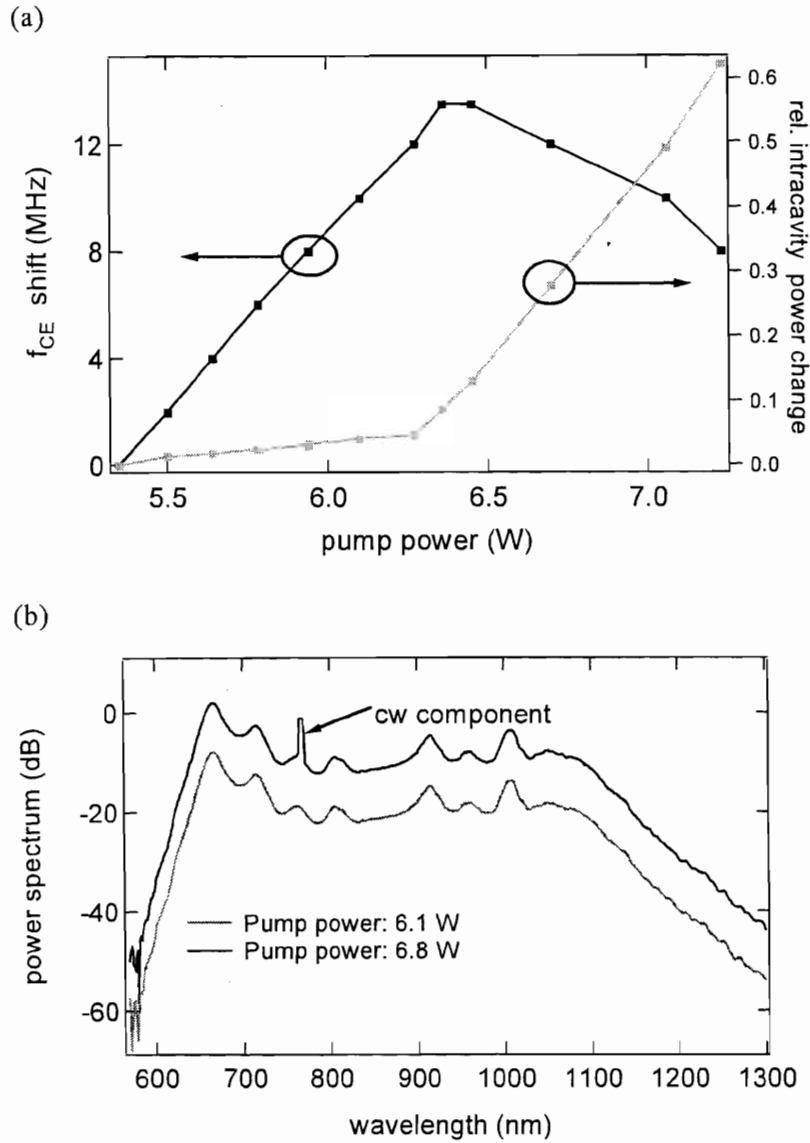


Figure 6-1: (a): Carrier-envelope frequency shift (left axis) and relative change in intracavity power (right axis) as a function of pump power. Both curves make evident the presence of a cw breakthrough for pump powers above 6.3 W, which is confirmed by the appearance of a cw component in the optical spectrum shown in (b). For clarity, the spectra are vertically offset by 10 dB.

formation.

6.2 Noise analysis of f_{CE} -stabilized lasers

The design and overall setup of carrier-envelope phase stabilized OSFC has been extensively discussed in Chapters 4 and 5. We have built two of these OSFCs at 200 MHz repetition rate with slightly different loop filter designs and pumped by different pump lasers. One is using a single-longitudinal-mode (slm) Nd:YVO₄ pump laser (Verdi-V10, Coherent) and the other a multi-longitudinal-mode (mlm) Nd:YVO₄ pump laser (Millennia Xs, Spectra-Physics). Fig. 6-2 depicts the measured relative intensity noise (RIN) for the mlm pump laser and slm pump laser. The mlm pump laser shows significantly higher relative intensity noise in the high-frequency range, whereas the slm pump laser has higher RIN at very low frequencies. Recently, S. Witte *et al.* [67] also characterized the influence of RIN of these pump lasers on the residual carrier-envelope phase noise for a 10-fs Ti:sapphire laser employing chirped mirrors for intracavity dispersion compensation and external spectral broadening in a microstructure fiber, however, no rigorous noise analysis has been performed so far. The purpose of this section is to elucidate the impact of the RIN of different pump lasers on the finally achievable carrier-envelope phase noise and how the feedback mechanism and the design of the feedback loop employed impacts residual carrier-envelope phase noise.

Fig.6-3 shows the corresponding spectrally-resolved and integrated carrier-envelope phase error measured for the two 200 MHz OSFCs which are directly carrier-envelope phase locked. In agreement with the data measured by S. Witte *et al.*, the high-frequency carrier-envelope phase noise is found to be larger for the mlm pump laser. The carrier-envelope phase fluctuations at lower frequencies, which are smaller for the mlm pump laser, are strongly suppressed by the large proportional-integral (PI) control loop gain and therefore do not contribute significantly to the residual carrier-envelope phase noise. The residual carrier-envelope phase fluctuations of the OSFC pumped by the mlm pump

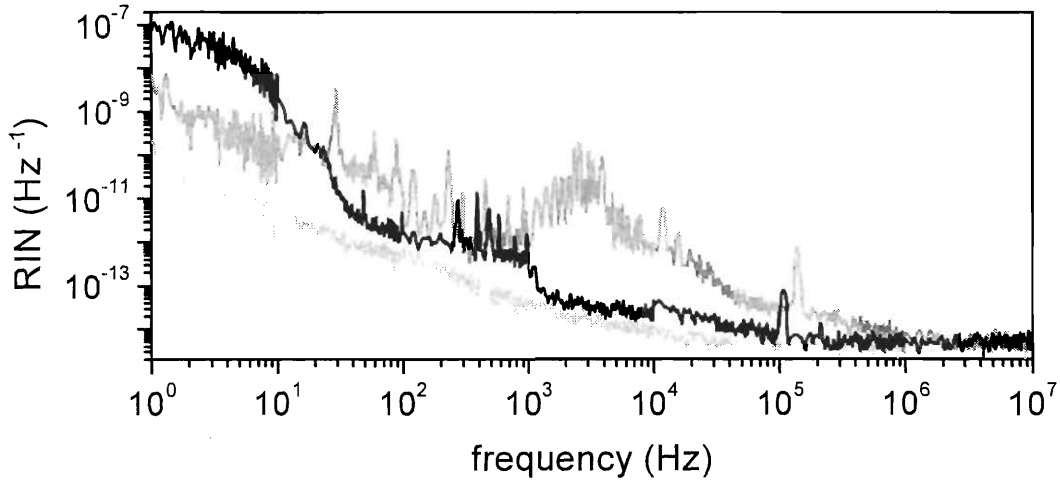


Figure 6-2: Relative intensity noise (RIN) of a Coherent Verdi-V6 (black curve) and a Spectra-Physics Millennia Xs (dark grey curve). The measurement noise floor is given by the black curve.

laser amount to 0.257 rad, compared to only 0.117 rad if the slm laser is used. First of all it is surprising that the mlm pumped system is only 2.2 times worse than the slm pumped system despite the fact that the high-frequency noise of the mlm pump is so much worse. As we will see this is so because the feedback gain is large below 100 kHz. Obviously the system pumped by the mlm pump laser could easily do equally well if the feedback-loop bandwidth could be extended by one order of magnitude. The reasons why the high-frequency noise of the mlm pump can not be further suppressed will be elaborated further in the following feedback analysis.

From a control systems point of view, the f_{CE} -stabilized laser is a phase-locked loop (PLL) [68], where the voltage-controlled oscillator (VCO) is the carrier-envelope frequency controlled OSFC, which is the block indicated by the dashed frame in Fig. 6-4. When the laser is turned on, the carrier-envelope frequency f_{CE} is determined by the cavity parameters and alignment, equivalent to the center frequency of oscillation of the VCO in a PLL. A voltage applied to the acousto-optic modulator (AOM) driver changes this frequency by an amount proportional to the equivalent VCO gain of the system.

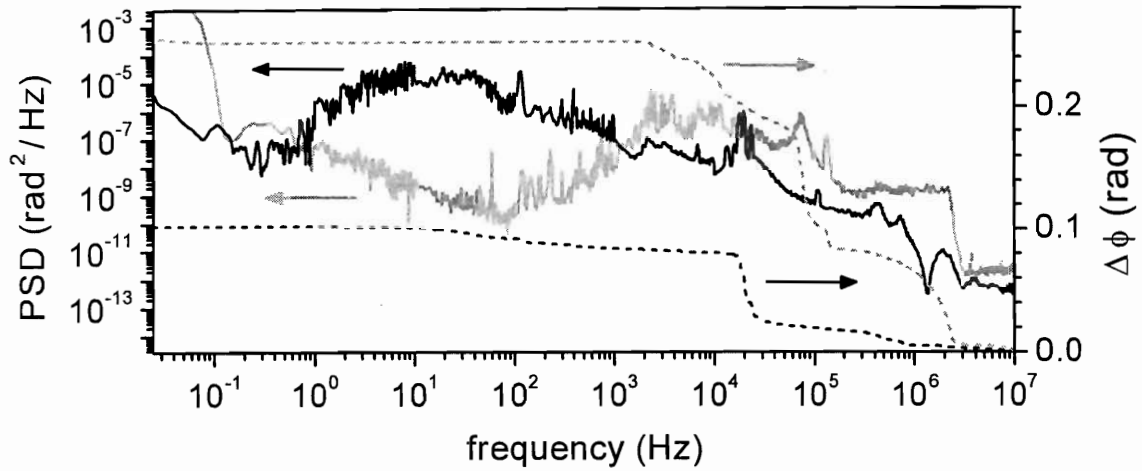


Figure 6-3: Comparison of the carrier-envelope phase noise of a self-referenced 200 MHz Ti:sapphire frequency comb pumped by a Coherent Verdi-V6 (solid and dashed black curves) and by a Spectra-Physics Millenia Xs (solid and dashed grey curves). The solid curves represent the spectral density of the phase noise and the dashed curves represent the accumulated phase.

The model depicted in Fig. 6-4 includes all the electronic components used in the stabilization (phase detector, AOM and loop filter), whose transfer characteristics are easy to measure and to describe by an analytic model. Assuming an instantaneous response of the carrier-envelope frequency to the pump power via a constant C_{fP_p} , one is not able to reproduce the measured carrier-envelope phase noise spectrum. Therefore, the impact of the frequency response of the OSFC system must be taken into account in the analysis, which was done by considering the transfer function between the intracavity laser power (or pulse energy) and the pump power via the laser gain dynamics.

6.2.1 Transfer function representation for the pulse energy versus pump power dynamics

The starting point for derivation of the transfer function are laser rate equations for pulse energy and gain, which can be derived from the master equation (6.5) by proper

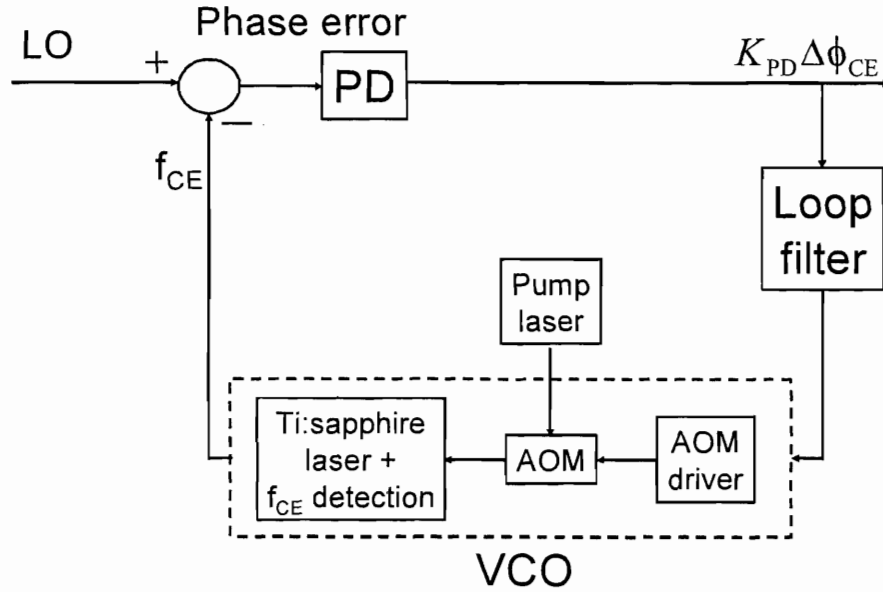


Figure 6-4: Block diagram of the phase-locked loop (PLL) composed of the f_{CE} -stabilized laser. The voltage-controlled oscillator (VCO) is depicted in the dashed box.

elimination of the remaining degrees of freedom in the mode-locked laser as has been derived for example in the case of soliton lasers mode locked by slow saturable absorbers [69, 70]. One can write

$$T_R \frac{dE}{dT} = (g - l - q(E))E \quad (6.14)$$

$$T_R \frac{dg}{dT} = -\frac{g - g_0}{\tau_L/T_R} - g \frac{E}{E_{\text{sat}}} \quad (6.15)$$

where

- T_R = cavity round-trip time,
- τ_L = upper state lifetime,
- l = total non-saturable loss,
- $q_{\text{ml}}(E)$ = effective energy-dependent saturable absorber and filter loss (for more detail, e.g., see Ref. [70]),
- g_0 = small-signal gain, which is proportional to pump power,
- E_{sat} = saturation energy of the gain medium.

Many assumptions have been made when using these equations to describe the energy and gain dynamics. For example, possible frequency shifts and back action of the background radiation onto the energy and gain dynamics, i.e., the details of the pulse shaping mechanism, are neglected. We have denoted the time coordinate as capital T to emphasize the fact that this dynamics occurs on the time scale of many cavity round trips. This is possible for solid-state laser gain media because the interaction cross section is small and therefore the gain saturates with average power rather than with a single passage of the pulse through the gain medium [69].

Note that the most important term in the rate equations is the mode locking related energy-dependent loss $q_{\text{ml}}(E)$, which comprises the loss during saturation of the absorber as well as additional losses due to the bandwidth limitations of the system, which increase with additional spectral broadening or increasing intracavity pulse energy [70]. A typical characteristic dependence of $q_{\text{ml}}(E)$ on intracavity pulse energy is shown in Fig. 6-5. To derive a transfer function for the laser, we linearize Eqs. (6.14) and (6.15) around the steady-state operating point, denoted by the subscript s : $E = E_s + \Delta E$, $g = g_s + \Delta g$, $g_0 = g_{0s} + \Delta g_0$, $q(E) = q(E_s + \Delta E) \approx q(E_s) + \frac{\partial q}{\partial E}|_{E=E_s} \Delta E \equiv q_s + \frac{\partial q}{\partial E_s} \Delta E$ to get the set

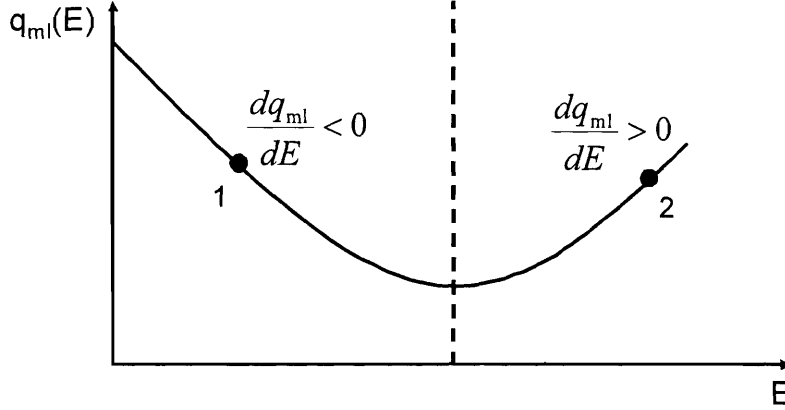


Figure 6-5: Mode locking related energy-dependent loss $q_{ml}(E)$. Stable mode locking occurs at operating point 2 where $dq_{ml}/dE > 0$.

of linearized equations

$$T_R \frac{d\Delta E}{dT} = -\frac{\partial q}{\partial E_s} E_s \Delta E + E_s \Delta g \quad (6.16)$$

$$T_R \frac{d\Delta g}{dT} = -\frac{T_R}{\tau_{stim}} \Delta g - \frac{g_s}{E_{sat}} \Delta E + \frac{T_R}{\tau_L} \Delta g_0 \quad (6.17)$$

where τ_{stim} is the stimulated lifetime given by $\tau_L (1 + \tau_L E_s / T_R E_{sat})^{-1}$. By taking the Laplace transform of the above equations ($\frac{d}{dT} \Rightarrow s$, where s is the Laplace variable, equal to $-i\omega$), it is straightforward to derive a *pump power to pulse energy* transfer function, by writing g_0 as $K_{g_0} P_p$. Defining the pump parameter $r = 1 + \tau_L E_s / T_R E_{sat} \equiv 1 + P_s / P_{sat}$, which indicates how many times the laser operates above threshold, we arrive at

$$\Delta \tilde{E} = \frac{P_s K_0 / \tau_L}{s^2 + \left(\frac{r}{\tau_L} + \frac{\partial q}{\partial E_s} P_s \right) s + P_s \frac{\partial q}{\partial E_s} \frac{r}{\tau_L} + \frac{r-1}{\tau_L \tau_p} \left(1 + \frac{g_s}{l} \right)} \Delta \tilde{P}_p, \quad (6.18)$$

where $\tau_p = T_R / l$ is the photon decay time due to the linear cavity losses in cw operation. So far we have considered the mode-locked case, but a similar relation can be obtained for the intracavity power in cw operation simply by setting the saturable absorber terms

in Eq. (6.18) to zero:

$$\Delta\tilde{P}_{intra} = \frac{P_s K_0 / \tau_L}{s^2 + \frac{r}{\tau_L} s + \frac{r-1}{\tau_L \tau_p} + \frac{q_s}{l}} \Delta\tilde{P}_p. \quad (6.19)$$

However, the laser parameters, like mode cross section in the gain medium likely change values when the laser changes from cw operation to mode-locked operation, but since we have no way of measuring them in mode-locked operation, we have estimated them based on our knowledge of laser parameters in cw operation and used those to examine the effect of the inclusion of the saturable absorber into the transfer function. Fig. 6-6 shows the pump power to intracavity power transfer functions, in amplitude and phase, for cw and mode-locked operation for different values of the term $\frac{\partial q}{\partial E_s} P_s$. It is obvious that the mode locking of the laser drastically changes the transfer characteristic between pump power and intracavity power due to the pulse operation, which introduces the term $\frac{\partial q}{\partial E_s} P_s$ into the rate equation (6.16). Depending on its sign this term enhances (for $\partial q / \partial E < 0$ it may lead to Q-switching when large enough) or strongly damps (for $\partial q / \partial E > 0$) intracavity energy fluctuations. In cw operation its absence usually leads to pronounced relaxation oscillations, see Fig. 6-6. As we can see, the stronger the effective inverse saturable absorption, the more damped become the relaxation oscillations in the laser, and the weaker becomes the response at all frequencies. This result has to be expected, because the stronger the inverse saturable absorption the more clamped become the pulse energy and the average power.

The model is verified by measuring the transfer function of the laser in cw and mode-locked operation. The measurement is performed by using a network analyzer (Agilent 4395A) as shown in Fig.6-7. Care has to be taken to assure that no cw component is present in mode-locked operation during the measurements. The results are shown in Fig.6-8. Also shown in the same plots are the amplitude and phase of the transfer function given by Eq. (6.18). For the cw case, $q(E) = 0$. The parameter r was measured to be 3.22, while the intracavity loss, l , which determines the value of τ_p and comes in the expression for the relaxation oscillation of the cw laser $\omega_r = \sqrt{\frac{r l}{\tau_L T_R}}$, was used to fit the model with the measured result for the cw case. The value obtained was $l = 0.22$. K_{g_0}

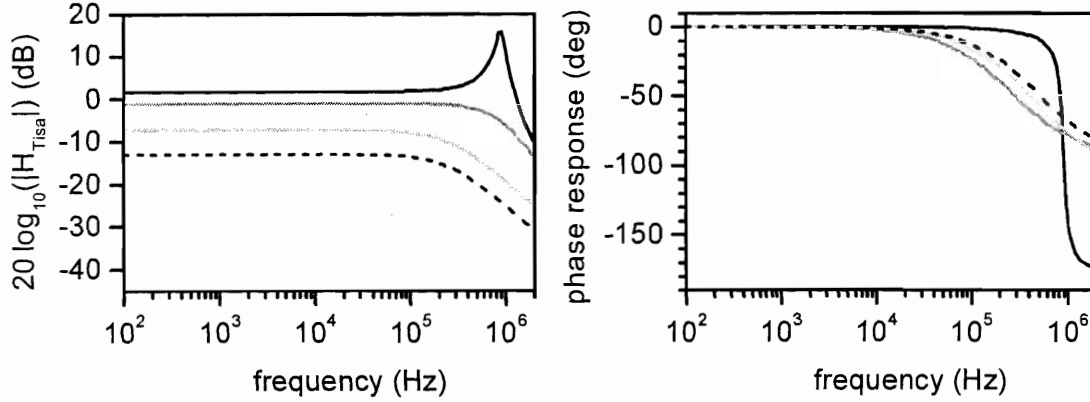


Figure 6-6: Calculated amplitude and phase response of intracavity power with pump power for cw operation (black) and for different values of saturable absorption: $\frac{\partial q}{\partial E_s} P_s = 10r/\tau_L$ (dark grey), $\frac{\partial q}{\partial E_s} P_s = 50r/\tau_L$ (light grey) and $\frac{\partial q}{\partial E_s} P_s = 150r/\tau_L$ (dashed).

was then calculated using the relationship $g_0 = K_{g_0} P_p = rl = 0.15$ [17]. As can be seen in Fig. 6-8, the model describes well the gain dynamics in cw operation. For the mode-locked case, we included the effect of the saturable absorber and modified the other parameters in such a way as to fit the measured and calculated transfer functions as close as possible, especially for frequencies beyond 10 kHz, where the impact on the final noise calculation is most pronounced. A close fit was achieved by setting $\frac{\partial q}{\partial E_s} P_s = 150 r/\tau_L$, $q_s = l$, $l = 0.17$, $r = 3.5$ and $K_{g_0} = 0.23$. Fig. 6-8 shows that the approximations made in the model do not fully describe the system, i.e., we neglect the interaction with the continuum, which is an infinite-dimensional system. In the measurements, a significant change in the amplitude response from low to high frequencies, in the 1–100 kHz range, is observed in mode-locked operation, which is an indication of additional slow processes that may be occurring in the mode-locked laser that are absent in the cw laser. Nevertheless, the model gives good qualitative and quantitative description of the laser dynamics and the final transfer function mimics the global behavior of the measured transfer function while still being simple. It confirms our observations on the strength of the saturable absorption in such systems, explicit in the measurements shown in Fig. 6-1. As will be

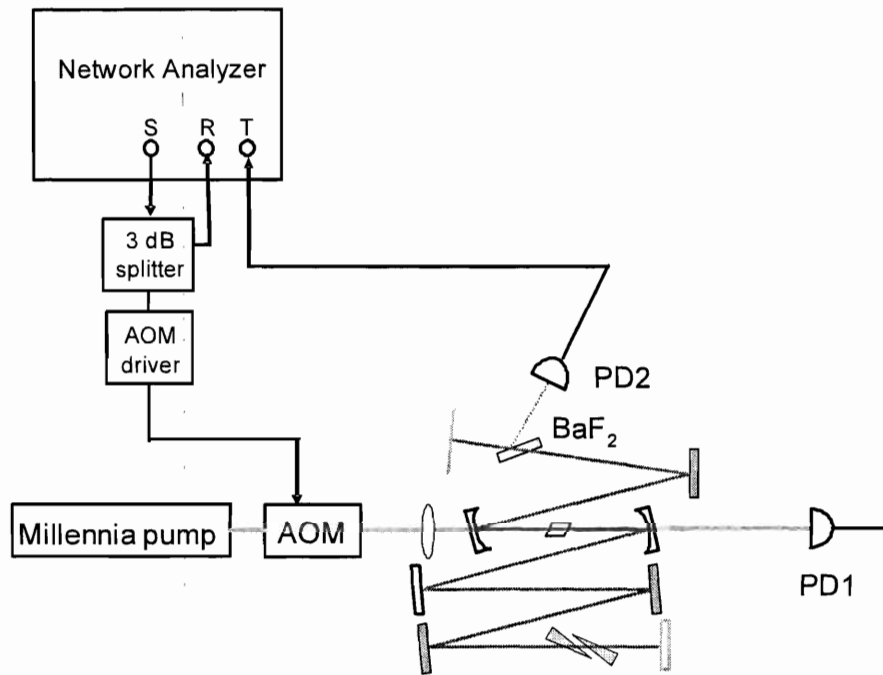


Figure 6-7: Schematic of the transfer function measurement setup. In order to measure only the contribution from the laser itself, a first calibration measurement is performed with PD1 measuring the AOM and AOM driver response (PD1 and PD2 are the same photo detector, Thorlabs model PDA-55). The laser transfer function is measured by the network analyser, Agilent model 4395A, by detecting with PD2 the reflection from one intracavity BaF₂ plate.

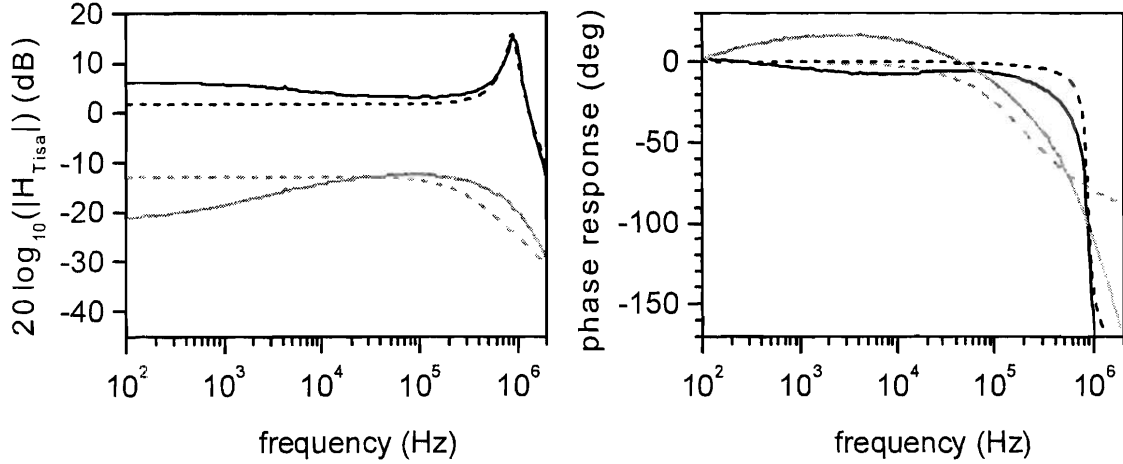


Figure 6-8: Measured (solid curves) and modelled (dashed curves) amplitude and phase response of OSFC laser, in CW and mode-locked operation.

shown in the next section, the inclusion of this transfer function in the noise analysis is essential in deriving the correct noise behavior of the system.

6.2.2 Determination of the carrier-envelope phase error

To calculate the carrier-envelope phase noise spectrum of the OSFC, a linear noise analysis is performed. The block diagram in Fig. 6-9 shows the closed loop system. The input noise source, characterized by the power spectral density of the pump noise $S_P(s)$, which is the RIN multiplied by the square of the pump power, is converted to the carrier-envelope phase noise spectral density $S_\phi(s)$ in the laser and is partially suppressed in the feedback loop. The feedback path consists of the phase detector, the loop filter and the AOM, with transfer functions denoted by $H_{PD}(s)$, $H_{LF}(s)$ and $H_{AOM}(s)$, respectively. Table 6.1 shows the corresponding analytic expressions. The loop filter consists of a simple PI controller and the AOM is, up to a small drop in amplitude for higher frequencies, equivalent to a delay line with a propagation delay given by the time it takes for the acoustic wave to travel from the piezoelectric transducer to the optical beam. We set

this delay to $1.73 \mu\text{s}$ to match the measured transfer function. The limitations of the bandwidth of the AOM are not taken into account here because the measurements show that it is approximately flat out to 1 MHz, whereas we observe that our loop bandwidth is significantly smaller. The calculated and measured transfer functions for the loop filter and the AOM are shown in Fig.6-10. We consider the phase detector (Analog Devices AD9901) transfer function to be flat based on its datasheet.

In the noise analysis we consider the case of the OSFC pumped by the multi-longitudinal-mode pump laser because of the increased high-frequency noise in such systems as discussed above. Given the RIN measurement in Fig.6-2 as the input noise source, we calculate $S_\phi(s)$ using the transfer functions in Table 6.1 to derive the closed loop transfer function that describes the conversion of pump noise $S_P(s)$ to carrier-envelope phase noise $S_\phi(s)$,

$$H_{\text{CL}}(s) = \frac{H_{\text{Tisa}}(s)}{1 + H_{\text{Tisa}}(s)H_{\text{PD}}(s)H_{\text{LF}}(s)H_{\text{AOM}}(s)}. \quad (6.19)$$

Then, $S_\phi(s)$ is obtained by multiplying the absolute intensity noise of the pump laser, $S_P(s)$, with the magnitude squared of H_{CL} given by expression (6.19) [68]:

$$S_\phi(s) = |H_{\text{CL}}(s)|^2 S_P(s). \quad (6.20)$$

The calculated and measured carrier-envelope phase noise are shown in Fig.6-11. Already given in the previous section, the values for the parameters used in $H_{\text{Tisa}}(s)$ are those which closely match the measured and calculated OSFC transfer function in mode-

Table 6.1: Transfer functions of the Ti:sapphire laser, phase detector, loop filter, and AOM.

$H_{\text{Tisa}}(s)$	$\frac{P_s K_0 / \tau_L}{s^2 + \left(\frac{\tau}{\tau_L} + \frac{\partial q}{\partial E_s} P_s\right) s + P_s \frac{\partial q}{\partial E_s} \frac{\tau}{\tau_L} + \frac{\tau-1}{\tau_L \tau_P} (1 + \frac{q_s}{l})} \times \frac{C_f P_{\text{intra}}}{s T_R}$
$H_{\text{PD}}(s)$	K_{PD}
$H_{\text{LF}}(s)$	$\frac{1 + \tau_2 s}{\tau_1 s} \frac{1}{(1 + \tau_3 s)^3}$
$H_{\text{AOM}}(s)$	$e^{-s \tau_{\text{delay}}}$

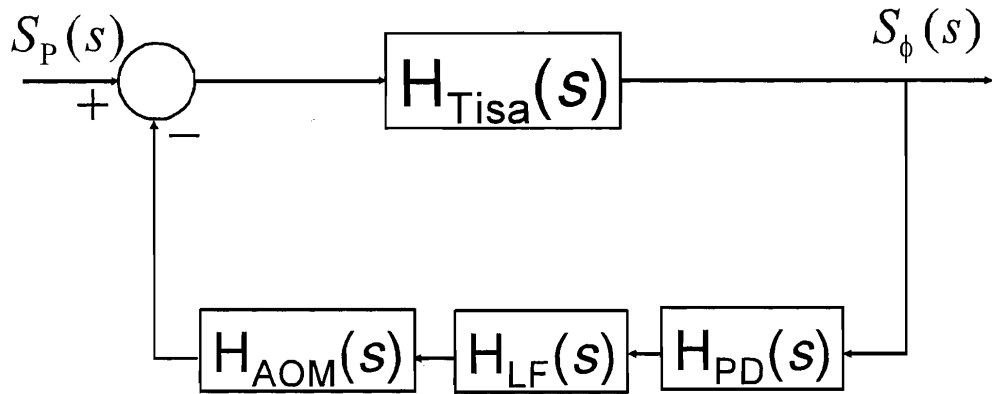


Figure 6-9: Block diagram describing the addition of intensity noise to the laser PLL.

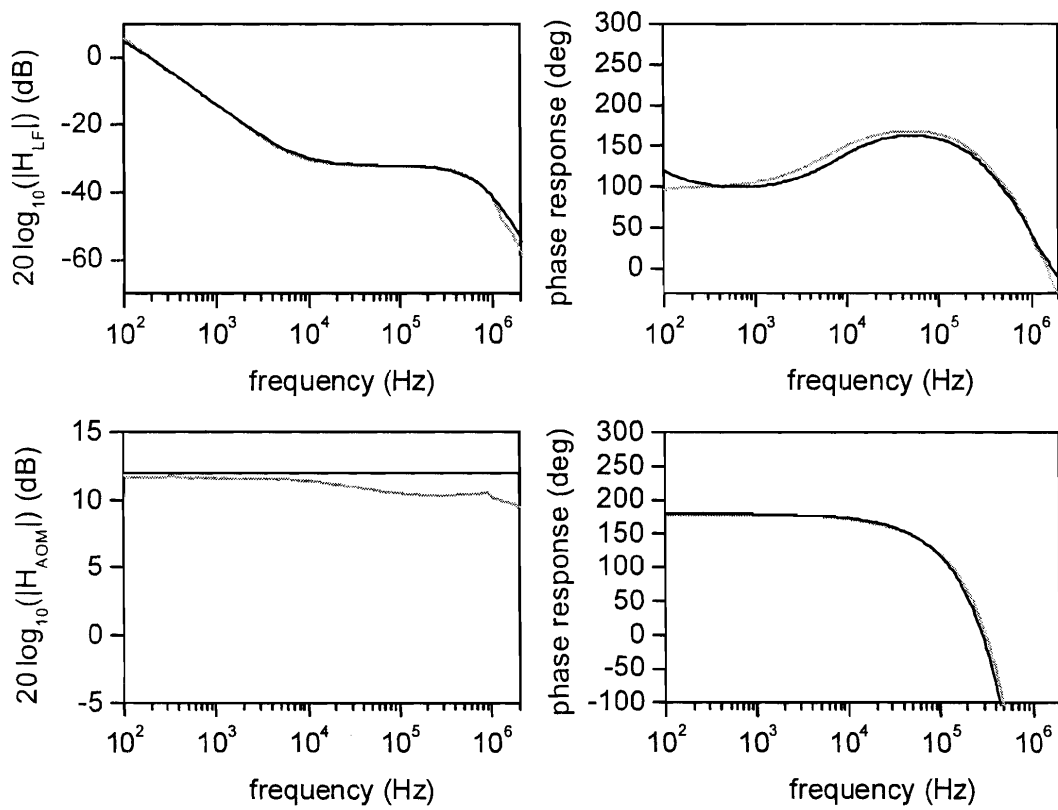


Figure 6-10: Measured (grey) and calculated (black) transfer functions for loop filter (top) and AOM (bottom).

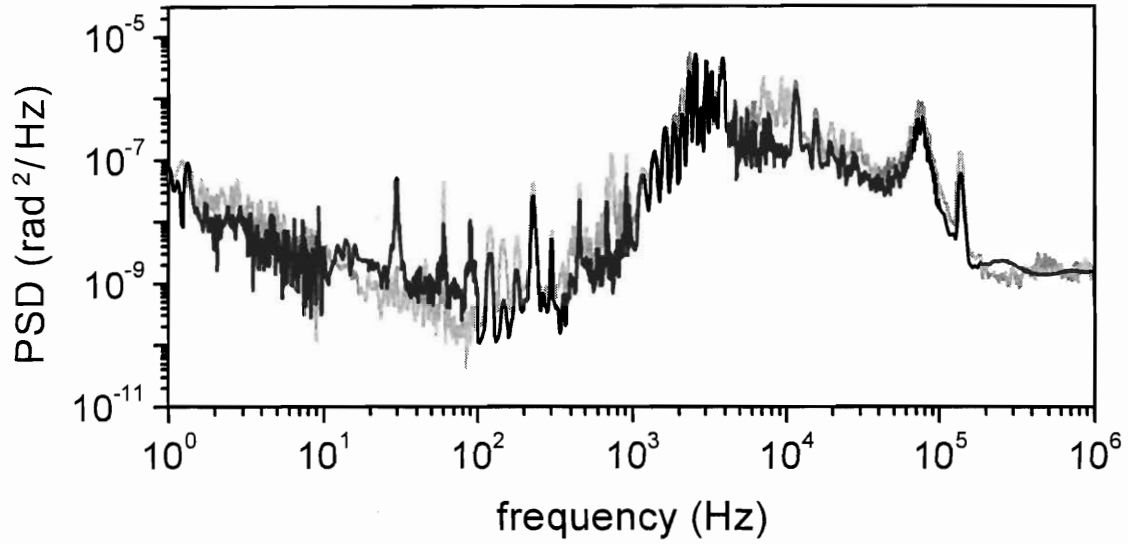


Figure 6-11: Carrier-envelope phase noise spectrum of the Millenia-Xs-pumped OSFC. The red curve is the calculated spectrum and the blue curve is the measurement.

locked operation in the range between 10 kHz and 1 MHz. When only the pump noise was used as a noise source, we found that the calculated and measured $S_{\phi}(s)$ showed good agreement up to 200 kHz, beyond which point the measurement showed enhanced noise. This was determined to be due to electronic noise at the output of the phase detector, which needs to be considered as an additional noise source in the analysis to get a good fit beyond 200 kHz. We added this white noise source S_{PD} in the loop, which converts to a final contribution to $S_{\phi}(s)$ by the closed-loop transfer function

$$H_{CL}^{wn}(s) = \frac{1}{1 + H_{Tisa}(s)H_{PD}(s)H_{LF}(s)H_{AOM}(s)}. \quad (6.21)$$

where the magnitude of the noise source S_{PD} was estimated based on the measurement. To verify the importance of the effect of the laser dynamics on the predicted noise, we have performed the same noise calculation, but considering only the integrating effect of the VCO on the phase and neglecting the transfer function 6.18, as shown in Fig. 5-2. Figure 6-12 shows such a simulation compared to the measured phase noise.

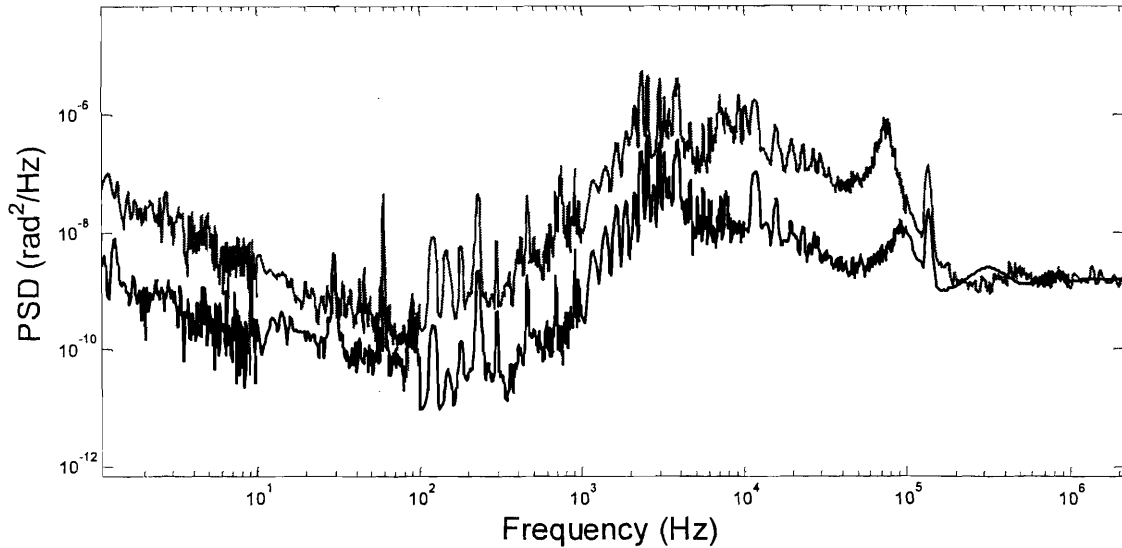


Figure 6-12: Calculated (black) and measured (grey) phase noise spectrum of carrier-envelope phase stabilized laser without taking the laser gain dynamics into account in the simulation. Because the low-pass filtering effect of the laser dynamic is absent, it is in theory possible to suppress the noise further without compromising the loop stability.

Improved noise performance could be obtained by increasing the closed-loop bandwidth, which is currently about 100 kHz. This bandwidth is dictated by the phase margin of the feedback loop, which according to the Nyquist theorem may run unstable when the gain is larger than 1 while the phase approaches 180° [56]. Note that the VCO integrates a frequency deviation into a phase deviation causing the feedback loop to start off with a -90° phase, as can be seen in Fig. 6-13. When the bandwidth of the gain medium is approached, additional phase accumulates from the gain dynamics and the time delay from the AOM (see Fig. 6-13), which renders the system unstable if the gain setting is not properly reduced. Of course, for a reasonably stable system and optimum operation of the feedback loop, large enough gain and phase margins are necessary. This imposes a limitation to the maximum loop gain since the jointly added phase from $H_{\text{AOM}}(s)$ and $H_{\text{Tisa}}(s)$ contribute to a decrease in the phase margin. However, now that the different phase contributions to the feedback loop are well understood, the noise suppression at

high frequencies could be improved by custom design of the control electronics. For example, by adding a lead-lag compensator [56], the limitation from the added phases could be overcome. Also, replacing the AOM by an electro-optic modulator would eliminate the contribution to the open-loop phase from the time delay of the AOM.

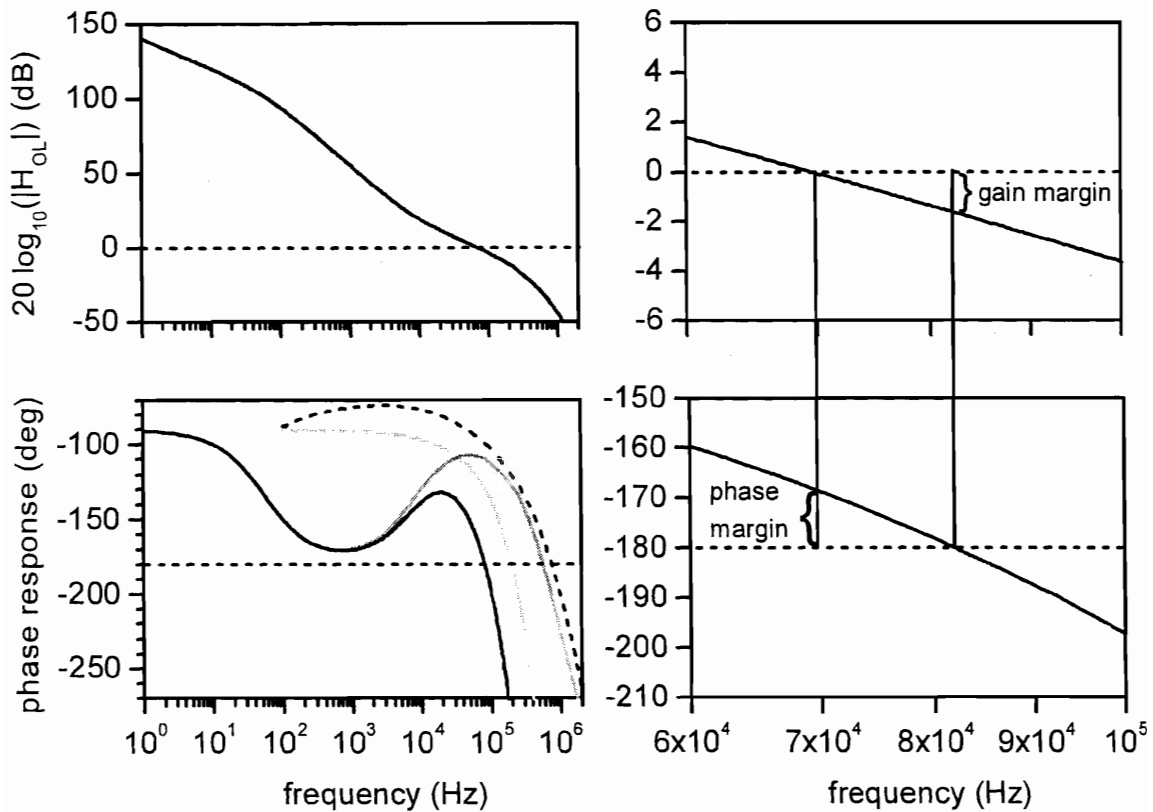


Figure 6-13: Amplitude (top) and phase (bottom) of open-loop transfer function of the laser PLL (solid black curves) corresponding to Fig. 6-9. The contribution from the loop filter (dark grey), AOM (light grey) and laser dynamics (dashed) to the open-loop phase are also shown. The zoomed plots on the right-hand side confirm that the PLL satisfies the Nyquist stability criterium (with gain margin 2 dB, phase margin 12°).

Chapter 7

Applications to frequency metrology of ultracold hydrogen

This frequency comb has been developed with the goal of carrying out ultraprecise spectroscopy of ultracold hydrogen and also of creating an optical clock based on the 1S-2S two-photon transition. As the first step of applying optical frequency metrology to atomic hydrogen, we planned to study two-photon optical transitions originating from the 2S state, which is metastable. The frequency comb would be used to measure the frequencies of several 2S- n S transitions, with n higher than 6, directly in terms of the frequency of the 1S-2S transition, which has been measured to about 1 part in 10^{14} [71]. The goal for precision in these measurements is relatively modest -about part in 10^{12} - but this would be of immediate scientific value, leading to a ten-fold increase in the precision of the Rydberg constant and contribute to an improvement of the knowledge of the Lamb shift in hydrogen. Furthermore, such a measurement would be directly in line toward the next step, improving the precision of the 1S-2S frequency, currently the best known optical frequency, to significantly greater than 1 part in 10^{14} .

The rationale for pursuing two-photon spectroscopy of ultracold metastable hydrogen with the goal of improving on the frequency measurement of these transitions is discussed in more detail in the thesis of Kendra Vant [2]. Because the diode laser system presented

in that thesis was specifically designed to perform two-photon spectroscopy copy of the 2S-8S transition, Section 7.1 will be devoted to describing how this frequency measurement can be performed using our existing system. However, this same approach can be applied to measuring any 2S- n S transition, with n in the range from 6 to 12, since the comb spectrum spans the whole frequency range in question. Techniques for carrying out two-photon spectroscopy of 2S metastables are described in [2].

As the ultimate goal of our optical frequency metrology efforts at MIT is to improve the determination of the 1S-2S transition, Section 7.2 is devoted to describing how that experiment can be performed. The focus of the discussion here is on the frequency metrology aspects of this experiment. The experimental methods of the spectroscopy in itself will be described elsewhere.

7.1 Measuring the 2S-8S transition

The frequency of the 2S-8S transition can be found by using the comb to bridge the 77 THz frequency gap between a laser stabilized to hydrogen at 486 nm - one quarter of the 1S-2S frequency - and a laser tuned to the 2S-8S two-photon transition at 778 nm, as the schematic on Fig. 7-1 shows. An important aspect of this scheme is that the 1S-2S transition serves as our frequency reference, known to 1.8 parts in 10^{14} .

The schematic of the optical setup can be seen in Fig. 7-2. The atomic transition is probed by a diode laser stabilized to the comb at 778 nm (not shown). A beatnote is generated between the output of that laser and a line of the frequency comb. Mode preselection is done with the help of an optical grating (for details, see [2]). Obtaining good S/N in this case is the most challenging of all the optical beatnotes involving the comb. For two cw lasers with about the same power available, the one which provides the narrowest linewidth will generate a larger S/N in the beatnote with the comb line. The dye laser which is used to stabilize the comb is itself stabilized to a high-finesse cavity, providing it with a linewidth on the order of 1 kHz. In contrast, the diode laser, which

is to be locked to the comb, has a relatively broad passive linewidth of 300 kHz. This makes the comb-diode beat signal correspondingly broader, with a lower peak S/N than the dye-comb beat signal. The best we have observed is 30 dB in 100 kHz RBW, just enough for phase locking without cycle slips. In this case, the diode laser is locked to the frequency comb by means of a PLL with the same electronic circuits already described in the previous chapter. The error signal is fed back to the diode laser, and phase-locking without cycle slips can be obtained by increasing the linear phase detection range to 32π .

The first step in performing a frequency measurement involves of course locking the comb to the 1S-2S transition in hydrogen as described in Chapter 5. Then, the diode laser is locked to the comb and therefore also referenced to the 1S-2S transition. As can be seen in the diagram in Fig. 7-3, a determination of the 2S-8S frequency requires determining the quantities f_{CE} , f_R , m , n , f_{beat1} and f_{beat2} . The RF frequencies f_{CE} , f_R , f_{beat1} and f_{beat2} are measured using frequency counters as Fig. 7-4 shows. The next step requires unambiguously determining which comb line each laser is locked to, which amounts to determining the integers m and n in the diagram of Fig. 7-3 to a precision better than ± 1 . Since we do not have a wave meter with enough resolution to distinguish individual comb lines, this absolute frequency calibration can be done by utilizing intermediate absolute frequency references. The requirement is that they can determine the frequency of the cw lasers to better than the repetition rate, or 191 MHz. For the dye laser, at 486 nm, the frequency is generally known absolutely to within 20 kHz or less, since the 1S-2S signal serves as our reference and has routinely been observed in our apparatus with typical linewidths of 10 kHz. For the 778 nm laser, a molecular iodine frequency reference can be used to determine the 2S-8S frequency to within 10 MHz, adequate to determine the nearest comb line, since these are separated by 191 MHz. Given the cw laser frequencies and the 4 measured RF frequencies from counters 1, 2, 3 and 4, we can

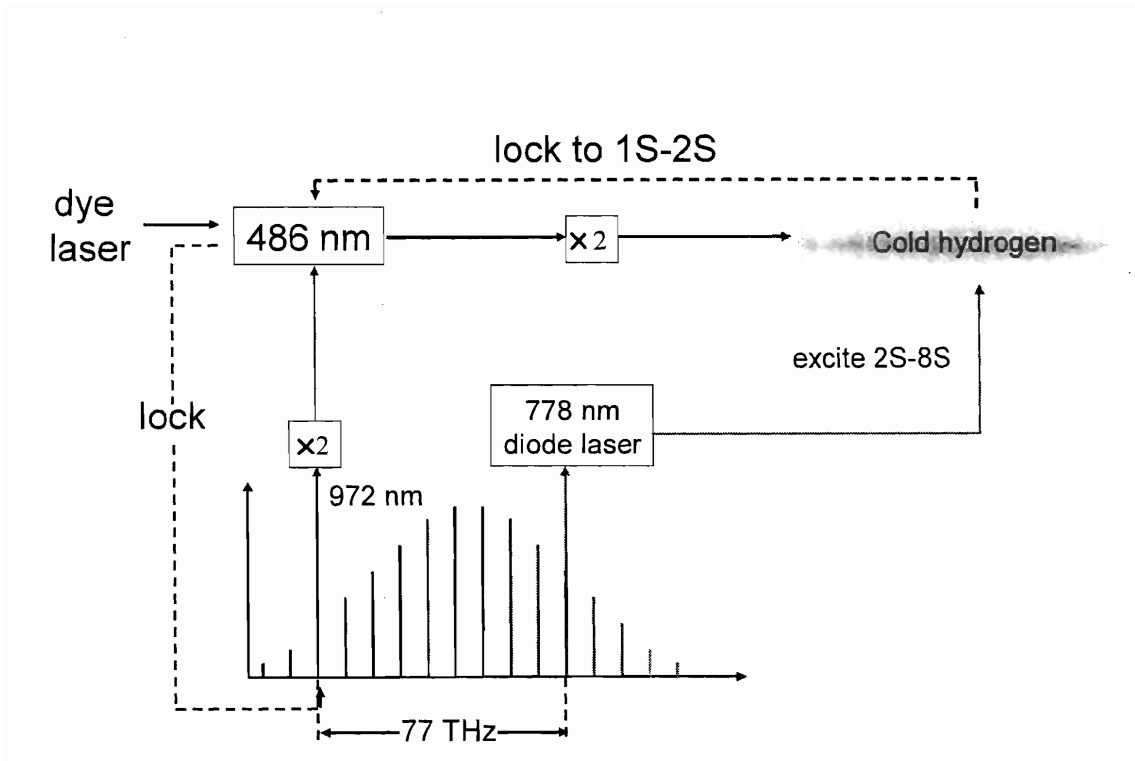


Figure 7-1: Schematic representation of complete setup to perform optical frequency metrology of ultracold hydrogen. The comb bridges different optical transition frequencies, in this case 1S-2S to 2S-8S.

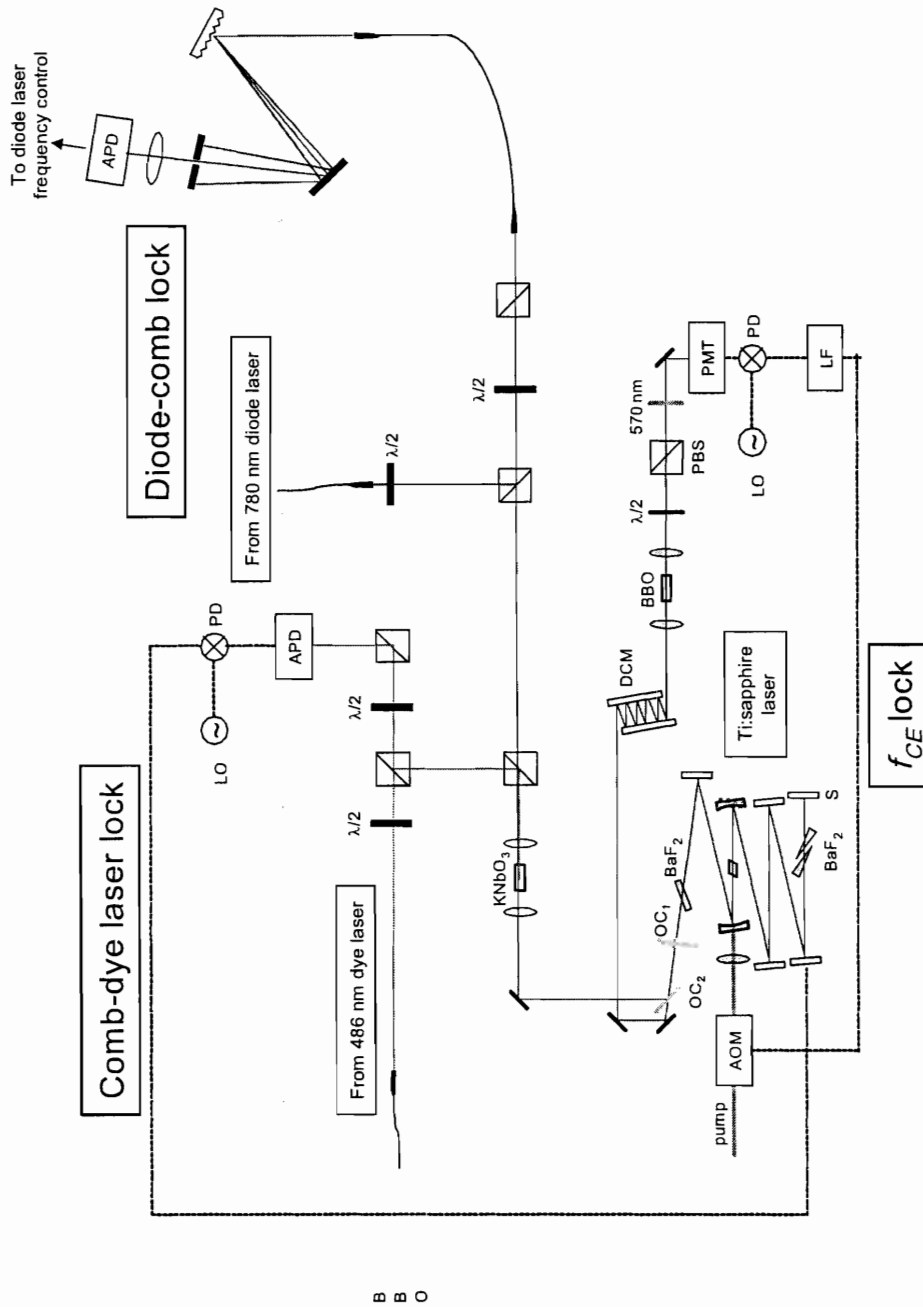


Figure 7-2: Complete optical setup for metrology of ultracold hydrogen. The section here that has not been shown previously is the heterodyne beat setup between the comb and the 2S-8S spectroscopy diode laser. It is similar to the comb-dye laser setup with the only difference being the mode pre-selection, which is done here with the help of a grating.

express the relationship between them as:

$$\begin{aligned} f_{\text{beat1}} &= \pm(2\nu_n - 2(\frac{1}{8}\nu_{1S-2S})) \\ &= \pm(2nf_{\text{R}} + 2f_{\text{CE}} - \frac{1}{4}\nu_{1S-2S}) \end{aligned} \quad (7.1)$$

and

$$\begin{aligned} f_{\text{beat2}} &= \pm(\nu_{m-}\nu_{2S-8S}^*) \\ &= \pm(mf_{\text{R}} + f_{\text{CE}} - \nu_{2S-8S}^*) \end{aligned} \quad (7.2)$$

where the factor of 2 in Eq. 7.1 comes from the fact that we double the comb to observe the beat signal f_{beat1} with the dye laser. The star (*) in Eq. 7.2 is to indicate that this is a "coarse" number obtained from the iodine reference and not the final frequency measurement. As a convention, f is used for radio frequencies and ν is used for optical frequencies. The \pm sign in both equations is to account for the possibility of the beat being between the cw laser and the comb line directly above (+) or below (-) in frequency. This can be easily determined by observing how the beat signal changes as a positive voltage is given to the PZT which controls the laser cavity length. For simplicity lets assume the beat is between the cw laser and the comb line directly above it. Then, we get

$$n = \frac{f_{\text{beat1}} - 2f_{\text{CE}} + \frac{1}{4}\nu_{1S-2S}}{2f_{\text{R}}} \quad (7.3)$$

and

$$m = \frac{f_{\text{beat2}} - f_{\text{CE}} + \nu_{2S-8S}^*}{f_{\text{R}}}. \quad (7.4)$$

Since $\frac{1}{4}\nu_{1S-2S} = 616$ THz and $\nu_{2S-8S}^* = 385$ THz, in order to determine m and n to within ± 1 it is necessary for this purpose to measure f_{R} to better than 60 Hz, easily achievable with any standard frequency counter.

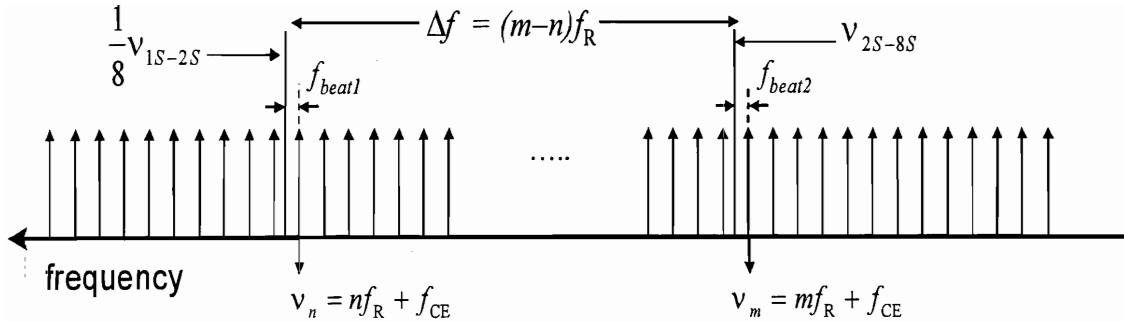


Figure 7-3: Schematic representation of relevant quantities in relation to each other in the frequency domain. This is a simplified representation where a cw laser is present at 972 nm which generates f_{beat1} . In reality, as previously described, the comb is converted to 486 nm via SFG.

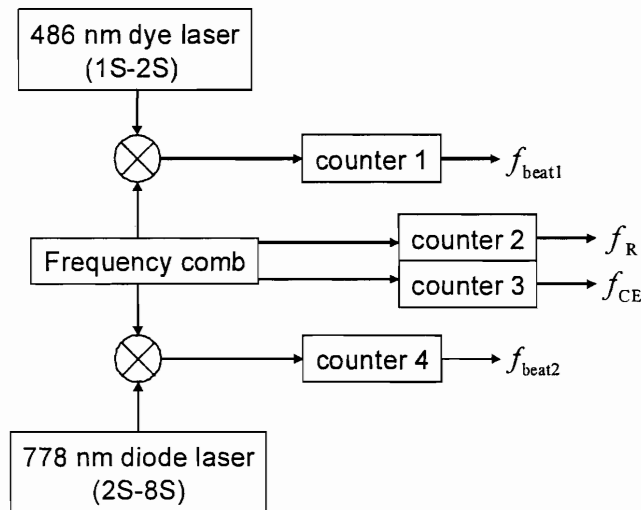


Figure 7-4: Frequency measurement setup, with four frequency counters to measure the comb parameters f_{CE} and f_R as well as the heterodyne beats with the cw lasers.

Given the values of m and n , the relative value for the 2S-8S transition is

$$\nu_{2S-8S} = \frac{m}{2n}(f_{\text{beat1}} - 2f_{\text{CE}} + \frac{1}{4}\nu_{1S-2S}) + f_{\text{CE}} - f_{\text{beat2}}. \quad (7.5)$$

It is clear from the previous expression that the (un)certainty obtained in this measurement is limited by the uncertainty in ν_{1S-2S} . All of the radio frequencies are phase-locked to a stable synthesizer and offer no contribution to the final uncertainty at the level of 10^{-12} . To give an example, a moderately stable RF source at 50 MHz with a stability of 10^{-11} will add only $5 \times 10^7 \times 10^{-11} = 5$ mHz noise to the final measurement, about 1 part in 10^{-17} . On the other hand, the dye laser has a linewidth of a few kHz, 6 orders of magnitude larger than the typical RF noise.

7.2 Measuring the 1S-2S transition

With a 1.2 Hz natural linewidth at a center frequency of 1200 THz (relative (in)stability of 10^{-15}), the 1S-2S transition in hydrogen offers possibilities of unprecedented resolution and precision and potentially one of the highest accuracies for physical measurements. The measurement of this transition frequency at the Max-Planck Institute for Quantum Optics (MPQ) is one of the most precise determinations of an optical frequency to date, currently limited at 1.8 parts in 10^{14} . Further improvement of systematic uncertainties are an obstacle to increasing the accuracy of these measurements, currently at 500 Hz, that are performed on a cryogenically cooled atomic beam. The advantages offered by an ultracold sample of hydrogen include dramatic reduction of systematic uncertainties such as Doppler shifts and AC stark shifts caused by the strong light intensities typical to atomic beam experiments. The metastable 2S atoms have been observed to remain in our trap for 100 ms, close to the natural lifetime of 122 ms [72]. If a stable enough laser were available, this would mean the capability of observing a linewidth of 1.6 Hz. This has motivated the development of an improved laser at 486 nm. Such an improved 1S-2S frequency measurement would be an important addition to the recent explosion of

optical frequency measurements enabled by frequency comb techniques that have taken place in the last four years (see, for example, [71],[73],[74]).

For an absolute optical frequency measurement, it is necessary that the optical frequencies of the comb be determined by the microwave hyperfine transition in cesium that defines the second. However, the operation can be reversed to create an atomic clock based on the optical transition itself. By locking a comb line to an optical transition, the repetition rate signal of the comb is a frequency submultiple of the optical clock oscillator. From the schematics in Fig. 7-3, we can see that the 1S-2S transition frequency is written in terms of measurable quantities as

$$\nu_{1S-2S} = 4[2(nf_R + 2f_{CE}) - f_{beat1}]. \quad (7.6)$$

By heterodyning f_R with a microwave signal generated from the Cs standard, an absolute value for the 1S-2S transition can be given. The beat signals that appear in the above expression will also be determined by the microwave standard, as it will also synchronize all the synthesizers used as local oscillators in the comb stabilization.

In our comb stabilization scheme, the comb lines are not referenced to any microwave frequency standard but to the optical transition which we wish to measure. It might seem more straightforward to lock the comb to a microwave frequency standard and directly derive from the measured beat signals the absolute value for the optical transition. The motivation for favoring optical stabilization of the comb (locking a comb line to the dye laser) over microwave stabilization (locking a microwave harmonic of the repetition rate to a Cs standard) was the inherent advantage of the first scheme, where a frequency division process is involved, in comparison to a frequency multiplication in the latter scheme. Another strong motivation was the lack of a highly stable RF signal source available, such as a hydrogen maser or a commercial Cs clock. We propose that, when such a microwave standard is made available for these measurements, an absolute 1S-2S measurement can be performed with the current stabilization scheme by measuring our generated "clock" signal relative to the microwave standard.

Chapter 8

Conclusion and outlook

To conclude, we have demonstrated the first frequency comb based on an octave-spanning, prismless Ti:sapphire laser. The self-referencing is done directly from the output spectrum of the laser without the need for external fiber broadening. Dispersion compensation is obtained with the use of double-chirped mirror pairs, that provide smooth group delay over the full octave, between 600 and 1200 nm. Because of the prismless design, this cavity was scaled to a higher repetition rate (191 MHz) than typical frequency comb setups based on lasers with intracavity prisms. This brought along several advantages. First, a more compact design increased the long term stability of the system relative to a lower repetition rate version (80 MHz). Furthermore, an improved f_{CE} detection setup to a DCM based delay line greatly reduced the alignment sensitivity, also contributing to better long term stability. Second, the higher repetition rate results in more power per comb line, an important factor in metrology applications where a beat signal is always observed between a single comb line and a cw laser.

We have referenced the entire frequency comb to the 1S-2S transition frequency in ultracold hydrogen by locking a comb line to a stable dye laser at 486 nm. The 486 nm dye laser is used in the 1S-2S spectroscopy and can thus be locked to the 1S-2S transition. This arrangement enables several precise frequency measurements in ultracold hydrogen. First, any 2S-nS transition can be measured relative to the well know 1S-2S transition

by using the comb to bridge the frequency gap. The experimental setup is flexible enough to perform several different measurements, requiring only that an appropriate diode laser exist at the necessary wavelength. Second, given that a stable absolute microwave reference becomes available at MIT, this system can be used to perform an absolute frequency measurement of the 1S-2S transition, currently the most accurately known optical transition frequency.

We have performed a complete characterization and analysis of the intensity-related carrier-envelope phase dynamics in octave-spanning frequency combs and our studies confirm the validity of the theoretical treatment by Haus and Ippen of soliton-like propagation in the few-cycle pulse regime. The inclusion of the self-steepening term in the expression describing the dependence of f_{CE} on intensity produces good agreement with our experimental observations. The intensity dependence of f_{CE} in OSFCs is found to be significantly simpler than in systems which employ external fiber broadening, where the effect of intensity-dependent spectral shifts of the comb spectrum was found to be of importance. Here, there is a simple linear behavior which is universal, provided that the pump power level is limited so as to prevent the appearance of pulse instabilities. The pulse energy in the octave-spanning regime is strongly clamped by the KLM action, making the intensity-related carrier-envelope frequency shift much smaller than one would expect from the behavior of the cw laser.

We have carried out a complete noise analysis of a carrier-envelope phase stabilized OSFCs. We found that including the pump power to intracavity power transfer function of the laser, that was derived from the linearized rate equations for the system, is essential to predicting the correct carrier-envelope phase noise behavior. Most importantly the finite response time of the gain introduces a phase delay that adds a phase to the closed-loop transfer function of the system. This, together with the phase delay due to the AOM, decreases the phase margin and limits the loop bandwidth to ~ 100 kHz. This limited bandwidth is insufficient to fully suppress the intensity-dependent high-frequency carrier-envelope phase noise in the system. Because these different contributions are now well

understood, the stabilization electronics can be further optimized to suppress the noise in OSFCs pumped by multi-longitudinal-mode lasers to the level of those pumped by single-longitudinal-mode lasers.

8.1 Outlook

This work reveals that there is no fundamental limit to how high a repetition rate is possible with prismless octave-spanning lasers. Therefore it is highly desirable from the point of view of metrology applications to continue to push these developments further, generating 1 GHz repetition rates and beyond.

Time domain applications were not the focus of this work, but the system developed here seems to be highly suitable for that as well. In experiments that are highly sensitive to the electric field of the pulse and not just the intensity envelope, an ultimately low residual carrier-envelope phase is desired. By enhancing our understanding of the carrier-envelope phase dynamics in octave-spanning lasers, we have now the tools necessary to design an optimum carrier-envelope phase control technique. It seems possible to completely suppress all noise sources by implementing this control via intracavity loss modulation as opposed to pump power modulation. This technique has not yet been demonstrated but our analysis shows that it would be advantageous.

From the applications point of view, the system developed here is ready to perform precision measurements in ultracold hydrogen as soon as sufficiently cold trapped hydrogen is obtained in the new cryogenic apparatus.

Bibliography

- [1] B. de Beauvoir, C. Schwob, O. Acaf, L. Jozefowski, L. Hilico, F. Nez, L. Julien, A. Clairon, and F. Biraben. Metrology of the hydrogen and deuterium atoms: Determination of the rydberg constant and lamb shifts. *European Physical Journal*, 12:61, 2000.
- [2] Kendra Margaret Denny Vant. *Spectroscopy of ultracold metastable hydrogen: in pursuit of a precision measurement*. Thesis (PhD). Massachusetts Institute of Technology, Dept. of Physics, 2005.
- [3] J. Helmcke F. Riehle H. Schnattz, B. Lipphardt and G. Zinner. First phase-coherent measurement of visible radiation. *Physical Review Lett.*, 76, 1996.
- [4] R. Holzwarth T. Udem, J. Reichert and T. W. Hänsch. Accurate measurement of large optical frequency differences with a mode-locked laser. *Optics Lett.*, 24:881–3, 1999.
- [5] R. Holzwarth T. Udem, J. Reichert and T. W. Hänsch. Absolute optical frequency measurement of the cesium d1 line with a mode-locked laser. *Physical Review Lett.*, 82:3568–71, 1999.
- [6] J. Reichert, R. Holzwarth, T. Udem, and T.W. Hänsch. Measuring the frequency of light with mode-locked lasers. *Opt. Commun.*, 172:59–68, 1999.
- [7] A. I.Ferguson J. N. eckstein and T. W. Hansch. High resolution two-photon spectroscopy with picosecond light pulses. *Physical Review Lett.*, 40:847, 1978.

- [8] M. Zimmermann C. Gohle T. Udem, R. Holzwarth and T. W. Hänsch. *Optical frequency-comb generation and high-resolution laser spectroscopy*, volume 95 of *Topics in Applied Physics*. Springer Verlag, 2004.
- [9] H. A. Haus. Theory of mode locking with a slow saturable absorber. *IEEE Journ. of Quantum Electron.*, QE 11:736–46, 1975.
- [10] H. A. Haus. Theory of mode locking with a fast saturable absorber. *Journ. of Appl. Phys.*, 64:3049–58, 1975.
- [11] D. E. Spence, P. N. Kean, and W. Sibbett. 60-fs pulse generation from a self-mode-locked ti:sapphire laser. *Opt. Lett.*, 16:42–4, 1991.
- [12] U. Keller, G. W. 'tHooft, W. H. Knox, and J. E. Cunningham. Femtosecond pulses from a continuously self-starting passively mode-locked ti:sapphire laser. *Optics Lett.*, 16:1022–1024, 1991.
- [13] F. Salin, J. Squier, and M. Piché. Modelocking of ti:sapphire lasers and self-focusing: a gaussian approximation. *Optics Lett.*, 16:1674–1676, 1991.
- [14] E. P. Ippen, H. A. Haus, and L. Y. Liu. Additive pulse modelocking. *J. Opt. Soc. Am. B*, 6:1736–1745, 1989.
- [15] J. Goodberlet, J. Jacobson, J. G. Fujimoto, P. A. Schulz, and T. Y. Fan. Self-starting additive pulse modelocked diode-pumped nd:yag laser. *Optics Letters*, 15:504–506, 1990.
- [16] K. J. Blow and D. Wood. Modelocked lasers with nonlinear external cavities. *J. Opt. Soc. Am B*, 5:629–632, 1988.
- [17] F. X. Kaertner. *Ultrafast Optics course, class notes*.
- [18] Anthony E. Siegman. *Lasers*. University Science Books.

- [19] Evgeni Sorokin. *Solid-state materials for few-cycle pulse generation and amplification*, volume 95 of *Topics in Applied Physics*. Springer Verlag, 2004.
- [20] J.K. Ranka, R.S. Windeler, and A.J. Stentz. Visible continuum generation in air-silica microstructure optical fibers with anomalous dispersion at 800 nm. *Opt. Lett.*, 25:25–7, 2000.
- [21] Ye J. Cundiff S. T. Fortier, T. M. and R. S. Windeler. Nonlinear phase noise generated in air-silica microstructure fiber and its effect on carrier-envelope phase. *Opt. Lett.*, 27:445, 2002.
- [22] Jones D. J. Ye J. Cundiff S. T. Fortier, T. M. and R. S. Windeler. Long-term carrier-envelope phase coherence. *Opt. Lett.*, 27:1436.
- [23] J. K. Ranka A. Stentz R. S. Windeler J. L. Hall D. J. Jones, S. A. Diddams and S.T. Cundiff. Carrier-envelope phase control of femtosecond modelocked lasers and direct optical frequency synthesis. *Science*, 288:635–639, 2000.
- [24] T. W. Hänsch J. C. R. Holzwarth, T. Udem, W. J. Wadsworth Knight, and P. S. J. Russell. Optical frequency synthesizer for precision spectroscopy. *Physical Review Lett.*, 85:2264, 2000.
- [25] A. Poppe, R. Holzwarth, A. Apolonski, G. Tempea, Ch. Spielmann, T.W. Hänsch, and F. Krausz. Few-cycle optical waveform synthesis. *Applied Physics B Lasers and Optics*, 72(3):373–376, 2001.
- [26] J. Ye, L. S. Ma, and J. L. Hall. Molecular iodine clock. *Phys. Rev. Lett.*, 87:270801, 2001.
- [27] S. A. Diddams, Th. Udem, J. C. Bergquist, E. A. Curtis, R. E. Drullinger, L. Hollberg, W. M. Itano, W. D. Lee, C. W. Oates, C. W. Vogel, and D. J. Wineland. An optical clock based on a single trapped hg-199(+) ion. *Science*, 293:825, 2001.

- [28] R. Ell, U. Morgner, F. X. Kärtner, J. G. Fujimoto, E. P. Ippen, V. Scheuer, G. Angelow, and T. Tschudi. Generation of 5 fs pulses and octave-spanning spectra directly from a ti:sapphire laser. *Opt. Lett.*, 26:373–375, 2001.
- [29] L. Matos, D. Kleppner, O. Kuzucu, T. R. Schibli, J. Kim, E. P. Ippen, and F. X. Kärtner. Direct frequency comb generation from an octave-spanning, prism-less ti:sapphire laser. *Opt. Lett.*, 28:2198, 2004.
- [30] T. M. Fortier, D. J. Jones, and S. T. Cundiff. Phase stabilization of an octave-spanning ti:sapphire laser. *Opt. Lett.*, 28:2198, 2003.
- [31] T. M. Ramond, S. A. Diddams, L. Hollberg, and A. Bartels. Phase-coherent link from optical to microwave frequencies by means of the broadband continuum from a 1-ghz ti:sapphire femtosecond oscillator. *Opt. Lett.*, 27:1842–1844, 2002.
- [32] T. M. Fortier, A. Bartels, and S. A. Diddams. A high repetition rate octave-spanning ti:sapphire laser for optical frequency measurements and comparisons. *LEOS IEEE Summer Topicals*, San Diego, July 2005.
- [33] O. D. Mücke, T. Tritschler, M. Wegener, U. Morgner, and F. X. Kärtner. Determining the carrier-envelope offset frequency of 5-fs pulses using extreme nonlinear optics in zno. *Opt. Lett.*, 27:2127–2129, 2002.
- [34] T. Tritschler, K. D. Hof, M.W. Klein, and M. Wegener. Variation of the carrier-envelope phase of few-cycle laser pulses owing to the gouy phase: a solid-state-based measurement. *Opt. Lett.*, 30:753, 2005.
- [35] T. Fuji, J. Rauschenberger, A. Apolonski, V. S. Yakovlev, G. Tempea, T. Udem, C. Gohle, T.W. Hänsch, W. Lehnert, M. Scherer, and F. Krausz. Monolithic carrier-envelope phase-stabilization scheme. *Opt. Lett.*, 30:332, 2005.

- [36] T. R. Schibli, K. Minoshima, F.-L. Hong, H. Inaba, A. Onae, H. Matsumoto, I. Hartl, and M. E. Fermann. Frequency metrology with a turnkey all-fiber system. *Opt. Lett.*, 29:2467, 2004.
- [37] B. R. Washburn, S. A. Diddams, N. R. Newbury, J. W. Nicholson, M. F. Yan, and C. G. Jørgensen. Phase-locked, erbium-fiber-laser-based frequency comb in the near infrared. *Opt. Lett.*, 29:250, 2004.
- [38] P. Kubina, P. Adel, F. Adler, G. Grosche, T.W. Hänsch, R. Holzwarth, A. Leitenstorfer, B. Lipphardt, and H. Schnatz. Long term comparison of two fiber based frequency comb systems. *Opt. Express*, 13:904, 2005.
- [39] Hermann A. Haus. A theory of forced mode locking. *IEEE Journal of Quantum Electronics*, 11:323–330, 1975.
- [40] H. A. Haus. Mode-locking of lasers. *IEEE J. Sel. Top. Quantum Electron*, 6:1173–1185, 2000.
- [41] P. G. Drazin and R. S. Johnson. *Solitons: an introduction*. Cambridge University Press, New York, 1990.
- [42] O. E. Martinez, R. L. Fork, and J. P. Gordon. Theory of passively modelocked lasers including self-phase modulation and group-velocity dispersion. *Optics Lett.*, 9:156–158, 1984.
- [43] F. X. Kärtner, U. Morgner, T.Schibli, R. Ell, J. G. Fujimoto, E. P. Ippen, and H.A. Haus. *Few-cycle pulse generation directly from the laser*. Topics in Applied Physics. Springer Verlag, 2004.
- [44] Ch. Spielmann, P. F. Curley, T. Brabec, and F. Krausz. Ultrabroadband femtosecond lasers. *IEEE Journal of Quantum Electronics*, 30(4):1100 – 1114, 1994.
- [45] K. Tamura, E. P. Ippen, H. A. Haus, and L. E. Nelson. 77-fs pulse generation from a stretched-pulse modelocked all-fiber ring laser. *Optics Letters*, 18:1080–1082, 1993.

- [46] Y. Chen, F. X. Kärtner, U. Morgner, S. H. Cho, H. A. Haus, J. G. Fujimoto, and E. P. Ippen. Dispersion managed mode-locking. *J. of the Optical Society of America B*, 16:1999, 1999.
- [47] U. Morgner, F. X. Kärtner, S. H. Cho, H. A. Haus, J. G. Fujimoto, E. P. Ippen, V. Scheuer, G. Angelow, and T. Tschudi. Sub-two cycle pulses from a kerr-lens modelocked ti:sapphire laser. *Optics Letters*, 24:411 – 413, 1999.
- [48] F. X. Kärtner, N. Matuschek, T. Schibli, U. Keller, H. A. Haus, C. Heine, R. Morf, V. Scheuer, M. Tilsch, and T. Tschudi. Design and fabrication of double-chirped mirrors. *Optics Lett.*, 22(13):831–833, 1997.
- [49] N. Matuschek, F. X. Kärtner, and U. Keller. Theory of double-chirped mirrors. *IEEE J. of Sel. Topics in Quantum Electronics*, 4(2):197, 1998.
- [50] T. R. Schibli, O. Kuzucu, J.-W. Kim, E. P. Ippen, J. G. Fujimoto, F. X. Kaertner, V. Scheuer, and G. Angelow. Toward single-cycle laser systems. *IEEE J. of Selected Topics in Quantum Electronics*, 9(4):990–1001, 2003.
- [51] M. Tilsch, V. Scheuer, J. Staub, and T. Tschudi. Direct optical monitoring instrument with a double detection system for the control of multilayer systems from the visible to the near infrared. *SPIE Conf Proc.*, 2253:414–22, 1994.
- [52] V. Scheuer, M. Tilsch, and T. Tschudi. Reduction of absorption losses in ion beam sputter deposition of optical coatings for the visible and near infrared. *SPIE Conf Proc.*, 2253:445–54, 1994.
- [53] Onur Kuzucu. *High repetition rate Ti:Sapphire modelocked laser*. Thesis (S.M.). Massachusetts Institute of Technology, Dept. of Electrical Engineering and Computer Science, 2003.
- [54] L. Matos, O. Kuzucu, T. R. Schibli, J. G. Fujimoto, E. P. Ippen, and F. X. Kaertner. Direct frequency comb generation from an octave spanning prismless ti:sapphire

- laser. In *Conference on Lasers and Electro-Optics (CLEO)*, page CThPDB11, Baltimore, 2003.
- [55] O. D. Muecke, Ell R., A. Winter, Kim J., J. R. Birge, L. Matos, and F. X. Kaertner. Self-referenced 200 mhz octave-spanning ti:sapphire laser with 50 attosecond carrier-envelope phase jitter. *Optics Express*, 13(13):5163–5169, 2005.
- [56] C. L. Phillips. *Feedback control systems*. Prentice Hall, 3rd edition, Englewood Cliffs, NJ, 1996.
- [57] L. Xu, C. Spielmann, A. Poppe, T. Brabec, F. Krausz, and T.W. Hänsch. Route to phase control of ultrashort light pulses. *Opt. Lett.*, 21:2008–10, 1996.
- [58] S. T. Cundiff, J. Ye, and J. L. Hall. Optical frequency synthesis based on mode-locked lasers. *Rev. Sci. Instrum.*, 72:3749–3771, 2001.
- [59] Tara M. Fortier, David J. Jones, Jun Ye, Steven T. Cundiff, and Robert S. Windeler. Long-term carrier-envelope phase coherence. *Opt. Lett.*, 27:1436, 2002.
- [60] C. L. Cesar, D. G. Fried, T. C. Killian, A. D. Polcyn, J. C. Sandberg, I. A. Yu, T. J. Greytak, D. Kleppner, and J. M. Doyle. Two-photon spectroscopy of trapped atomic hydrogen. *Phys. Rev. Lett.*, 77:255, 1996.
- [61] Erich P. Ippen. *6.634 Nonlinear Optics class notes*. MIT, Spring Term 2003.
- [62] L. Matos, O. D. Mücke, J. Chen, and F. X. Kärtner. Carrier-envelope phase dynamics and noise analysis in octave-spanning ti:sapphire lasers. *submitted to Optics Express*, 2005.
- [63] Adela Marian Steven T. Cundiff Kevin W. Holman, R. Jason Jones and Jun Ye. Detailed studies and control of intensity-related dynamics of femtosecond frequency combs from mode-locked ti:sapphire lasers. *IEEE J. of selected topics in Quantum Electron.*, 9(4):1018–1024, 2003.

- [64] H. A. Haus and E. P. Ippen. Group velocity of solitons. *Opt. Lett.*, 26(21):1654, 2001.
- [65] G. P. Agrawal. *Nonlinear Fiber Optics*. Academic Press, 3rd edition, San Diego, 2001.
- [66] Y. Lai H. A. Haus. Quantum theory of soliton squeezing: a linearized approach. *J. Opt. Soc. Am. B*, 7:386–392, 1990.
- [67] S. Witte, R. T. Zinkstok, W. Hogervorst, and K. S. E. Eikema. Control and precise measurement of carrier-envelope phase dynamics. *Appl. Phys. B*, 78:5–12, 2004.
- [68] F. M. Gardner. *Phaselock Techniques*. John Wiley, 3rd edition, Hoboken, NJ, 2005.
- [69] F. X. Kärtner, L. R. Brovelli, D. Kopf, M. Kamp, I. Calasso, and U. Keller. Control of solid state laser dynamics by semiconductor devices. *Optical Engineering*, 34:2024–2036, 1995.
- [70] F. X. Kärtner, I. D. Jung, and U. Keller. Soliton mode-locking with saturable absorbers. *IEEE J. Sel. Top. Quantum Electron*, 2:540–556, 1996.
- [71] M. Niering, R. Holzwarth, J. Reichert, P. Pokasov, Th. Udem, M. Weitz, T. W. Hänsch, P. Lemonde, G. Santarelli, M. Abgrall, P. Laurent, C. Salomon, and A. Clairon. Measurement of the hydrogen 1s- 2s transition frequency by phase coherent comparison with a microwave cesium fountain clock. *Phys. Rev. Lett.*, 84:5496, 2000.
- [72] Claudio Lenz Cesar. *Two-photon spectroscopy of trapped atomic hydrogen*. Thesis (PhD). Massachusetts Institute of Technology, Dept. of Physics, 1996.
- [73] T. Udem, S. A. Diddams, K. R. Vogel, C. W. Oates, E. A. Curtis, W. D. Lee, W. M. Itano, R. E. Drullinger, J. C. Bergquist, and L. Hollberg. Absolute frequency measurement of the hg+ and ca optical clock transitions with a femtosecond laser. *Physical Review Lett.*, 84(22):4996–99, 2001.

- [74] J. Stenger, C. Tamm, N. Haverkamp, S. Weyers, and H. R. Telle. Absolute frequency measurement of the 435.5-nm yb-171(+)-clock transition with a kerr-lens mode-locked femtosecond laser. *Opt. Lett.*, 26:1589, 2001.